Laser-induced Crystallization of Barium Strontium Titanate Thin Films for Microwave Device Applications

A thesis submitted in partial fulfillment of the requirements for the award of the degree of

DOCTOR OF PHILOSOPHY

in PHYSICS

by

J PUNDAREEKAM GOUD

(**Reg. No: 13PHPH07**)



School of Physics University of Hyderabad Hyderabad – 500046, Telangana, India

December 2020

DECLARATION

I, J PUNDAREEKAM GOUD, hereby declare that the matter embodied in this thesis

entitled "Laser-induced Crystallization of Barium Strontium Titanate Thin Films for

Microwave Device Applications" is submitted to the University of Hyderabad in partial

fulfillment for the award of Doctor of Philosophy in Physics is an original research work

carried out by me under the supervision of Prof. K. C James Raju, in School of Physics,

University of Hyderabad, Telangana, India. I also declare that this work has not been submitted

previously in part or in full to this University or any other university or institution for the award

of any degree or diploma.

A report on plagiarism statistics from university of Hyderabad library is also

enclosed.

J. Phindercelosing Gard

J Pundareekam Goud

Reg. No: 13PHPH07

Place: Hyderabad

Date: 22-12-2020



CERTIFICATE

This is to certify that the research work presented in the thesis entitled "Laser-induced Crystallization of Barium Strontium Titanate Thin Films for Microwave Device Applications" submitted by J PUNDAREEKAM GOUD bearing the registration number 13PHPH07. In the partial fulfillment of the requirements for the award of DOCTOR OF PHILOSOPHY (Ph. D) in Physics at School of Physics is a bonafide work carried out by him under my supervision and guidance.

This thesis is free from plagiarism and has not been submitted previously in part or in full to this University or any other University or institution for the award of any degree or diploma. Further, the student has the following publications before submission of the thesis for adjudication.

- 1. J. Pundareekam Goud, S Ramakanth, Andrews Joseph, Kongbrailatpam Sandeep, G L N Rao, and K C James Raju, "Effect of crystallinity on microwave tunability of Pulsed laser deposited Ba_{0.5}Sr_{0.5}TiO₃ Thin Films" Thin Solid Films 626 126–130 (2017).
- 2. **J. Pundareekam Goud**, Kongbrailatpam Sandeep, Sivanagi Reddy Emani, Mahmoud. S. Alkathy, Kuna Lakshun Naidu¹ and K C James Raju "Zr-substituted Ba_{0.6}Sr_{0.4}TiO₃ ferroelectric thin films grown by pulsed laser deposition (PLD) at different laser fluence". **Ferroelectrics**, **VOL. 516**, **28–35** (2017).
- 3. J. Pundareekam Goud, Mahamoud S. Alkathy, K.C. James Raju, "Structural, dielectric and impedance study of Bi and Li co-substituted Ba_{0.5}Sr_{0.5}TiO₃ ceramics for tunable microwave devices applications", Journal of Materials Science: Materials in Electronics, 29, 3611–3620 (2018).
- 4. **J. Pundareekam Goud**, Mahmoud S. Alkathy, Kongbrailatpam Sandeep, S Ramakanth and K. C. James Raju "Influence of laser fluence on structural, optical and microwave dielectric properties of pulsed laser deposited Ba_{0.6}Sr_{0.4}TiO₃ thin films". **Journal of Materials Science: Materials in Electronics**, 29, 15973–15982 (2018).

- 5. **J. Pundareekam Goud**, Ajeet Kumar, S Ramakanth, Kongbrailatpam Sandeep, and K.C. James Raju, "Tunable microwave device fabrication on low-temperature crystallized **Ba_{0.5}Sr_{0.5}TiO₃** thin films by an alternating deposition and laser annealing process", **Manuscript being reviewed and revised**.
- 6. **J. Pundareekam Goud**, Ajeet Kumar, Kongbrailatpam Sandeep, Deepak kumar, S. Ramakanth, K. C. James Raju, A.R. James, Partha Ghoshal "Reducing the leakage current in BST by a low temperature crystallization process", **Manuscript unde preparation**.

Presentations in the following conferences:

- 1. **J. Pundareekam Goud,** Andrews Joseph, S. Ramakanth, Kuna Lakshun Naidu, and K. C. James Raju "Microwave dielectric and optical properties of amorphous and crystalline Ba_{0.5}Sr_{0.5}TiO₃ thin films" ICC-2015, POSTER presentation.
- 2. **J. Pundareekam Goud**, S Ramakanth, Ajeet kumar, and K C James Raju, Laser induced crystallization of tunable BST thin films suitable for RF and high frequency devices, ISIF-2017, ORAL presentations.

Further, the student has passed the following course towards the fulfillment of course work required for Ph.D.

S. No.	Course code	Name	Credits	Pass/Fail
1	PY801	Advanced quantum mechanics	4	Pass
2	PY803	Advanced Statistical mechanics	4	Pass
3	PY804	Advanced electromagnetic theory	4	Pass
4	PY821	Research Methodology	4	Pass

DEAN
School of Physics
University of Hyderabad
Hyderabad-500 046, INDIA

Dean, School of Physics, University of Hyderabad.

Place: Hyderabad
Date: 22 - 12 - 2020

Supervisor

Prof. K. C James Raju School of Physics, University of Hyderabad.

Dr. K.C. James Raju
Professor
School of Physics
University of Hyderabad
Hyderabad-500 046. INDIA

Dedicated

to

Parents, Teachers and Friends

Acknowledgements

It gives me an immense pleasure to express my gratitude to one and all for helping me in a long run. It's time to bring them to stage since, most of them were behind the screens. On this note, I thank all of them who involved directly or indirectly for a successful completion of my doctoral thesis.

Firstly, I am greatly honoured to express my deepest gratitude to my supervisor, Prof. K.C James Raju for giving me the opportunity to join his research group. I would like to specially thank him for his guidance, valuable scientific discussions, inspiring attitude and support throughout the research work. His constant encouragement, freedom to work with anything and at any time made my life much easier and it helped me a lot.

Besides my supervisors, I would like to thank my doctoral committee members: Prof. S.V.S Nageshwar Rao and Dr. Venkataiah Gorige for their valuable discussions, insightful comments and encouragement. I am heartily thankful to the present Dean Prof. Ashok Chatarji and former Deans, Prof. Seshu Bai, Prof. Bindu A Bamba, Prof. Rajender Singh, Prof. S. Chaturvedi and Prof. S. P. Tiwari for providing me with the necessary facilities in School of Physics.

I would like to thank to present and former Vice Chancellers of University of Hyderabad Prof. Apparao Podile and Prof. Ramakrishna Ramasamy.

I am grateful to Prof. M. Ghanashyam Krishna, Prof. Rajaram coordinators of Center for Nanotechnology (CFN), University of Hyderabad (UoH) for allowing me to access clean room facility, and Prof. Seshu Bai, coordinator of UGC-NRC for allowing me to use required characterization facilities. I would like to thank faculty members of School of Physics and SEST-UoH for offering course work, and synthesis and characterization facilities and Deportment of English for Effective Technical Communication course.

My thanks to our collaborator Dr. A.R James, Scientist-G, DMRL Hyderabad for his valuable suggestions on the work dealing with ceramic materials.

I am very grateful to my seniors and group mates, Dr. S. Ramakanth, Dr. Ajeet Kumar, Mr. K. Sandeep, Mr. Andrew Joseph, Dr. MS Alkathy, Dr. T. Anil, Dr. S. Bashaiah, Dr. S. V. N. Reddy, Akhil Raman, Sampath, Rahul, Vishnu, Srikanth, Shivikram, surjithnath, Rakesh, Sravan, Gnanashekar, Bibhudatta, Subhashree, Sravani, Shiva, Nikhil and Arun for their moral support and useful discussions during my Ph.D.

I would like to pay special thanks to Dr. Raju Botta, Dr. Ade Ramesh, Dr. B. Ravi Kumar, Dr. Sandeep Marka, M. Yadaiah, Santhanu Padhi, B. Ashok, Dr. Laxshun Naidu, Dr.P. Shivaramakrishna and Dr. Thirupathi for their moral and financial support during my Ph.D.

I would like to greatly acknowledge UoH for providing financial support under BBL scheme and DST-SERB for providing financial support under grant No. DST-SERB/ SB/S2/CMP-094/2013, Dated 20/10/2014.

My sincere thanks to the School of Physics office staff, Mr. Abraham, Mr. Sudharshan, Mrs. Deepika, Mr. Ravi Babu, Mrs. Sailaja, Mrs. Vijaya Lakshmi, Mr. Shekar, Mr. K. Srinivas, Mr. Prasad, Suresh Babu, Mukunda Reddy, Narsimha Rao, Somla, Santhosh and Krishna. I thank Ms. Sunitha (FESEM) and Mr. Naresh (GIXRD), NRC staff, Y. Jyothi and Mr. Laxminarayana for accepting to help with my experiments, CIL staff, Dr. S. Manjunath, Mr. Suresh, Mr. Pavan Kumar, Mr. Sudhakar, Mr. Rajesh, Mr. Nagaraju, and CFN staff, Mr. Pankaj, Dr. Durga Prasad, Mr. Prashanth, Mrs. Sandhya, Mrs. Grasy and Srikanth for their help and technical support.

My Thanks to University research coordinator Prof. Durga Prasad and patent cell staff and patent wire private Ltd. staff, Sruthi Kaushik, Praveen Nandan, Anjuvoda for their help in filing the patent. I am thankful to the IGML, Computer center and University finance office staff, Jaffer, Sriramulu, David Raju, Parameshwar, Raghunathan, Rani, Sravan, Anand.

I am thankful to my fellow research scholar's Dr. K. Ravi Babu, Dr. Binoy Krishna, Dr. Shihab, Arun Nimmala, B. Prakash, Joshi Joseph, Dr. Robertson, Dr. Shivarama Krishna, Dr. Suchismitha Sahoo, Dr. Nabil, Y. Rajesh, Ch. Srinivas, K. Balaji, Atiya, Nisha Gowtham, Anupama Swain, Avisek Naresh and VenkatReddy. We have shared joy, laughter, excitement, frustration and most importantly love.

It's my pleasure to remember my Grandfathers and Grandmothers J. Yella Goud – Laxmamma, K. Gangamma, K. Pocha Goud-Balakistamma, K. Rama Goud-Kistamma for their blessings throughout my carrier.

I am greatly honored to pay my deepest gratitude to my Mother and Father J.Laxmamma-Anja Goud. I could not have come to this stage without their support. I would like to acknowledge my brothers Mr. J. Kista Goud, Banda Goud, Ashok Goud, Narasimha Goud, Mahesh Goud, Yada Goud, and sister-in-law's Mrs. J. Hamsamma, Swapna, Renuka, and my relatives J. Rama Goud, K. Narsa Goud, Chenna Goud, Ramesh Goud, Raja Goud, Manjula, Kashamma, Lalithamma, Chandrakala, Sattamma, Yashoda, Praveen, Naveen, Laxmi, Latha, shivarani, Akanksha, Krishna for supporting me spiritually throughout my career. I thank my nieces and nephews for their best wishes and prayers. Above all it is the endless sacrifice, support and motivation from my family and friends which has brought me to the position where I am.

My apologies to the people who are not covered on this note but helped throughout my carrier.

(J Pundareekam Goud)

List of contents

Tit	le		Page No.	
	nowledgements		ii	
	le of contents		iv	
	of figures of tables		viii xiv	
	onyms		xvi	
Abs	tract		xix	
Cha	pter 1: Introducti	on		
1.1	Introduction			3
1.2	Choice of Material			4
	1.2.1 Ferroelectric	Materials		4
	1.2.2 Barium Stron	ntium Titanate (BST)		6
	1.2.3 Tunable Mat	terial		7
	1.2.4 BST Varacto	ors		8
1.3	Challenges Posed by	y High Crystallization Temperature	of BST Thin Films	11
1.4	Laser Annealing and	d Its Importance in Low Temperatur	e Crystallization	11
	1.4.1 Literature Su	ırvey		14
	1.4.2 Mechanism	of Laser Annealing: Lattice Mending	g Theory	19
1.5	Motivation of the Tl	hesis		22
1.6	Objectives of the Th	nesis		23
1.7	Organization of the	Thesis		24
Refe	ences			27
Cha	pter 2: Experimer	ntal Procedures		
2.1	BST ceramic target	preparation		33
2.2	Pulsed Laser Depos	tion (PLD)		36
2.3	Deposition of BST t	thin films by PLD		39
2.4	Laser Annealing set	up		40
2.5	Characterization tec	chniques		42
	2.5.1 X-ray Diffra	ection		43
	2.5.2 Field Emissi	ion Scanning Electron Microscopy (I	FESEM)	46

	2.5.3	Transmission Electron Microscopy (TEM)	47
	2.5.4	Thin film thickness measurement	49
	2.5.5	Band gap measurement from UV-Visible spectroscopy	50
	2.5.6	Raman spectroscopy	51
2.6	Electric	cal Measurement	52
	2.6.1	Leakage current measurement	52
2.7	Device	fabrication	54
	2.7.1	Test structure fabrication	54
	2.7.2	Circular Patch Capacitor (CPC) fabrication	55
	2.7.3	Interdigitated capacitor (IDC) fabrication	57
2.8	Microw	vave Dielectric properties for BST thin films	58
	2.8.1	SOLT Calibration	59
	2.8.2	TRL Calibration	60
Refer	rences		62
Cha	pter 3: 1	In-situ crystallization of Ba _{0.5} Sr _{0.5} TiO ₃ thin films	
3.1	Introduc	ction	67
3.2	Deposit	tions Conditions	68
3.3	properti	rement of structural, microstructural and microwave dielectric ies X-ray diffraction (XRD) Studies	69 69
		Calculation of Orientation Factor (OF)	71
		Microstructural studies by FESEM	71
3.4		ric studies at Microwave frequencies	72
3.5	Conclus	•	74 76
	rences		70 77
		In-situ crystallization of Ba _{0.6} Sr _{0.4} TiO ₃ thin films	, ,
Ulla	-	•	81
4 1	Introdu	ction	A I
4.1 4.2	Introduc Experin		
4.2	Experin	mental detailes	82
	Experin Results		

	4.3.3	Stru	ectural studies by Transmission Electron Microscopy (TEM)	87
4.4	Optica	al pro	perties	89
	4.4.1	UV-	-Visible Spectroscopy - Bandgap studies	89
	4.4.2	Ran	nan spectroscopy	91
4.5	Micro	wave	dielectric properties	92
4.6	Concl	usion	s	94
Refer	ences			95
Chaj	pter 5:	Cry	stallization of BST thin films using laser irradiation	Į.
		at 3	300°C	
5.1	Introd	uctio	n	101
5.2	Exper	iment	tal	102
	5.2.1	Dep	osition of Ba _{0.5} Sr _{0.5} TiO ₃ thin films	102
	5.2.2	Lase	er annealing of Ba _{0.5} Sr _{0.5} TiO ₃ thin films	103
5.3	Resul	ts and	discussions	104
	5.3.1	Effe	ect of pulse count	104
		I	Phase and stuctural analysis	104
		II	TEM Analysis	106
		III	Microstructure properties	109
		IV	Optical properties	112
			a Raman analysis	112
			b Bandgap studies	113
	5.3.2	Effe	ect of repetition rate	116
	5.3.3	Effe	ect of Laser Energy Density	118
5.4	Micro	wave	characterization	120
5.5	Cross	-secti	onal TEM studies	123
5.6	Concl	usion	S	125
Refer	ences			126

Cnaj	pter 6:	Full depth crystallization of BS1 with laser annealing	OI
		layers at 300°C	
6.1	Introd	uction	131
	6.1.1	Laser annealing: Full vertical crystallization	132
6.2	Exper	imental	133
	6.2.1	Deposition of and Laser annealing Ba _{0.5} Sr _{0.5} TiO ₃ thin films	133
6.3	Phase	and stuctural analysis	135
6.4	TEM	analysis	136
6.5	Micro	structure properties	139
6.6	Optica	al properties	140
	6.6.1	Raman analysis	140
	6.6.2	Bandgap studies	141
6.7	Micro	wave dielectric properties	143
6.8	Electr	ical Properties	148
	6.8.1	Leakage current studies for BST thin films deposited at high temperature	148
	6.8.2	Leakage current studies for laser annealed BST thin films	150
6.9	High	overtone bulk acoustic resonator (HBAR) response	153
6.10	Concl	usions	155
Refer	ences		157
Chaj	pter 7:	Conclusions and scope of future work	
7.1	Concl	usions	161

165

166

Scope of future work

List of Publications

7.2

List of figures

Chapter-1

Figure No	Description	Page No.
1.1	(a) The variation of dielectric constant in the vicinity of Curie	5
	point. P-E graph of material in (b) ferroelectric (hysteresis loop)	
	phase (c) paraelectric phase.	
1.2	Structure of Barium Strontium Titanite (BST)	7

Chapter-2

Figure No	Description	Page No.
2.1	Schematic diagram of steps in solid state reaction method	33
2.2	(a) Uniaxial Pressing (b) Green Pellets (c) High Temperature furnace, (d) Sintered Target	34
2.3	X-ray diffraction pattern of Ba _{0.5} Sr _{0.5} TiO ₃ target	35
2.4	(a) FESEM image and (b) EDAX of Ba _{0.5} Sr _{0.5} TiO ₃ sintered target	36
2.5	Schematic diagram of Pulsed Laser Deposition (PLD) system	38
2.6	Pulsed laser deposition (PLD) set up with high vacuum (HV) chamber	38
2.7	Schematic diagram of the laser annealing setup	40
2.8	Set-up for the laser annealing of thin films with the chamber and KrF- Excimer laser	42
2.9	(a) Bruker D8 advanced diffractometer for bulk (b) Bruker D8 discover for thin films (GIXRD)	45
2.10	(a) Field emission scanning electron microscope (model: Carl ZEISS, Ultra55, Germany) (b) Gold coating sputtering unit for non-conducting samples	47
2.11	TEM system used for the work (FEI Tecnai G2-STWIN TEM)	48
2.12	Stylus Profilometer (XP-200, Ambios Technology, USA)	49
2.13	Illustration of stylus profilometer based measurement of film thickness (b)Thickness measurement result for BST thin films	50

2.14	(a) UV-VIS-NIR spectrophotometer (JASCO V-570). (b) Shows	51
	the transmission spectra of BST thin film	
2.15	Photograph of the Raman spectrophotometer (Witec Alpha 300)	52
2.16	TF 1000 Analyzer of aixACCT GMBH, Germany for leakage	53
	current measurement.	
2.17	Wave form for leakage current measurements [Hysteresis	54
	software version 2.4.0.0 user manual, aixACCT GMBH,	
	Germany]	
2.18	Schematic of the device fabrication process used to fabricate test	55
	structures with ferroelectric thin films	
2.19	Schematic of the cross section of a Circular Patch Capacitor	56
	(CPC) test structure for microwave measurement of BST thin film	
	on Pt/Si, top electrode: Cr-Au; (b) Top view of the CPC test	
	structure: Centre (80μm) and outer circle (300μm)	
2.20	(a) Schematic of IDC structure (b) FESEM image of fabricated	58
	IDC	
2.21	On wafer probing measurement setup with probe station, VNA	59
	and DC voltage source	
2.22	(a) One port vector calibration for port-1 and port-2 (b) Microstrip	60
	SOLT standards. Dotted line denotes the reference plane	
2.23	Microstrip TRL standards. The electrical reference plane is at the	61
	center of theThru	

Figure	Description	Page No.
No		
3.1	(i) XRD pattern of BST5 films on MgO substrates. (ii) depicts	71
	the variation of lattice parameter and unit cell volume with	
	oxygen working pressure	
3.2	The FESEM images of BST5 films grown on MgO substrates	73
	(a) MBST5-001 (b) 002, (c) 003, (d) 004 and (e) 005.	
3.3	Variation of capacitance with frequency for MBST5-003, 004	74
	and 005 films for IDC structures derived from data measured by	
	VNA (vector network analyzer) at two different voltages namely	
	0 V and 75 V.	

Description	Page No.
(a) XRD patterns and (b) lattice parameter and unit cell volume	84
of the BST6 films deposited at various laser fluences	
W-H plots of BST6 films grown at different laser fluence	85
Crystallite size and (b) Strain of BST6 films deposited at different laser fluence	86
Microstructure of different BST6 films grown at different laser fluence	87
TEM images of BST6 films grown at different laser fluence(a) Bright field images (b) HRTEM and (c) Selected area diffraction (SAED) patterns.	88
(a) Optical transmission and (b) $(\alpha h v)^2$ vs $h v$ plots of BST6 films	89
Optical band gap values of BST6 films deposited at different laser fluence	91
Raman spectrum of BST6 films showing improving crystallinity with increase in laser fluence during deposition.	91
Microwave Dielectric properties of 2 J/cm ² laser fluence grown BST6 thin films. (a) Schematic top and cross-sectional view of CPC test structure made on BST6 films. (b and c) Capacitance and dielectric loss (tanδ) variation with frequency.	93
	 (a) XRD patterns and (b) lattice parameter and unit cell volume of the BST6 films deposited at various laser fluences W-H plots of BST6 films grown at different laser fluence Crystallite size and (b) Strain of BST6 films deposited at different laser fluence Microstructure of different BST6 films grown at different laser fluence TEM images of BST6 films grown at different laser fluence(a) Bright field images (b) HRTEM and (c) Selected area diffraction (SAED) patterns. (a) Optical transmission and (b) (αhv)² vs hv plots of BST6 films Optical band gap values of BST6 films deposited at different laser fluence Raman spectrum of BST6 films showing improving crystallinity with increase in laser fluence during deposition. Microwave Dielectric properties of 2 J/cm² laser fluence grown BST6 thin films. (a) Schematic top and cross-sectional view of

Figure	Description	Page No.
No		
5.1	X-ray diffraction pattern of BST5 thin films (a) Deposited at	105
	700°C and 300°C (a) Films on FS substrates deposited and laser	
	annealed at 300°C with 50, 250, (b) 500, 1000, 2000 and 3000	
	number of annealing pulses	
5.2	The images in columns (a) (b) and (c) shows the TEM Bright	107
	field, selected area diffraction (SAED) and HRTEM patterns of	
	BST5 thin films respectively (i)ADF 300 FS (ii) ADF 700 FS	
5.3	(i)-(vi) TEM images of BST5 films laser annealed with different	108
	laser pulses (a) Bright field images (b) Selected area diffraction	
	(SAED) patterns and (c) HRTEM	
5.4	FESEM images (a, c) and Cross-sectional SEM (b, d) of ADF	110
	300 FS and ADF 700 FS	
5.5	The FESEM images of LA 300FS -50 to LA 300FS- 3000:	111
	BST5 films laser annealed with different number of laser	
	pulses. At different magnifications and the histogram of grain	
	sizes observed	
5.6	Raman spectra of BST5 thin films annealed with	113
	different no. of laser pulses in comparison with in-situ	
	crystallized films and as deposited films	
5.7	(a) Transmission spectra (b) Plots of $(\alpha hv)^2$ vs. hv of BST5 films	115
	annealed with different no. of laser pulses.	
5.8	Effect of pulse repetition rate on laser annealed films (i) XRD	116
	pattern for films annealed at 5 and 10Hz. (ii) Corresponding	
	optical spectra (a) Transmission spectra (b) Plots of $(\alpha hv)^2$ vs. hv .	
5.9	Effect of Laser energy density on laser annealed films (i) The	119
	XRD pattern (ii) (a) Transmission spectra (b) Plots of $(\alpha hv)^2$ vs.	
	hv.	
5.10	Capacitance, dielectric constant & dielectric loss parameters of	121
	Ba _{0.5} Sr _{0.5} TiO ₃ (BST5) thin-films of (i) ADF 300 PS (ii) ADF 700	
	PS and (iii) LA 300 PS on platinized silicon substrates	
5.11	Cross-sectional TEM Images of BST5 thin films on fused silica	123
	substrates	

Figure No	Description	Page No.
6.1	Partial crystallization of PZT thin films (PZT 44/56 of ~600 nm,	131
	crystallized upto ~120 nm using Kr-F laser) (Lu et. al.)	
6.2	Schematic of partial crystallization of BST thin films	132
6.3	XRD patterns of BST5 thin films (i): (a) ADF 300 FS (b) ADF	135
	700 FS, (ii): (a) LLD 300 FS and (b) LLD 300 PS (iii): XRD of	
	each layer deposited on fused silica substrate.	
6.4	The images in columns (a) (b) and (c) shows the TEM Bright	137
	field, selected area diffraction (SAED) and HRTEM patterns of	
	BST5 thin films respectively (i) ADF 300 FS (ii) ADF 700 FS	
	and (iii) LLD 300 FS	
6.5	Shows cross-sectional TEM Images of BST5 thin films	138
	as deposited (ADF 700 PCS) and multilayered deposited and	
	laser annealed at 300°C (LLD 300 PCS) on platinum coated	
	silicon substrates.	
6.6	FESEM images of BST5 thin films in different magnifications	139
	(i)As deposited at 300°C (ADF 300 FS) (ii) As deposited at	
	700°C (ADF 700 FS) and (iii) Layer by layer deposited and	
6.7	annealed both at 300°C (LLD 300 FS) on fused silica	1.10
6.7	Raman spectra of the BST5 thin films of ADF 300 FS, ADF	140
	700 FS, and LLD 300 FS.	1.40
6.8	Transmission spectra and $(\alpha h v)^2$ vs. hv plots of BST5 thin films	142
6.9	of (a) ADF 300FS, (b) LLD 300 FS and (c) ADF 700 FS Schematic (cross-section and top view) of the varactor using the	1.42
0.9	BST5 film as the dielectric layer	143
6.10	Capacitance, dielectric constant & dielectric loss of	144
0.10	Ba _{0.5} Sr _{0.5} TiO ₃ (BST5) thin films of ADF 300 PS and ADF 700	144
	PS on platinized silicon substrates.	
6.11	(a-c) Capacitance, dielectric constant & dielectric loss of BST5	145
	thin films of LLD 300 PS	143
6.12	The plot of leakage current density vs. electric field for the	148
	BST5 thin film ADF 700 PS	110
6.13	The plot of log J vs. log E for the BST5 thin films ADF 700 PS	149
6.14	(i) J vs. E of ADF 300 PS and (ii) (a) J vs. E (b) log J vs. E	150
	curve for Layer-by-layer deposited and laser annealed BST5	
	thin films (LLD 300 PS).	

6.15	Log J vs. log E curve for BST5 thin films LLD 300 PS	151
6.16	(a) Measured HBAR frequency spectrum for ADF 700 PCS with and without biasing, S_{11} , (c) Calculated electric impedance in broad band range of 500 MHz $-$ 4 GHz. (b) and (d) HBAR response with and without dc bias in the 2 GHz $-$ 2.1 GHz narrow	154
6.17	band frequency range for S ₁₁ and electric impedance respectively (a), (c) Measured frequency spectrum of HBAR of LLD 300 PCS with and without dc biasing, S ₁₁ and calculated electric impedance in broad band range of 500 MHz–3 GHz respectively. Fig. (b), (d) HBAR response in S ₁₁ and electric impedance with and without dc bias in narrow frequency range of 2–2.1 GHz	155

List of Tables

Chapter-1

Table No.	Description	Page No.
1.1	Comparison of Ferroelectric varactor, semiconductor diodes and RF MEMS capacitors	10
1.2	Laser annealing done on different materials and its parameters	18

Chapter-2

Table No.	Description	Page No.
2.1	The deposition conditions for BST films	40

Chapter-3

Table No.	Description	Page No.
3.1	Nomenclature and deposition conditions of BST thin film samples deposited at constant temperature and variable pressure and laser fluence	69
3.2	The values of average crystallite size, texture ratio, orientation factor and tunability (%) for BST5 films	72

Chapter-4

Table No.	Description	Page No.		
4.1	The deposition conditions used for Ba _{0.6} Sr _{0.4} TiO ₃ thin films on a	83		
	fused silica substrate with an oxygen working pressure of 8×10 ⁻³			
	mbar. 10,000 pulses of laser shots are used with fluences as			
	given in the table.			
4.2	Crystallite size from XRD and from WH plot along with strain for	89		
	films deposited at different laser fluence			

Chapter- 5

Table No.	Description	Page No.
5.1	Deposition conditions of Ba _{0.5} Sr _{0.5} TiO ₃ films	103
5.2	Laser annealing conditions of Ba _{0.5} Sr _{0.5} TiO ₃ thin films	104
5.3	Crystallite size and Grain size values of BST5 thin films grown on FS and laser annealed at 300C with different number of laser pulses	106
5.4	Bandgap values of BST5 thin films annealed with different number of laser pulses	
5.5	Effect of pulse repetition rate during laser annealing	116
5.6	Effect of energy density of annealing laser beam	
5.7	The list of optimized parameters for laser annealing	

Chapter-6

Table No.	Description	Page No.
6.1	The conditions of films grown by layer-by-layer deposition and	134
	subsequent annealing process at the same temperature (300°C).	
6.2	Sample codes used in this chapter	134
6.3	Band gap values of layer-by-layer deposited and subsequent laser annealed BST5 thin films	143
6.4	Comparison of microwave dielectric properties of following BST 5 films: ADF 300 PS, ADF 700 PS and LLD 300 PS	146
6.5	Leakage current study for layer-by-layer laser annealed and high temperature deposited BST5 crystalline thin films.	151

Abbreviations

Abbreviation	Full form		
ADF 300	As-deposited film at 300°C		
ADF 300 FS	As deposited films at 300°C on fused silica		
ADF 700 FS	As deposited films at 700°C on fused silica		
ADF 300 PS	As-deposited film at 300°C on Platinized Silicon		
ADF 700 PS	As-deposited film at 700°C on Platinized Silicon		
ADF 300 PCS	As-deposited film at 300°C on Platinum Coated Silicon		
ADF 700 PCS	As-deposited film at 700°C on Platinum Coated Silicon		
AW	Acoustic Waves		
AC	Alternative Current		
BSE	Back Scattered Electrons		
BAW	Bulk Acoustic Wave		
BW	Band Width		
Bg	Bandgap		
BST	(Ba,Sr)TiO ₃ (Barium Strontium Titanate)		
BST5	Ba _{0.5} Sr _{0.5} TiO ₃ (Barium Strontium Titanate)		
BST6	Ba _{0.6} Sr _{0.4} TiO ₃ (Barium Strontium Titanate)		
CPC	Circular Patch Capacitor		
CMOS	Complementary Metal Oxide Semiconductor		
DC	Direct Current		
EDS	Energy Dispersive X-ray Spectroscopy		
Ed	Energy Density		
ELA	Excimer Laser Annealing		
EM	Electromagnetic		
FE	Ferroelectric		
FESEM	Field Emission Scanning Electron Microscopy		
FWHM	Full Width Half Maximum		
GHz	Giga Hertz		
GIXRD	Grazing Incidence X-ray Diffraction		

G-S-G	Ground-Signal-Ground	
HRTEM	High Resolution Transmission Electron Microscope	
HBAR	High Overtone Bulk Acoustic resonator	
Hz	Hertz	
IDC	Inter digited capacitor	
KrF	Krypton Florid	
LA	Laser Annealing	
LA 300 FS	Laser Annealing at 300°C on fused silica	
LIC	Laser Induced Crystallization	
LLD 300 PS	Layer-by-layer deposited and laser annealed film at 300°C on Platinized Silicon	
LLD 300 PCS	Layer-by-layer deposited and laser annealed film at 300°C on Platinum Coated Silicon	
LF	Laser Fluence	
MW	Micro Waves	
Nd-YAG	Neodymium-doped yttrium aluminium garnet	
OPP	Oxygen Partial Pressure	
P-E loop	Polarization-Electric field loop	
PF	Pico Farad	
PLD	Pulsed Laser Deposition	
PVD	Physical Vapour Deposition	
PZT	Pb [Zr _x Ti _{1-x}]O ₃ (0≤x≤1)Lead Zirconate Titanate	
Q factor	Quality Factor	
RF	Radio Frequency	
RTP	Rapid Thermal Annealing	
RT	Room Temperature	
SAW	Surface Acoustic Wave	
SAED	Selected Area Electron Diffraction	
SIP	System in Package	
SOC	System on Chip	
S-Parameter	Scattering Parameter	

TEM	Transmission Electron Microscope	
VNA	Vector Network Analyzer	
UP	Uniaxial Press	
XRD	X-Ray Diffraction	

Abstract

There is a technological necessity for the reduction of crystallization temperature of ferroelectric (FE) oxides to match their processing with that of the nano-electronic processing conditions. The major problem to integrate FE oxides to a conventional semiconductor processing is the higher crystallization temperature of FE oxides (> 600°C). In contrast, Si wafers with nano-scale components cannot be subjected to a temperature above 300°C. Therefore, non-thermal routes for crystallizing these films became indispensable. To obtain good quality BST films via traditional routes such as conventional furnace heating, rapid thermal processing etc. require a temperature around 700°C. Such conditions are not compatible with either polymer or silicon substrates. Hence, fabricating FE devices on these substrates are quite challenging. The only means to integrate these two technologies is by decreasing the processing temperatures of ferroelectric thin films. Understanding and finding means to lower the processing temperatures of ferroelectric thin films is a necessary task of prime importance for the realization of ferroelectrics based flexible electronics. Laser-induced crystallization (LIC), which is the primary goal of this thesis, has stood out to be one major contender for bringing down FE thin films processing temperature.

Initially Ba_{0.5}Sr_{0.5}TiO₃ (BST5) thin films are deposited at 750°C on MgO (100) substrates by pulsed laser deposition (PLD) and then it was conventionally annealed. The X-ray diffraction pattern shows that the films that are deposited at higher oxygen working pressure (1×10^{-1} mbar) are partially crystalline. The films that are deposited at lower oxygen working pressure (1×10^{-4} mbar) showed improved crystallinity. The crystallinity is further increased with a particular orientation as the laser fluence increases from 1.4 J/cm² to 2 J/cm². It is found that the maximum tunability (in IDC configuration) of 16.5% at 1GHz is obtained

for films deposited at low oxygen working pressure and high laser fluence (1×10^{-4} mbar and 2 J/cm²). These studies help us in exploring the correlation between the structural and microwave dielectric properties.

Ba_{0.6}Sr_{0.4}TiO₃ (BST6) thin films are deposited by PLD method at different laser fluences (1 J/cm² to 2 J/cm², five steps), keeping the temperature 700°C and oxygen pressure (8×10⁻³ mbar) constant. The BST6 thin films grown at 2 J/cm² shows the best microstructural and optical properties and microwave range measurements are performed on these samples by circular patch capacitor (CPC) method. The microwave tunability and dielectric constant (ε_r) of a well crystallized BST6 thin film were found to be ~56% and ~284, respectively at 1 GHz making it suitable for applications in tunable microwave devices. This investigation highlights the importance of laser fluence on determining the electrical properties (both dielectric constant value and its tunability) of the films.

The laser crystallization of amorphous BST5 thin-film is achieved after many stages of optimizations. BST5 thin films deposited using PLD at 300°C on fused silica substrates and platinized silicon are found to be amorphous. These films are later laser annealed at 300°C using a KrF excimer laser. The optimization parameters are varied to achieve LIC thin films are the number of laser pulses, the energy density, and the pulse repetition rate. X-ray diffraction method is used for the phase confirmation of the laser annealed BST thin films. The optimized laser annealing parameters are 10 Hz repetition rate, 2000 pulses and laser energy density of 66 mJ/cm². The optical studies, shows a steady decrease in bandgap with increase in crystallization. Cross-sectional TEM is carried out for optimized BST5 films, and it showed that the film is crystallized only up to a thickness of 120 nm out of 600 nm.

The laser annealing in BST can be understood in terms of laser matter interaction. It is known that when nanosecond pulses of laser light is incident on the material, it generates a shockwave. The conservation relations-based shock wave velocity calculations yield low shock velocity. This slowly propagating shock waves can force atomic diffusions and pressure induced lattice mending which can be the basic mechanism in the crystallization of these films.

A novel technique is introduced to get full depth crystallization of 600 nm thick BST films using optimised condtions. This technique involves layer-by-layer (5 layers) deposition and laser annealing of BST5 thin film at 300°C using the KrF excimer laser. In this process, each layer of ~120 nm BST5 thin film is deposited and subsequently annealed at an energy density of 66 mJ/cm². The phase formation and full depth crystallization of BST5 thin films were confirmed by XRD patterns, Raman, and TEM studies. The bandgap values studied using UV-Vis-NIR spectroscopy show a systematic decrease after each laser annealing step. These layer-by-layer deposited and laser annealed BST5 thin films exhibit a 34% tunability at 1GHz (comparable to films deposited at 700°C) and with lower dielectric loss (with reference to films deposited at 700°C). The leakage current in the layer-by-layer laser annealed BST5 thin films are remarkably lower than that of high temperature deposited thin films. This is a crucial achievement because the reduction in leakage current is essential for developing commercially viable FE based tunable microwave devices, CMOS circuits and flexible electronic devices.

Chapter 1

Introduction

1.1 Introduction

The voltage tunable passive devices for application in microwave frequency range have attracted significant attention in the past two decades because of the potential it holds in the ever-expanding communication technology. The frequency agility characteristics enables reduction in the number of components required for a device operating in multiple frequency bands. Miniaturized varactors, resonators, phase-shifters, tunable filters, antennas, etc. can be fabricated with the attractive characteristics of possessing high Q (quality factor), high isolation and high speed coupled with low power consumption and low insertion loss using ferroelectric thin films and replace their bulky counterparts [1-7].

Varactors are important building blocks for RF/microwave components such tunable filters, phase shifter etc. Micromachined varactors have low loss and consume less power but has issues with stability with varying temperature. Moreover, large scale production of them in an integrated manner with other electronic circuits is difficult [3].

Since semiconductor technology provide high density device integrations, semiconductor varactor and transistors are commonly preferred in tunable microwave devices in the lower frequency bands. Currently semiconductor based tunable/switchable microwave devices are the best cost-effective fabrication technology available for commercial and defense applications. But these semiconductor-based systems fail to provide high Q factor and tuning speed in higher frequency bands and their performance degrade drastically above 10 GHz [3].

A promising technology which avoids all these drawbacks is ferroelectric thin filmbased varactors. The ferroelectric materials possess electric field dependent permittivity and this dependency is much stronger near the ferroelectric phase transition temperature. The loss of ferroelectric varactor at microwave frequencies is an order of magnitude less than that of a semiconductor varactor. Hence, a ferroelectric capacitor can in theory be used as a varactor i.e., voltage dependent capacitor, giving same functionality as RF-MEMS switch or a semiconductor PIN diode at microwave frequencies. Another major problem with RF-MEMS capacitor switches is that they being mechanical parts are sluggish and decrease the response speed. Semiconductor PIN diode become highly lossy above 10 GHz which hinder their applications in high frequency bands. Hence the alternative available through ferroelectrics are being seriously explored. This leads to considerable amount of research interest in this field [1-7].

1.2 Choice of material

1.2.1 Ferroelectric Materials

A ferroelectric material is a non-linear dielectric having spontaneous polarization whose direction can be switched by applying an external electric field [8]. These materials, exhibit a transition from a highly symmetric centrosymmetric phase to a non-centrosymmetric unit cell at the Curie temperature T_c (Fig1.1(a)). The non-centrosymmetric phase is called ferroelectric phase which have very distinct structural and physical properties which changes when the temperature is above T_c and enters paraelectric phase. Even though material in paraelectric phase does not show ferroelectric hysteresis or ferroelectricity, they maintain reasonably high permittivity near ferroelectric phase transition temperature. This ferroelectric materials in paraelectric phase have high dielectric constant and low dielectric loss which are widely explored for tunable microwave device applications. And in recent years optimizing the material parameters for industrial standard devices is under intensive investigations [4-6.9].

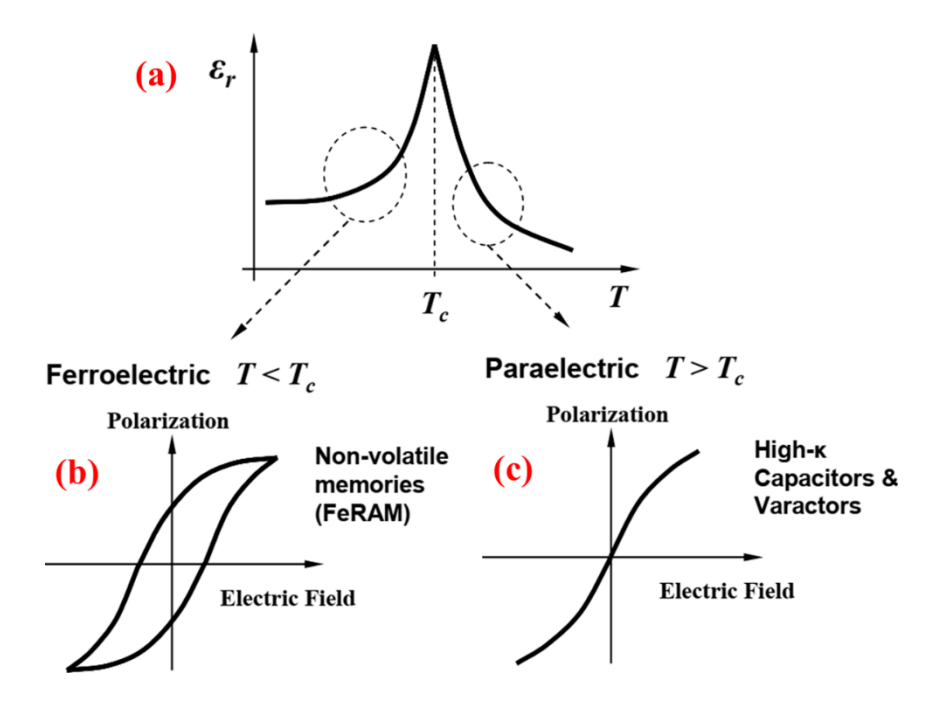


Fig 1.1.(a) The variation of dielectric constant in the vicinity of Curie point. P-E graph of material in (b) ferroelectric (hysteresis loop) phase (c) paraelectric phase [4].

Similar to ferromagnetic materials, ferroelectric materials in polar phase also have domain structure and the electric dipole moment inside domains are arranged parallel to each other. In the absence of an external electric field, all these domains are arranged randomly but in presence of on applied field the domains start to align in the direction of applied field. When the field is strong enough, all the domains are lined up along the field direction and material is said to be in the saturated state (P_{sat}). If the field is applied in the opposite direction the domains are rearranged in opposite direction. Unlike ferroelectrics in their polar phase, in paraelectric phase there is no domains and hence no hysteresis effect in polarization curve as shown in fig. 1.1(c) [4-6.9,10].

The ferroelectric materials in their paraelectric phase do not show hysteresis loop but still maintain its non-linear dielectric behavior, which leads to electric field dependent dielectric constant. In the paraelectric phase, the material is centrosymmetric and do not have domains and hysteresis loss which explain the reduced dielectric loss of paraelectric materials compared to their ferroelectric counterpart. The preferable combination of having a high non-linear dielectric response with the lack of hysteresis, and low losses make compositions exhibiting paraelectric behavior at operational temperatures quite attractive for some applications, compared to materials in their ferroelectric phase [4-6,9,10].

1.2.2 Barium Strontium Titanate

Barium Strontium Titanate $(Ba_{1-x},Sr_x)TiO_3$ $[0 \le x \le 1]$ (BST) is having ABO_3 structure in which, the A site is co-occupied by Ba and Sr atoms. In the perovskite unit cell, the Ba^{2+} and Sr^{2+} ions are occupied in the corners and oxygen anions on the face center and Ti^{4+} ions on the center of the unit cell (Fig. 1.2) [4-6]. At temperatures above the phase transition temperature (T_c) , the material is in the paraelectric (cubic) state while below T_c it exhibits ferroelectric (tetragonal) state. In paraelectric phase the lattice parameter and T_c shows strong dependency on the Ba:Sr ratio. Sr can replace Ba over the entire range of composition to form a continuous solid solution, leading to a smooth varying T_c and lattice parameter. The transition temperature of BST with Ba:Sr ratio of 50:50 $[(Ba_{0.5},Sr_{0.5})TiO_3,BST_5]$ is just below room temperature and explored widely among the various BST compositions for paraelectric varactors.

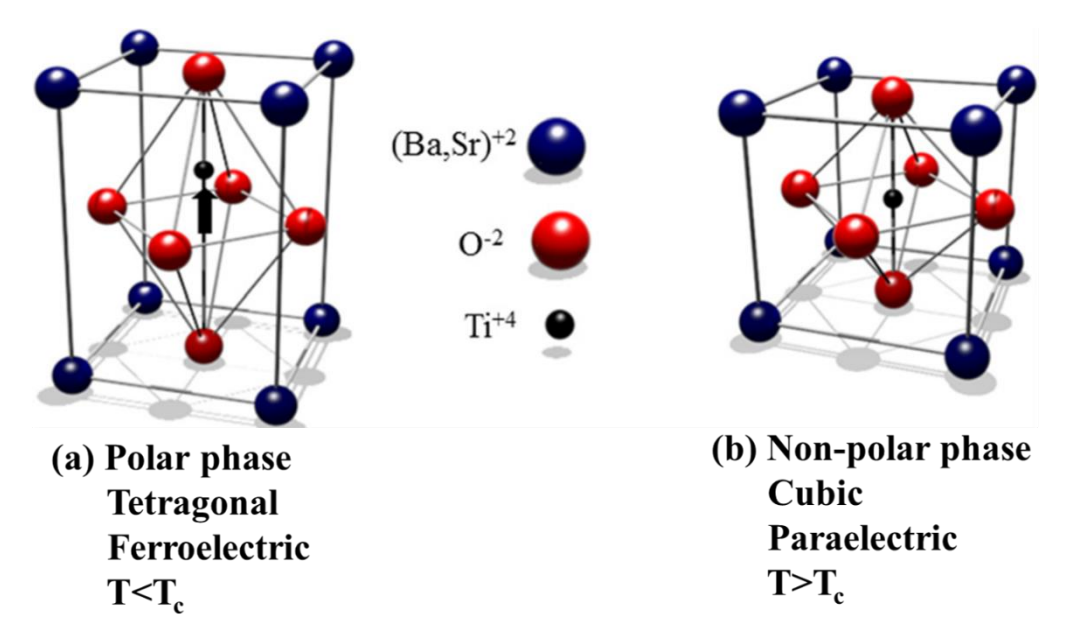


Fig.1.2. Structure of Barium Strontium Titanite (BST) [5].

1.2.3. Tunable materials

The materials having a variable dielectric constant as a function of the applied external electric field are known as tunable dielectric materials [12]. These dielectric materials find applications in various microwave devices, such as varactors, tunable oscillators, phase shifters and filters. Suitably high permittivity with low loss and reasonably high dielectric tunability are the basic factors to be considered while choosing an appropriate material for such applications. Ferroelectric materials in their paraelectric state are promising for many tunable RF and microwave applications because of their suitable dielectric constant value and tunability. With the advancement in fabrication, certain ferroelectric thin-films can be developed using monolithically compatible processes which has opened up possibility of integration of these thin films with MMIC and MIC devices [14]. The dependence of the dielectric permittivity ϵ on the applied external electric field E_0 gives the flexibility for microwave engineer to explore new tunable devices. The tunability "n" is the ratio of the permittivity of the material without an external applied electric field ϵ (0) to its permittivity under application of an electric

field $\varepsilon(E)$ as given by equation (1.1). The relative tunability n_r is defined by the relation given below (1.2) [2,5,11-13].

$$n = \frac{\varepsilon(0)}{\varepsilon(E)}$$
 1.1

$$n_r = \frac{\mathcal{E}(0) - \mathcal{E}(E)}{\mathcal{E}(0)}$$
 1.2

Numerous ferroelectric materials are being considered as suitable candidates for tunable microwave devices and SrTiO₃ and its solid solutions with BaTiO₃ and PbTiO₃ are widely explored [15]. At cryogenic temperatures, the bulk form of SrTiO₃ exhibits large tunability when applied with a large electric field [16]. Due to their high tunability and large power handling capabilities (Ba,Sr)TiO₃ thin films have been widely investigated. The fact is that thin-film processing and fabrication are compatible with the standard IC technology procedures and it is the most favorable technology for mass production [17].

BST is a high dielectric constant material which can vary its relative permittivity by applying voltage, and it shows relatively low losses at microwave frequencies [18]. The additional advantage of using BST is that it enables miniaturization of the circuit due to its high dielectric constant. Another important feature of BST is the customizable microwave dielectric properties of BST for a specific application by adjusting the ratio of strontium and barium according to the formula $Ba_xSr_{1-x}TiO_3$.

1.2.4 BST Varactors

In most of the tunable microwave devices, varactors are used as the primary tuning element [19]. Currently, microwave varactor technology is based on GaAs or silicon fabrication [20]. The varactor diode fabricated on silicon substrates could be easily integrated in the standard complementary metal-oxide-semiconductor (CMOS) integrated

circuit technology. But the downside of the semiconductor varactor diodes is their very low power handling capacity and they are also lossy at frequencies above 10 GHz [21].

Barium Strontium Titanite (BST) thin films have been investigated over the past 20 years for room temperature adjustable or reconfigurable RF and microwave components and circuits. Compared to semiconductor varactor diodes and PIN diodes MEMS varactors and varactor based on thin film BST have advantages such as high Q at higher frequency [1]. Most BST research used compositions of Ba_{0.5}Sr_{0.5}TiO₃ or Ba_{0.6}Sr_{0.4}TiO₃ because they have critical temperature (T_c) at or close to room temperature. The characterization of BST varactor reveals that they possess high Q, operate fast, miniaturized and consume low power [22-24]. Table1.1 compares the various device characteristics and performance parameter between ferroelectric varactor, semiconductor varactor diodes and RF MEMS capacitor.

Tombak et al. have reported a tunable bandpass and a lowpass filter using BST thin film [25]. Their design includes lumped inductors and BST varactor. Jayesh Nath et al. [26] reported a third-order comb-line tunable bandpass filter using BST varactors fabricated on sapphire substrates. They obtained a 16% frequency tunability from 2.44 GHz to 2.88 GHz. An impedance transformer has also been reported by Chen et al. [27]. The reported transformer could do 4:1 to 2:1 transformation in a 50 Ohm line environment. Paratek Microwave Inc has started commercializing these BST based tunable filters [28]. Even hybrid microstrip configurations (f~2 GHz) and inline waveguide resonator configurations (f~22.5 GHz) using BST thin film varactors have been reported.

Table 1.1. Comparison of Ferroelectric varactor, semiconductor diodes and RF MEMS capacitors [1].

S.No.	Device characteristics and performance parameter	Semiconductor diodes	RF MEMS capacitors	Ferroelectric varactor (parallel plate)
1	Tuning DC voltage	Low (<10 V reverse bias)	High (40–50 V bipolar)	Low (<10 V bipolar bias)
2	Capacitance tuning ratio	>3:1 in the linear range	>5:1 in the linear range	~3:1 in the linear range
3	Tuning speed	High (10 ns)	Low (~10 μs)	High (~10 ns)
4	Quality factor (Q)	~200 at 1 GHz	>500 at 1 GHz	~200 at 1 GHz (0 V)
5	Switching lifetime	High	Low	High
6	Packaging cost	Low	Very high	Low
7	Power handling	Poor (~1 W)	Good (<5 W)	Good (up to 5 W)
8	Power consumption	Low (nW-µW)	Low (nW-µW)	Low (nW-µW)
9	Breakdown voltage	Low (<25 V)	Moderate (>50 V)	Low (<25 V)
10	Linearity	Low	High	High
11	Third order intercept (IP3)	Low (~ +28 dBm)	High (~ +55 dBm)	High (~ +55 dBm)
12	Integration capability	Very good	Good	Good

1.3 Challenges Posed by High Crystallization Temperature of BST Thin Films

Conventional crystallization methods requires high temperature and it is a slow process. This high temperature crystallization process requires high thermal budget (thermal power) with long processing time. High degree of energy loss happens as all of the energy is used to raise the temperature of the substrate and the furnace. This high temperature crystallization is incompatible with thermally sensitive substrates. So, to decrease the crystallization temperature and reduce the annealing time, conventional annealing is replaced by laser annealing. The laser-based crystallization methods are considered as the most suitable and flexible method to crystallize a specific region of a device without damaging the other parts. Device quality crystallized films at lower processing temperatures is known to be achievable by the use of lasers of appropriate wavelength and pulse width in the semiconductor industry. In order to achieve crystalline ferroelectric films, it is necessary to consider the ultraviolet wavelength laser because its energy is of the order of bandgap and its non-thermal primary mode of interaction with these films.

1.4 Laser Annealing and Its Importance in Low Temperature Crystallization

Laser Induced Crystallization (LIC) or Laser annealing is referred to the phase transformation of materials from amorphous to crystalline phase at a lower temperature using a laser of high-power density and short pulse width.

The need to lower the crystallization temperature of ferroelectric (FE) materials in their thin film form is essential to meet process compatibility issues. The FE materials have multifunctionality and to make them compatible with integrated circuit processing techniques, LIC is a good solution once it is perfected. The latest technology independently incorporates semiconductor and ferroelectric based functional devices. Therefore, as the processes for both are often incompatible with temperature, the size of devices increase. The miniaturization of devices demand acquisition of multifunctionalities in the same materials or substrates and develop different functions in the same framework. This offers the possibility of using a different type of functional material on the same substrate to create a System on Chip device (SoC) with various functionalities applied to different substrate areas. For achieving such a multifunctional structure, semiconductor and FE are two critical elements because FE thin films can give high dielectric constant, tunability and piezoelectricity which are important for various device functionalities. The processing temperature of semiconductors is lower, and FE thin films are higher, combining the same device with these two materials is difficult. Thus, decreasing the processing temperatures of ferroelectric thin films is the key concept for the hetero material based high-quality device development. Hence an understanding of ways to lowering the processing temperatures of ferroelectric thin films is crucial.

Lasers made it easy to dream of lowering the crystallization temperature of these type of insulating thin films with high band width. Energy can be directed to a needed region in the device processing step without damaging the other components. Therefore, the initiative is taken in the present study to reduce the crystallization temperature of ferroelectric thin films to make them consistent with the processing of multifunctional devices. Generally, ferroelectrics are wide bandgap materials, and the ultraviolet wavelength lasers are therefore capable of crystallization by non-thermal route. Laser crystallization has been commonly used in semiconductor technology to benefit selective absorption at lower temperature of the substrate. Also, the irradiation area can be freely chosen without other regions being heated. Some of the earlier pioneering works in this

field are examined in this section. It could be noticed that constant effort has been made to reduce the temperature applied on the semiconductors or semiconductor components.

The major speciality of LIC lies in its rapid heating and cooling rates, for example, the heating rate of laser annealing is approximately 100 times more than that of rapid thermal process (RTP) (with only surface heating of film without influencing the substrate). Heating through Laser can be localized to the surface layer, which reduces the film-substrate interfacial interaction that occurs at higher temperature, resulting in improved electrical properties in such cases. The pulse duration used in typical laser annealing is in the range of 10-30 ns, and hence in such a short time the heat cannot diffuse to longer distance. Hence laser annealing process are confined to the thin surface layer. Hence, the substrate is not affected by the annealing process.

Different methods have been tried to integrate FE films (thick/thin) onto the low temperature substrates in the past. The noticeable techniques are (i) bombardment of nanoparticles of FE powders on a polymer or low temperature substrates at very high velocity to form as a thick film that yields bulk properties at low temperature [29,30] (ii) high temperature deposition of the FE films and then etching the substrate to reduce its thickness and integration with low temperature polymer substrates[31] and (iii) complex film transfer process to transplant FE films from high temperature substrates to another low temperature flexible substrates [32].

To reduce the processing temperature and time, FE thin films can be deposited at room temperature and annealed by using microwave annealing (MWA), rapid thermal annealing (RTA) and laser induced crystallization (LIC). MWA and RTA are efficient to reduce the processing time to a few minutes but failed to decrease the processing temperature significantly. On the other hand, LIC is successful in reducing not only processing time but also temperature. In LIC, chemical reactions (photochemical effects)

can be induced by lasers which act as a heat source (photothermal effects) due to their intense and directed energy [33,34].

Importance of crystallization at low temperature in BST thin films

- ➤ Strong voltage depended dielectric constant and low dielectric losses make

 Ferroelectric materials an attractive candidate for microwave devices. Other

 important applications include ferroelectric memory devices and MEMS systems.
- ➤ BST thin films are widely investigated for developing tunable microwave devices, varactors, filters, delay lines and phase shifters. Large leakage current limits the performance of these devices.
- The growth of BST thin films on various substrates are possible and numerous cost-effective deposition methods are available to grow BST thin films.
- ➤ BST can be grown on Si wafers and platinum-coated silicon in single phase with superior dielectric properties and the only drawback is the higher processing temperature of BST thin film. In fabrication process for nanoscale components often we need to limit the maximum process temperature to 300°C. Therefore, non-thermal routes to crystallizing these films became necessary.

1.4.1 Literature survey

Laser-induced crystallization (LIC) is well investigated in semiconductor industries and there are many reports on laser annealing of silicon by using excimer laser. The mechanism of phase transformation and the resulting microstructure of Si films crystallized by LIC on SiO₂ have been identified. It is shown that there is a rise in grain size as the energy density increases in the low energy density regime. They found that the transition region is a good regime for creating broad grain-sized polycrystalline Si [35]. For the laser-induced crystallization (LIC) of Sb₂S₃, Sb₂Se₃, and Sb₂Te₃ semiconductor films, continuous-wave laser power is used. They found that in all three substances, the

photothermal process is responsible for the change in phase. Depending on the film thickness, the power needed for optical contrast at an irradiated site will depend. The optimized power density is 100 W/cm² for the above samples [36].

However, this technique was found to be suitable and useful also for the ferroelectric thin films. And because of this, different research groups from all over the world are trying laser annealing for different ferroelectric materials since ferroelectric thin films exhibit voltage dependent dielectric properties (tunability) and can be used in ferroelectric memory devices and microelectromechanical systems (MEMS). Laser annealing is carried out on various materials like PZT, PLZT, BZN, LMO, ZnO, BST, etc. [37-57]. In general, ferroelectric thin films, which were crystallized at high temperatures (700°C) show the best functional properties [58,59]. Therefore, this laser assisted process must yield equivalent results for best results.

Bharadwaj et al. [39] reported the laser annealing conditions to get phase pure perovskite PLZT thin films, which are substrate temperatures of 250°C and higher, repetition rate of 10 Hz, Oxygen partial pressure of 10-200 mTorr with laser energy of 100 mJ. Polycrystalline perovskite films were obtained with no observed secondary phase formation. The dielectric constant and loss tangent values of PLZT films crystallized with laser at 10 kHz were 406 and 0.027, respectively, and are close to rapid thermal annealed values of PLZT thin films. These results demonstrate the potential of the excimer laser crystallization of amorphous ferroelectric PLZT films at quite low relative temperatures.

Bharadwaj et.al. [40] deposited PLZT thin films using RF-magnetron sputtering on LaNiO₃ coated silicon substrate. The kinetics of laser annealed films were investigated for the substrate temperature below 400°C. For the crystallization process, a KrF Excimer laser with a pulse width of 20 ns and an energy density of 40 mJ/cm² was used. They found that with a time exposure of 0.1 to 1ms, 380-400 nm thick films can be fully crystallized. The

crystallization of films is observed without any secondary phases for a minimum number of shots. Laser annealed samples gave good dielectric properties.

The LIC is a standardized and well-accepted process for amorphous silicon crystallization. An elevated temperature of about 300-400°C for ferroelectric thin films is found to be useful for PZT. The optimization of the LIC process depends heavily on the pulse width, the laser wavelength, the laser energy density, the substrate thermal conductivity, and the substrate's temperature during the annealing process [41-44]. Nd-YAG, Excimer, and femtosecond lasers are used for the annealing process, out of which Nd-YAG costs the least and gives the largest number of wavelengths. There are not many studies reported so far for other ferroelectric thin films.

Rajashekhar et. al. [45] from the same group reported the simultaneous pulsed-laser heating during growth of PZT (52/48) thin films on PZT (30/70) seeded platinized silicon substrates at a substrate temperature of ~370°C with energy density 55 mJ/cm². Once crystalline films were made, the TEM measurements showed porosity separated at the grain boundaries. In terms of transient heating from the pulsed laser deciding the nucleation events, the evolution of film microstructure is defined, while the energy of arriving species dictates grain growth. It was shown that in lateral densification and in affecting grain sizes, energy of the plume species played a dominant role.

Considerable laser crystallization work was also performed in BST compounds, in addition to PZT. The $Ba_{0.8}Sr_{0.2}TiO_3$ thin films were deposited on platinized silicon and glass substrates at $600^{\circ}C$ temperature and was found to be amorphous. The films are crystallized after laser annealing with room temperature. Here the author observed that the number of laser pulses is a key parameter for crystallization and without damage of the

film. There has also been research in progress to understand the film crystallization and associated mechanism [46].

To integrate BST thin film directly into system-on-package (SoP), reduction of processing temperature of the BST film is crucial. There are very few literatures on laser annealing of BST thin films. Halder et. Al., used a KrF excimer laser to crystallize BST thin films (thickness~95 nm), which were deposited by a chemical solution. These films were laser annealed with various fluence and laser pulses at a substrate temperature ranging from 25°C to 250°C. The films were crystallized above 100 mJ/cm² fluence. The 250°C-substrate temperature-maintained film showed crack free microstructure. With an increase in laser fluence, the films also demonstrated higher dielectric constant. A higher dielectric constant of 200 showed a better crystallization of the film annealed with 120 mJ/cm². [50]. The BST6 thin films crystallized at 300°C by Kang et. al. using excimer laser annealing (ELA) exhibited a single perovskite phase, high dielectric constant (143), low dielectric loss (0.028) at 1 MHz and low leakage current density (0.9 mA/cm²) [43].

Table 1.2. Laser annealing done on different materials and its parameters.

S. No	Material	Substrate	LIC temper ature	Thickness	Device fabrication (Yes/No)	Ref
1	Bi _{1.5} Zn _{0.5} Nb _{1.5} O _{6.5} (BZN)	Pt/Ti/SiO ₂ /Si substrates	400°C	300 nm	NO	37
2	Ba _{0.7} Sr _{0.3} TiO ₃	Pt-coated Si substrate	450°C	95 nm	NO	57
3	(Pb,La)(Zr _{0.30} Ti _{0.70})O ₃	LaNiO ₃ -coated Si substrates	400°C	380 to 400 nm	NO	40
4	Pb(Zr,Ti)O ₃	LaNiO ₃ -coated Si substrates	400°C	320 nm	NO	39
5	Pb(Zr _{0.52} Ti _{0.48})O ₃	(CMOS, polymers, platinized silicon substrates).	400°C	300 nm	NO	45
6	Ba _{0.6} Sr _{0.4} TiO ₃	platinum coated Si substrate	300°C	30-40 nm	NO	43
7	Ba _{0.6} Sr _{0.4} TiO ₃ (BST)	Pt/Ti/SiO ₂ /Si substrate	300°C	300 nm	NO	52
8	Ba _{0.8} Sr _{0.2} TiO ₃ (BST)	(LNO/SiO ₂ /Si) substrates	500°C	40-160 nm	NO	53
9	Pb(Zr,Ti)O ₃	Glass	Ambien t	600 nm	NO	54
10	Pb(Zr _{0.52} Ti _{0.48})O ₃	Pt/Ti/SiO ₂ /Si substrate	370°C	300 nm	NO	63
11	Pb (Zr _{0.52} Ti _{0.48})O ₃	(111) Pt/Ti/ SiO ₂ /Si substrate	350– 375°C	300-350 nm	NO	44
12	Al-ZnO	Glass	300- 500°C	180 nm	NO	48
13	Ba _{0.8} Sr _{0.2} TiO ₃	bare glass and platinized substrates	Dep 600°C LA-RT	250 nm	NO	46
14	Ba _{0.5} Sr _{0.5} TiO ₃	Pt/Ti/SiO ₂ /Si	300°C	600 nm	Yes	Present study

Effect of thin film thickness on Laser annealing:

There are many issues involved with the laser annealing (LA) of BST and other ferroelectric thin films. Film thickness also affects the laser annealing process and the depth of crystallization. In the recent report published by Queralto et. al. [53], they were able to obtain crystallization in BST8 thin films (BST/LNO/SiO₂/Si) at 500°C in the fluences ranging from 50 to 75 mJ/cm². They obtained uniaxial {00l} orientation in 40 nm fully crystallized film but for thicker 160 nm films, crystallization occurs only up to 70 nm after 12,000 pulses. Rest of the film remained amorphous. Lu et. al. [54] deposited 600 nm PZT thin films out of which up to 120 nm thickness of PZT was crystallized by using a KrF excimer laser.

Baldus et. al. [55] has done a series of experiments on laser annealing for BST systems by changing the number of pulses and the laser energy density to prevent cracks, which appears due to thermal stress. Full vertical crystallization of the thin films can be achieved by (1) increasing the dwell time of the laser pulses by extended-pulse laser annealing as suggested by Lai et. al. [56] (Pulse width of KrF excimer laser pulses was extended from 25 to 374 ns) and (ii) In Situ annealing, in which two laser sources can be used, one for the ablation and a second one for the laser annealing. The delay in arrival of irradiation pulse with respect to ablation pulse can provide a uniformly crystallized thin film.

1.4.2 Mechanism of Laser Annealing: Lattice Mending Theory

The incident laser light can be absorbed, transmitted, or reflected based on the material's optical properties. The photon energy of KrF Excimer laser (λ =248 nm) is ~5 eV, and the bond energy for the Ba-O, Sr-O, and Ti-O are 5.9, 4.7, and 6.9 eV, respectively. The Sr-O bond energy is comparable to the photon energy; hence laser annealing is due to the photochemical process of laser-material interaction [51]. By just considering these

bond energy values, a simplistic realization would be of breaking the "Sr-O bond of amorphous matrix" to restructure/orient it as a new "Sr-O bond of crystalline" BST.

P-H Huang [60], et al. presented a scheme for the laser annealing process in copper. They proposed that when laser light is incident on the material it generates a shockwave, and when this shockwave meets a pore/defect region, the kinetic energy of the wave is reduced. This reduction in energy can trigger the collapse of this pore/defect and hence mending the lattice. A similar argument in the case of BST annealing may be stated as follows. The laser annealing in BST could be proceeding via breaking of the Sr-O bond and healing around formed pore/defects by a non-thermal method, by pressure waves excited with KrF-Excimer laser irradiation.

For a laser beam of 5eV, when incident onto the material's surface, the photon energy transfer depends on their bandgap energy (Eg). Generally, the energy of the incident normal light photons (hv) induces two types of electronic transitions (viz. intraband and band to band). If the photon energy is less than the bandgap of the ceramics (hv<Eg), the intraband transition only will occur. In this process, absorption of photons is possible, which is weakly coupled and as a result, is not favorable for ceramic thin film annealing. Whereas in the other case, if the photon energy is higher than the bandgap of the ceramics (hv>Eg), the absorption is much higher (i.e., stronger coupling) than the earlier case, and the excess photon energy (hv-Eg>0) is transformed into phonons, thus heating up the ceramic thin films [39].

The laser light incident on the material can strongly displace the electrons and produce a temporarily and spatially localized electron plasma in the material. This plasma relaxes via electron-phonon and phonon-phonon coupling and induces a massive pressure on impacting material and trigger collisional or collisionless plasma process depending on the intensity of the incident laser beam. For λ =248 nm; representing E = 5 eV is much

above BST optical band gap = 3.5 eV, thereby fulfilling the primary criteria of significant laser photon absorption (i.e., strong coupling). Also, the atomic electric field strength of materials is generally ($\sim 10^{11}$ V/m) is of approximately similar strength to that of the applied laser. Thereby physically the photon electric field associated with the applied laser can compete with material's electronic environment, an atom's own electric field to generate a plasma. In short, using the laser of appropriate wavelength, a strong coupling in both energy and the electric field of materials in one go is realized.

Moreover, the pulsating nano-second laser shots irradiation helps maintain the electric field produced by the laser in generating the plasma. This entire process is isochoric, leading to induced localized intense pulsating pressure, which increases/decreases, leading to a pressure wave. The rarefield low-pressure regions (i.e., materials relaxed portions) in materials are identified as suitable localized regions for having crystal nucleation supported by energy minimization studies [60,62]. A relation connecting the pressure generated with radiation intensity is obtained by using a 1-D plasma model as follows [61].

$$P = 1.5 I_{abs}^{3/4} for \lambda = 0.26 \mu m$$
 1.3

The amorphous to crystalline phase transition induced by low-intensity laser radiation (<10¹³ W/cm²) could be understood in terms of hydrodynamics by solving the fluid dynamic conservation equation. This equation's solution for low fluence gives small values of temperature and pressure, and such shock waves are often called weak shocks. These weak shocks can induce the transformation of material from amorphous to the crystalline phase.

Once nucleation happens, since the whole process is non-thermal, the nucleation sites' population takes over its dissipation. Finally, these fluctuating crystal nuclei

gradually contact each other by the aggregation to develop into a crystalline region. In the presence of the laser irradiation, these newly developed crystalline regions continue to grow until the complete crystallization of the laser-irradiated area is achieved.

To further understand the solid-state lattice mending in these materials, we need molecular dynamic (MD) simulation. These simulations often does not represent realistic experimental conditions. For instance, classical Molecular simulation omits the effect of electrons and purely works on atomic contributions. Another difficulty in performing MD simulation involves choosing appropriate potential for a complex oxide material system and other relevant modeling parameters. Pei-Hsing Huang et al. proposed a modified continuum—an atomistic approach for copper annealed using femtosecond laser pulse and evaluated the pressure-induced lattice mending process. They could identify three distinct phases of laser annealing, namely the incubation stage of dislocation nucleation, the plastic deformation stage, and finally, the lattice recovery stage. Further development in molecular simulation or sophisticated experiments is required to formulate a more comprehensive understanding of laser-induced crystalization [62].

1.5 Motivation of the Thesis

Barium Strontium Titanate (BST) can be grown on Si or platinized silicon with good dielectric properties and the main drawback is the higher processing temperature of BST thin film. In nanoscale components fabrication process, we need to limit the maximum temperature to about 300°C. Therefore, non-thermal routes to crystallizing these films become necessary. The laser induced crystallization (LIC) is of current research interest because of the limited fundamental understanding available about this process and their technological importance. Laser crystallized BST on silicon opens up the possibility of system on a chip (SOC) or a system in package (SIP) since the temperature of deposition

has been lowered to make it compatible with the already existing processes in silicon technology.

1.6 Objectives of the Thesis

- ➤ To understand the growth process of BST thin films deposited on various substrates using Pulsed Laser Deposition (PLD) technique and study its correlation with microstructure and microwave dielectric parameters such as dielectric constant, loss and tunability.
- → To achieve BST thin film with as high a tunability in microwave frequencies as possible.
- ➤ To optimize the laser annealing parameters in order to reduce the crystallization temperature of BST thin film and achieve crack free BST thin films with good microstructure using a laser annealing method.
- ➤ To achieve the full depth crystallization of the BST thin films using a layer-by-layer deposition of the film and laser annealing after each stage of deposition (all at 300°C).
- ➤ To get similar electrical and microwave dielectric properties for laser annealed BST thin films at 300°C, compared to the conventional annealed BST thin films (annealed at 700°C).

1.7 Organization of Thesis

The thesis is organized as follows

Chapter 1: Introduction

In this chapter a brief introduction to the varactors, and fundamentals of dielectric materials and tunable ferroelectric materials for microwave device applications are reported. An extensive literature review of laser annealed thin film ferroelectrics including BST thin film is carried out. The variety of previously used experimental techniques which are related to conventional crystallization approaches like in-situ annealing, thermal annealing, rapid thermal annealing, and laser annealing process are surveyed. Finally, the motivation and objective of the work and organization of the thesis are presented.

Chapter 2: Experimental Procedures

This chapter describes the sample preparation and characterization techniques utilized for doing the work presented in the thesis. The Barium Strontium Titanate (BST) ceramic target is prepared and used for thin film deposition. The importance of several process parameters in PLD during the thin film deposition process and laser annealing are systematically detailed out along with the characterization techniques that are to be used. The working principle and procedure of the following instruments and techniques are briefly explained: 1) Structural characterization techniques like XRD, Raman Spectroscopy, and TEM, 2) Microstructural studies with FESEM and TEM 3) Optical bandgap studies with UV/VIS/NIR spectrometer, and 4) Microwave dielectric properties study with Vector Network Analyzer (VNA). The measurement procedure for electrical and microwave dielectric properties are explained.

Chapter 3: In-situ crystallization of Ba_{0.5}Sr_{0.5}TiO₃ thin films

In chapter 3, details of Ba_{0.5}Sr_{0.5}TiO₃ (BST5) thin films deposited on (100) oriented MgO substrates using PLD are described. The deposition temperature is kept constant, and the oxygen working pressure and laser fluence are varied. Microwave dielectric properties of the thin films are measured using Inter Digitated Capacitor (IDC) test structure with VNA. It is found that the maximum tunability (in IDC configuration) is obtained at optimized oxygen working pressure and laser fluence. In this chapter, it is observed that the deposition conditions of oxygen working pressure and laser fluence are more helpful, leading to better tunability in BST5 films.

Chapter 4: In-situ crystallization of Ba_{0.6}Sr_{0.4}TiO₃ thin films

In this chapter, the role of laser fluence in improving the microwave dielectric properties of BST thin films is studied. Here, in-situ crystallization process of Ba_{0.6}Sr_{0.4}TiO₃ (BST6) thin films deposited with different laser fluences are discussed. This chapter explains the structural properties and formation of microstructures in these films, studied using XRD, FESEM and TEM. The optical properties are studied and the optical bandgaps are calculated by applying the Tauc relation on the transmission spectra. The microwave dielectric measurements of BST6 thin films are done using test circular patch capacitors on optimized films.

Chapter 5: Crystallization of BST thin films using laser irradiation at 300°C

In chapter 5, the laser crystallization of the amorphous Ba_{0.5}Sr_{0.5}TiO₃ (BST5) thin films are investigated. The BST5 thin films are deposited (at 300°C) using PLD on fused silica substrates and platinized silicon, and are found to be amorphous. The laser annealing process is done at 300°C temperature by varying the laser annealing parameters like no. of laser pulses used, repetition rate and laser energy density. Successful crystallization of BST

thin films at 300°C is achieved by laser annealing using KrF Excimer laser of 248 nm wavelength and pulse duration of 20 ns. Attempt was made to understand the effect of optimizing laser annealing parameters on BST thin films deposited and annealed at 300°C with the help of cross sectional TEM. The result of laser annealed thin films are correlated with that of conventional (deposited at 700°C) films.

Chapter 6: Full depth crystallization of BST with laser annealing of layers at 300°C

Chapter 6 discusses the full depth crystallization of Ba_{0.5}Sr_{0.5}TiO₃ (BST5) thin films by layer-by-layer (5 layers) deposition followed by laser annealing after every deposition, both at 300°C using a KrF excimer laser to yield films crystallized to 600 nm depth. Each layer was laser annealed using the optimized conditions described in Chapter 5. The phase formation and full vertical crystallization of BST5 thin films were confirmed by XRD patterns, Raman spectroscopy and UV-Vis-NIR study as well as TEM and SEM analysis. These layer-by-layer deposited and laser annealed BST5 thin films show good electrical properties and microwave tunability close to the tunability shown by conventionally deposited BST5 films (at 700°C).

Chapter 7: Conclusions and scope of future work

This chapter summarizes the outcomes based on the work reported in this thesis and discusses the future possible work which includes further optimization of laser annealing process to crystallize BST5 thin films at room temperature for opening up the scope of using it in flexible and wearable microwave devices.

References

- [1] G. Subramanyam, M. W. Cole, N. X. Sun, T. S. Kalkur, N. M. Sbrockey, G. S. Tompa, X. Guo, Ch. Chen, S. P. Alpay, G. A. Rossetti Jr., K. Dayal, L.Q. Chen and D. G. Schlom, Journal of Applied Physics 114, 191301 (2013).
- [2] A. K. Tagantsev, V. O. Sherman, K. F. Astafiev, J. Venkatesh and N. Setter, Permittivity, tunability and loss in ferroelectrics for reconfigurable high frequency electronics. In Electroceramic-Based MEMS (pp. 235-324). Springer, Boston, MA. (2005).
- [3] Spartak Sh. Gevorgian Alexander K. Tagantsev, Andrei K. Vorobiev, Tuneable Film Bulk Acoustic Wave Resonators, Springer-Verlag London (2013).
- [4] Robert A. York, Tunable Dielectrics for RF Circuits Multifunctional Adaptive Microwave Circuits and Systems M. Steer and W.D. Palmer, University of California at Santa Barbara, eds., Scitech Publishing (2009).
- [5] Aftab Ahmed, Irene A. Goldthorpe, and Amir K. Khandani, Applied Physics Reviews, 2, 011302 (2015).
- [6] N. Setter, D. Damjanovic, L. Eng, G. Fox, S. Gevorgian, J. Appl. Phys. 100, 051606, (2006).
- [7] P Bao, T J Jackson, X Wang and M J Lancaster, J. Phys. D: Appl. Phys. 41, 063001 (21pp) (2008).
- [8] Valasek, J. Phy.Rev 17,475(1921).
- [9] Venkata Saravanan, Crystalline Barium Strontium Titanate thin films on Amorphous Fused Silica Substrates for Frequency Agile Microwave Devices, thesis (2009).
- [10] A. J. Moulson and J. M. Herbert, "Electroceramics: Materials, properties, applications", chapman and hall, New Yok, USA (1997).
- [11] K. Sudheendran and K.C. James Raju, Voltage Tunable Microwave Dielectrics for Frequency and Phase Agile Devices, *Microwave Materials and Applications*, John Wiley & Sons, Ltd (2017).
- [12] A.K. Taganstev, V.O. Sherman, K.F. Astafiev, J. Venkatesh, N. Setter, Journal of electro ceramics, 11, 5(2003).
- [13] J.Y. Kim and A.M. Grishin Integrated ferroelectrics, 66, 291 (2004).
- [14] A. Dec, and K. Suyama, IEEE Transactions on Microwave Theory and Techniques,

- 46 (12), 2587–2596 (1998).
- [15] S.J. Lee, S. E Moon, M.H. Kwak, Y.T. Kim, H.C. Ryu, S.K. Han Appl Phys Lett, 82, 2133(2003).
- [16] I. Wooldridge, Westerner, P.A. Warburton, E.J. Romans, IEEE.Trans. Appl. Supercond, 9,3220 (1999).
- [17] G.H. Lin, R. Fu, S. He, J. Sun, X. Zhang, Sengupta, Mat.Res. Soc.symp. proc 720, (2002).
- [18] F.A. Miranda, Subramanyam, F.W. Vankeuls, R.R. Romanotsky, J.D. Warner and C.H. Muller IEEE Trans. On Microwave Theory and technique, 48,1181(2000).
- [19] Y. Zhu and L.C. Sengupta US patent No. US6,686,817B2 (2004).
- [20] S.R. Chandler, I.C. Hunter and J.G. Gardiner, IEEE Guided Wave Letters, 3,70 (1993).
- [21] S.P. Voinigescu, D.S. Mcpherson, F. Pera, S. Szilagyi, M. Tazlauana and H. Trani, International Journal for high-speed electronics and systems, 13, 27 (2003).
- [22] G. H. Haertling, J. Vacuum Sci. and Tech. A. 9, 414 (1991).
- [23] A. K. Tagantsev, V. O. Sherman, K. F. Astafiev, J. Venkatesh, and N. Setter, J. Electroceram. 11, 5 (2003).
- [24] A. Vorobiev, P. Rundqvist, K. Khamchane, and S. Gevorgian, Appl. Phys. Lett. 83, 3144 (2003).
- [25] A. Tombak, J.P. Maria, F.T. Ayguavives, Z. Jin, G.T. Stauf, A.I. Kingon and A. Mortazawi IEEE.Trans. Microwave Theory and Tech,51,462 (2003).
- [26] Jayesh Nath, Dipankar Ghosh, Jon Paul Maria, Angus. I. Kingon, Wael Fathelbab, Paul D. Fran Zon Michael. B. Steer, IEEE Trans. Microwave theory and technique,53,2707 (2005).
- [27] L.Y. Vicki Chen, Roger Forse, D. Chase, R.A. York IEEE MTT-S Digest 261(2004).
- [28] www.paratek.com
- [29] Palneedi, H., Peddigari, M., Hwang, G. T., Jeong, D.Y. and J. Ryu, *Adv. Funct. Mater.* 28, 1803665 (2018).
- [30] Peddigari, M. et al. ,ACS Appl. Mater. Interfaces 10, 20720–20727 (2018).
- [31] S. Abel, F. Eltes, J. E. Ortmann, A. Messner, P. Castera, T. Wagner, D. Urbonas, A. Rosa, A. M. Gutierrez, *Nat. Mater.* 18, 42–47 (2019).
- [32] Y. J. Ko, D. Y. Kim, S. S. Won, C. W. Ahn, W. Kim, A. I. Kingon, S. Kim,

- J.H. Ko, and J. H. Jung, ACS Appl. Mater. Interfaces 8, 6504–6511 (2016).
- [33] H. Palneedi, J. H. Park, D. Maurya, M. Peddigari, G.T. Hwang, A. Venkateswarlu, J. W. Kim, J.J. Choi, B.D. Hahn, S. Priya, K. J. Lee, and J. Ryu, Adv. Mater. 30, 1705148 (2018).
- [34] Bäuerle, D. *Laser Processing and Chemistry*. (Springer Science & Business Media) (2013).
- [35] James S. Im, H. J. Kim, and Michael O. Thompson, Appl. Phys. Lett. 63, 1969 (1993).
- [36] P Arun, A G Vedeshwar and N C Mehra, J. Phys. D: Appl. Phys. 32, 183(1999).
- [37] J. G. Cheng, J. Wang, T. Dechakupt and S.T. McKinstry, Appl. Phys. Lett.,87,232905 (2005).
- [38] T. Nakajima, T. Tsuchiya, M. Ichihara, H. Nagai and T. Kumagai, Appl. Phys.Express, 2,023001 (2009).
- [39] S.S.N. Bharadwaj, T. Dechakupt and S.T. McKinstry, H. Beratan, *J. Am. Ceram.Soc.* 91, 1580–1585 (2008).
- [40] S. Bharadwaja, J. Kulik, R. Akarapu, H. Beratan and S.T. McKinstry, IEEE Trans. Ultrason. Ferrolelect. Freq. Control, 57, 2182-2191(2010).
- [41] Y. Zhu, J. Zhu, Y. J. Song, and S. B. Desu, Appl. Phys. Lett., 73, 1958 (1998).
- [42] T. Miyazaki, T. Imai, N. Wakiya, N. Sakamoto, D. Fu, H. Suzuki, Mater.Sci. and Eng. B 173, 89 (2010).
- [43] M. G. Kang, K. H. Cho, S. M. Oh, Y. Ho Do, C. Y. Kang, S. Kim, S.J.Yoon, Current Applied Physics 11, S66 (2011).
- [44] S. S. N. Bharadwaj, F. Griggio, J. Kulik, and S. Trolier-McKinstry, Appl.Phys. Lett. 99, 042903 (2011).
- [45] A. Rajashekhar, H.-R. Zhang, S. Bharadwaja Srowthi, I.M. Reaney and S.T. McKinstry, J. Am. Ceram. Soc., 99, 43–50 (2016).
- [46] J. P. B. Silva, A. Khodorov, A. Almeida, J. Agostinho Moreira, M. Pereira,M. J. M. Gomes, Appl. Phys. A 116, 1271–1280 (2014).
- [47] S.U. Park, J.H. Koh, J. Alloys and Comp. 615,1032–1036 (2014).
- [48] W.T. Hsiao, S.F. Tseng, C.K. Chung, D. Chiang, K.C. Huang, K.M. Lin, L.Y. Li, M.F. Chen, Optics & Laser Technology, 68, 41–47 (2015).
- [49] S.O. Elhamali, W.M. Cranton, N. Kalfagiannis, X. Hou, R. Ranson, D.C.Koutsogeorgis, Optics and Lasers in Engineering, 80, 45–51(2016).

- [50] S. Halder, U. Boettger, T. Schneller, R. Waser, O. Baldus, P. Jacobs, M. Wehner, Mater. Sci. Eng. B, 133, 235–240 (2006).
- [51] A. Queralto, A. Perez Del Pino, M. De La Mata, J. Arbil, M. Tristany, A. Gomez,X. Obradors and T. Puig, Appl. Phys. Lett., 106, 262903 (2015).
- [52] M.G. Kang, K.H. Cho, Y.H. Do, Y.J. Lee, S. Nahm, S.J. Yoon and C.Y.Kang, Appl.Phys. Lett., 101,242910 (2012).
- [53] A. Queraltóa, A. P. del Pino, M. de la Mata, M. Tristany, X. Obradors, T. Puig,S.T. McKinstry, Ceramics International, 42, 4039–4047 (2016).
- [54] X.M. Lu, J.S. Zhu, W.S. Hu, Z.G. Liu and Y.N. Wang, Appl. Phys. Lett., 66, 2481-2483 (1995).
- [55] O. Baldus and R. Waser, Appl. Phys. A, 80,1553 (2004).
- [56] S.C. Lai, H.T. Lue, K.Y. Hsieh, S.L. Lung, R. Liu. T.B. Wu and P.P Donohue and P. Rumsby, J. Appl. Phys., 96, 2779-2784 (2004).
- [57] O. Baldus and R. Waser, J. Eur. Ceram. Soc., 24,3013-3020 (2004).
- [58] K. Kim and S. Lee, J. App. Phys. 100, 051604 (2006).
- [59] P. Muralt, Piezoelectric thin films for MEMS, Integr. Ferroelctr. 17, 297-307 (1997).
- [60] Pei-Hsing Huang and Hsin-Yi Lai, Nanotechnology, 19, 255701 (11pp) (2008).
- [61] J. Romain. GENERATION OF HIGH SHOCK PRESSURES BY LASER PULSES. Journal de Physique Colloques, 45 (C8), pp.C8-281-C8-289, (1984).
- [62] S. Ramakanth, Magnetism and Laser Induced Crystallization of BaTiO3, and Ultrafast Demagnetization of Ni films, Thesis, (2017).
- [63] A. Rajashekhar, S. S. N. Bharadwaja, and Susan Trolier-McKinstry, Applied Physics Letters 103, 032908 (2013).

Chapter 2

Experimental Procedures

This chapter deals with sample preparation and characterization techniques utilized for doing the present thesis work. The lab-made Barium Strontium Titanate (BST) target is used for the deposition of thin films in the pulsed laser deposition (PLD) method. Also, the importance of several process parameters in PLD during the thin film deposition process and laser annealing are systematically detailed out. Then, the characterization techniques are presented. These characterization methods are divided into subsections such as structural, microstructural, optical and microwave dielectric property characterizations.

2.1 BST ceramic target preparation

The BST stoichiometric target is prepared by a solid-state reaction method [1-3]. The essentiality of getting optimized target is foremost important in developing the high-quality thin-film samples with reproducible results.

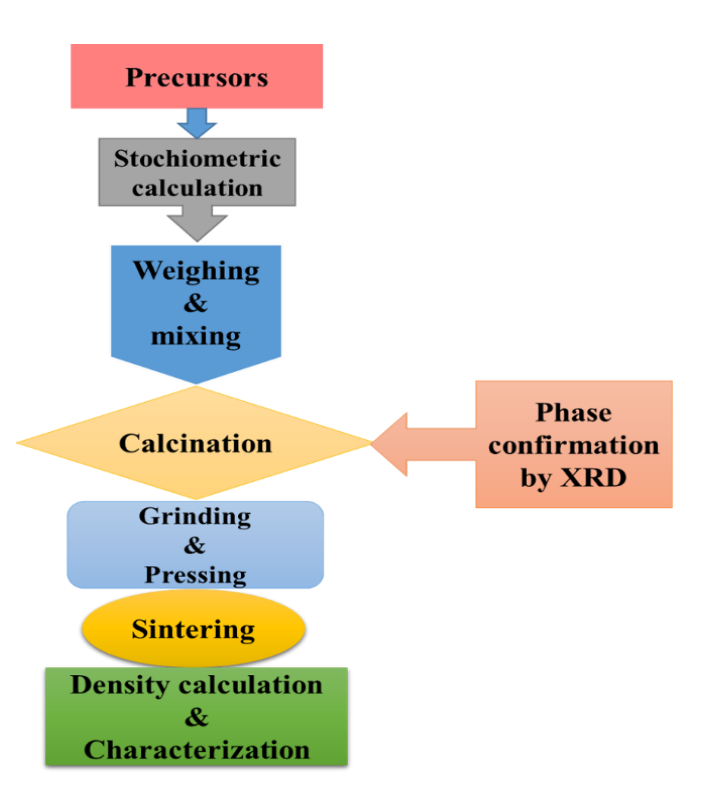


Fig.2.1. Schematic diagram of steps in solid state reaction method

In this work, the high purity reagents BaCO₃, SrCO₃ and TiO₂ (Sigma-Aldrich, purity 99.99%, USA) were used for preparation of Ba_{0.5}Sr_{0.5}TiO₃ ceramic target. The chemical reaction for the formation of Ba_{0.5}Sr_{0.5}TiO₃ is given by

$$0.5BaCO_3 + 0.5SrCO_3 + TiO_2 \longrightarrow Ba_{0.5}Sr_{0.5}TiO_3 + CO_2 \uparrow$$
(2.1)

These powders are mixed by ball milling (Retsch PM 100) for 2 hrs. Further, this mixed powder is calcined at 1000°C in a microwave sintering system with a dwell time of 30 minutes. The heating rate is 25°C/min. The calcined powder samples were again ball milled for 6 hrs. to reduce the particle size to enhance the density of the ceramic target, as shown steps in from fig.2.1. The fine powders are used for making PLD targets by adding 1% PVA (Poly Vinyl Alcohol) as a binder. The disc-shaped pellets with 25 mm diameter and 3 mm thickness were prepared using uniaxial press by applying a pressure of 2 MPa.

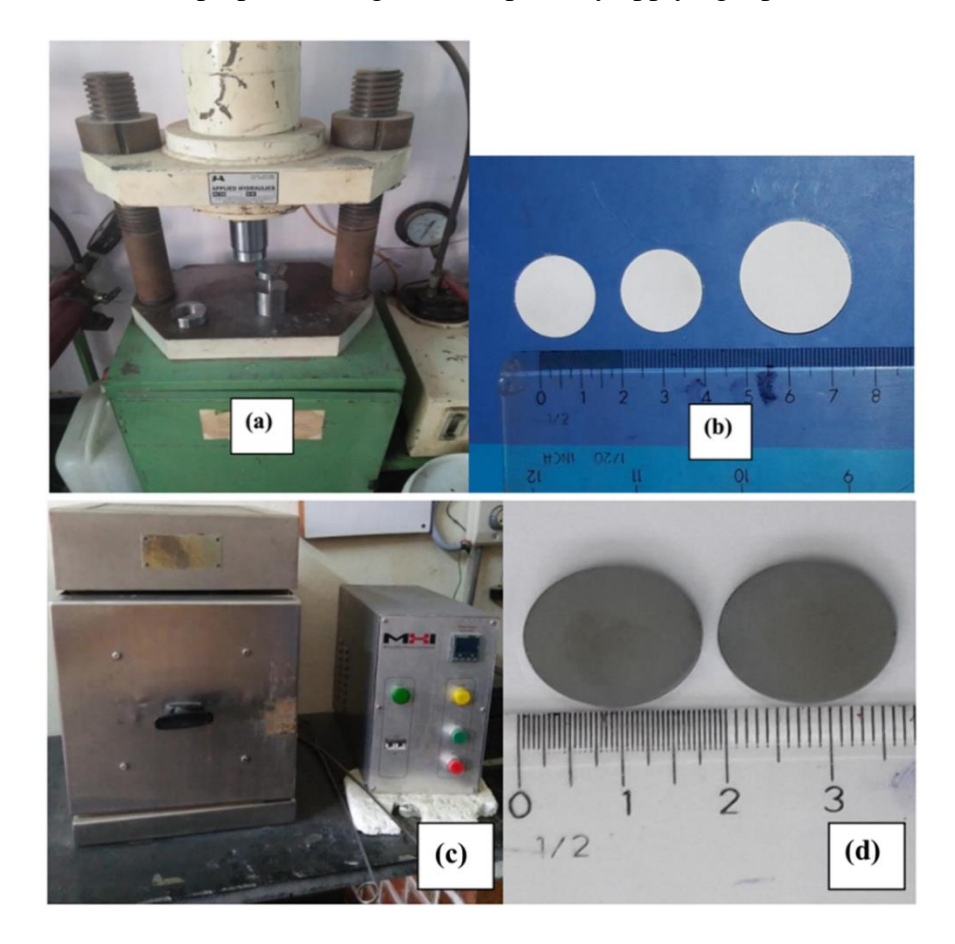


Fig.2.2. (a) Uniaxial Pressing (b) Green Pellets (c) High Temperature furnace, (d) Sintered Target.

The pellets were heated to 500°C at a heating rate of 2°C/minute for PVA binder evaporation. The prepared pellets were sintered at the optimized temperature of 1400°C for 2 hrs. with a heating rate of 5°C /min in the conventional furnace as shown in fig. 2.2. Both side surfaces of sintered BST targets were polished to avoid surface contamination [1-3]. In this work, for calcination, we used a microwave-assisted heating process in which the powders absorb the microwave energy with the help of SiC susceptors and get heated up. It means that heating of the sample happens fast with the susceptors accepting the microwave energy first and then heating the entire volume [4]. A similar procedure is utilized to fabricate BST6 target. XRD and FESEM are used to analyze the phase and microstructure of BST5 ceramic samples.

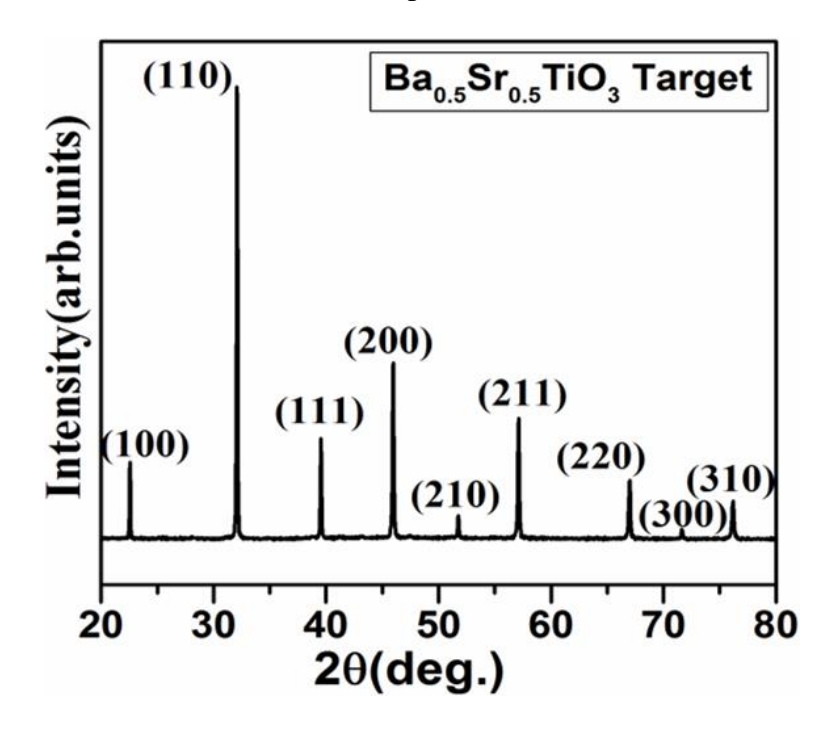


Fig.2.3. X-ray diffraction pattern of Ba_{0.5}Sr_{0.5}TiO₃ target.

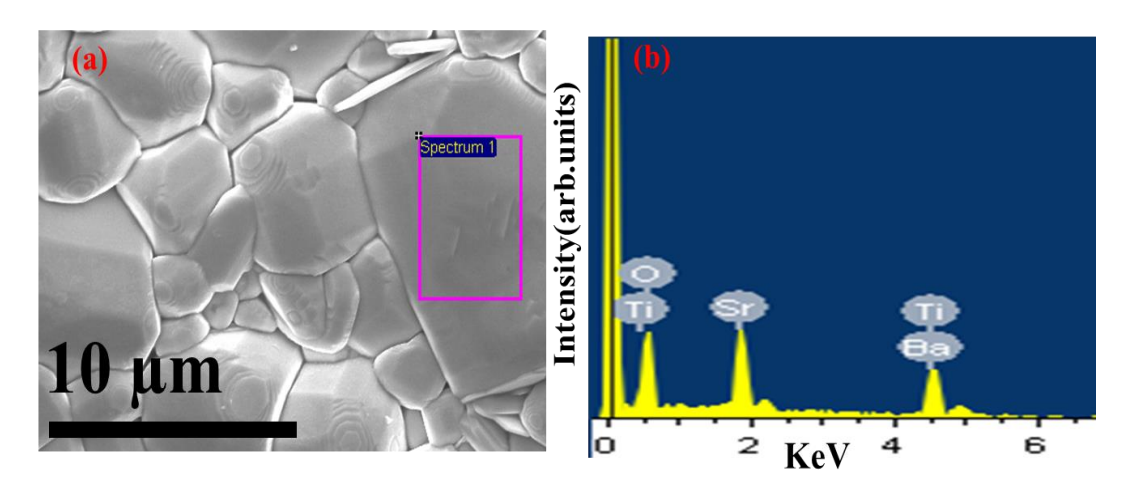


Fig.2.4. (a) FESEM image and (b) EDAX of Ba_{0.5}Sr_{0.5}TiO₃ sintered target.

The phase and structural properties of the Ba_{0.5}Sr_{0.5}TiO₃ (BST5) target were studied by X-ray diffraction (Bruker D8 Discover) at 40 kV and 30 mA with a Cu Kα radiation source of wavelength ~1.5406 Å as shown in fig. 2.3. The XRD pattern of this BST5 target matched well with the standard data (JCPDS file # 39-1395) and indexed as a cubic structure with *the Pm3m* space group. Fig 2.4(a) shows the FESEM image and fig. 2.4(b) EDAX of the BST5 sintered target. From the EDAX, BST5 target confirms the presence of elements Ba, Sr, Ti, and O without any impurity. The atomic percentage of Ba, Sr, Ti, and O are 12.58, 11.74, 20.7, and 54.97, respectively. It also confirms the stoichiometric ratio of elements Ti/Sr = 1.76 and Ti/Ba=1.64, as shown in fig. 2.4.

2.2 Pulsed Laser Deposition (PLD)

Pulsed laser deposition is a very simple technique for the deposition of thin films [5-8]. As the laser pulse is incident onto the dense target, the surface of the target absorbs the pulse energy resulting electronic excitation. Quickly this excited energy is converted into kinetic and heat energy resulting in target ablation. It results in an ejected ionized particle plasma plume. By adjusting the geometry of the target and laser beam, one can direct the plume path towards the desired substrate surface, resulting in the deposition of the thin film on the substrate as per the requirement. The plume generation and

expansion is a very complex process which involves several competing mechanisms. During the deposition of thin films, the chamber has to be kept in a vacuum to avoid plume scattering and the deposition of undesirable species on the surface of the substrate [5-8].

Advantages PLD method:

- The numerous wavelengths and power densities accessible allows the process to ablate many material or materials combinations by selecting the appropriate laser wavelength selection to match the absorption properties of materials.
- Epitaxial growth of thin films at a lower temperature.
- Atoms arrive in bunches and allowing for much more controlled deposition.
- Minimum contamination.

Various characteristics are mentioned below to distinguish PLD from other film- growth techniques and achieve a special role for the deposition of oxide and multi-component materials [5-8].

- Transfer of the stoichiometry of materials: Under proper adjusting of laser fluence, the film will possess the same composition of the target.
- Uniform thickness of thin films: Due to the highly forward-directed nature of the laser ablated plume, PLD films are uniformly thick only in a narrow region and because of this, all the films were grown on a small area (1cm × 1cm) substrate where uniform thicknesses are achieved.

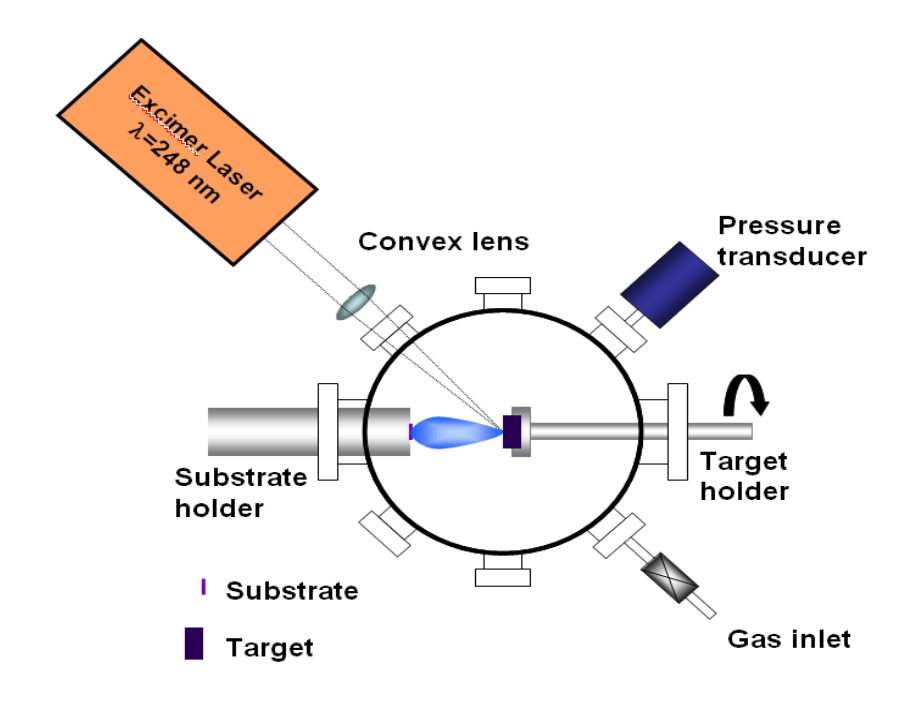


Fig 2.5. Schematic diagram of Pulsed Laser Deposition (PLD) system.



Fig. 2.6. Pulsed laser deposition (PLD) set up with high vacuum (HV) chamber.

2.3 Deposition of BST thin films by PLD

In this work, the BST films were deposited on an amorphous fused silica substrate by the PLD system, as shown in fig.2.6. Here, we use the 20 ns pulse width KrF Excimer laser of wavelength 248 nm (Coherent-Compex Pro 102 F) with a 5 Hz repetition rate. The deposition process of BST films are carried out in a spherical chamber (Excel Instruments, India). Initially, the chamber is evacuated to 5×10^{-6} mbar pressure using Turbo and backing pumps. The distance between the target and substrate is maintained at 5 cm. The target is set to rotate with a specific speed of 10 rpm. After deposition, the in-situ annealing is carried out for 30 min in the presence of oxygen gas. The complete deposition conditions are presented in Table 2.1.

A general scheme has been followed for all the thin film depositions in this thesis. Several substrates such as amorphous fused silica, platinized silicon (111) (Pt/TiO₂/SiO₂/Si), platinum-coated fused silica, platinum-coated silicon, platinum-coated sapphire, MgO (100) have been used to deposit BST thin films. Before the deposition process, the substrate cleaning was carried out using ultrasonic cleaning in acetone, isopropyl alcohol, and then rinsed with de-ionized water. It is then dried before loading into the deposition chamber. High purity O₂ gas was used as the background ambient gas during deposition. After the deposition, the films are slowly cooled down to room temperature in the same partial O₂ pressure (pO₂).

Table.2.1: The deposition conditions for BST films.

S.No	Parameter	Value
1	Laser source	KrF Excimer laser
2	Wavelength	248 nm
3	Laser model	(Coherent-Compex Pro 102 F)
4	Base vacuum	5×10 ⁻⁶ mbar
5	Target is set to rotate at	10 rpm.
6	Target and substrate distance	5 cm
7	Repetition rate	5 Hz
8	Fluence (or) Energy density	2 J/cm ²
9	Temperature	Varies
10	Substrates	Amorphous fused silica, platinized
		silicon (111) (Pt/TiO ₂ /SiO ₂ /Si),
		platinum- coated fused silica,
		platinum-coated silicon, platinum-
		coated sapphire, MgO (100)

2.4 Laser annealing set up

The Schematic diagram of the laser annealing set-up for annealing of deposited thin films is shown in fig. 2.7. The laser annealing set-up mainly consists of an excimer laser source, mirrors and annealing chamber.

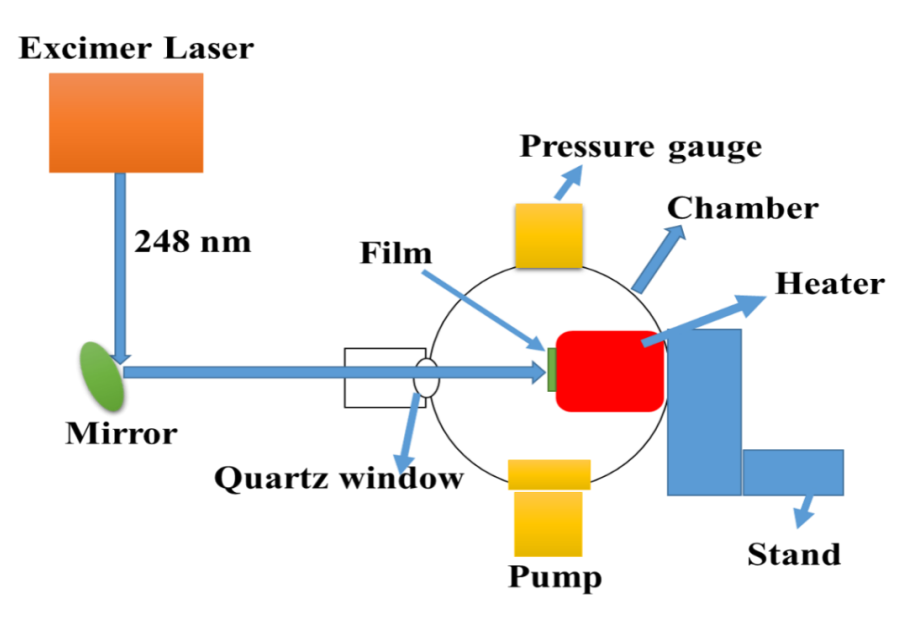


Fig.2.7. Schematic diagram of the laser annealing setup.

Thin films are directly exposed to the incoming laser to get the required energy density. The nucleation of crystalline phases is significantly affected by incident laser energy density, repetition rate and the number of shots used for irradiation. The annealing of the films was carried out at 300°C temperature and oxygen pressure used was same as that used for film deposition. Fig.2.8 shows the experimental laser annealing setup at the University of Hyderabad, which was used for the laser annealing study.

The Kr-F excimer laser (λ =248 nm) was used as a laser source for annealing. Mirror was used to bend and direct the laser beam on the ferroelectric thin films inside the annealing chamber. The spherical chamber has a substrate heater with a temperature controller and attachments like pressure gauges (Dual Gauge) and pumps (Rotary and Turbo) etc. It will help to maintain sample purity and control over the atmosphere during the laser crystallization process. The heater is used for ferroelectric thin films to be kept at desired elevated temperatures inside the annealing chamber. Quartz window is attached to the chamber, and the laser beam is passed into the chamber through this window. Quartz material is stronger than glass, it can be used at high temperatures up to 1050°C and it has high transmission in the range of 190 – 2500 nm wavelengths. This annealing chamber is kept at desired elevated temperatures below 300°C. The thin films of various materials are directly exposed to the incoming laser with or without diverging to get the required energy density. The laser annealing chamber has been used for substrates like amorphous fused silica, platinized silicon (Pt/TiO₂/SiO₂/Si), platinum-coated fused silica, platinum-coated silicon, and platinum-coated sapphire in controlled atmosphere and temperatures.

Thin films are directly exposed to the incoming laser to get the required energy density. The nucleation of crystalline phases is significantly affected by incident laser energy density, repetition rate, and the number of shots used for irradiation. The annealing of the films was carried out at 300°C temperature and oxygen pressure used was the same

as that used for film deposition. Fig. 2.8 shows the experimental laser annealing setup at the University of Hyderabad, which was used for the laser annealing study.

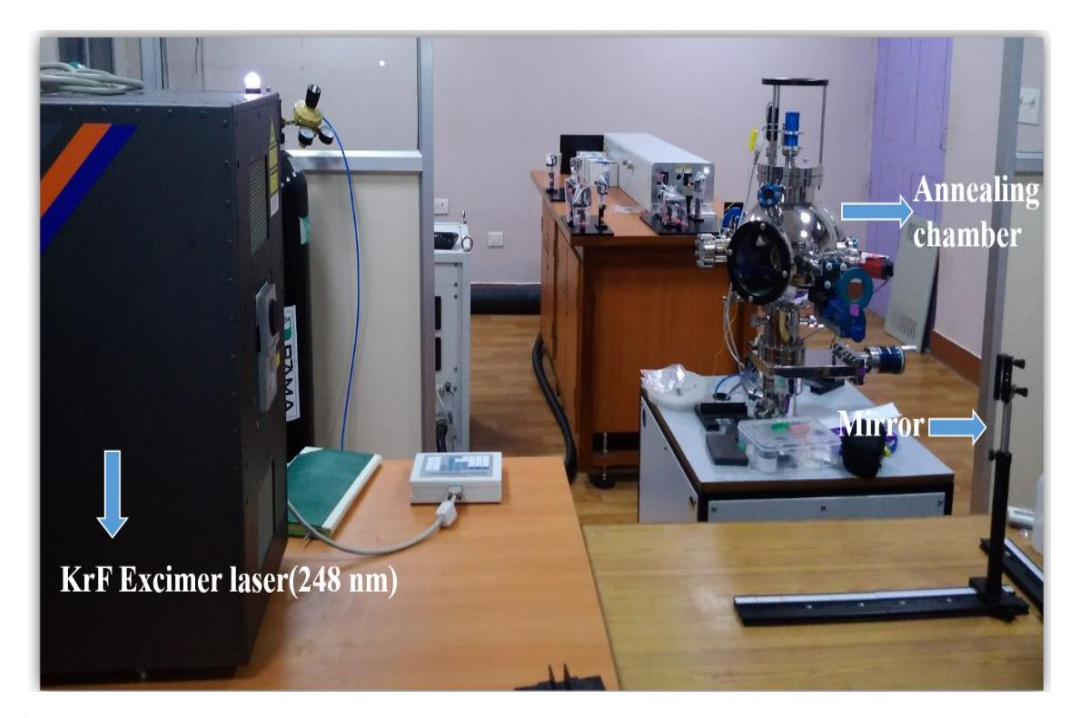


Fig. 2.8. Set-up for the laser annealing of thin films with the chamber and KrF- Excimer laser.

2.5 Characterization techniques

This section includes basic principles and the experimental techniques that are extensively used. Thin-film crystallinity and phase assessment are carried out by X-ray diffraction (XRD). Also, the film orientation and grown texture inferences from XRD will provide significant insights to understand their physical attributes like polarization, conductivity, and dielectric response. Chemical composition and purity are established by Energy Dispersive X-ray Spectroscopy (EDS). The morphology and microstructure of the thin film surfaces are studied using the Field Emission Scanning Electron Microscope (FE-SEM) and Transmission Electron Microscope (TEM).

2.5 Structural Characterization

2.5.1. X-ray Diffraction

X-ray diffraction is a powerful tool to obtain detailed information about the crystal structure and phase formulation of materials [9-12]. It helps in the determination of a given material's unit cell dimensions with absolute fractional coordinates of its constituent atoms. A variety of information such as crystallinity, phase or symmetry, lattice parameters, preferred orientation, defects, stress, strain, and average crystallite size can be extracted through careful analysis of the X-ray diffraction data [9-12].

A beam of accelerated electrons produced is allowed to fall on a metal target, usually Copper (Cu). These accelerated electrons knock off the electrons from the target atoms. X-ray photons are released when electrons from higher orbits jump to the vacant inner orbits. The energy of an ejected photon is a characteristic of the target material. For example, the characteristic wavelengths of copper are 1.5406 Å for CuKα₁ and 1.5443 Å for CuKα₂ [11]. According to Bragg's law, when X-rays are scattered from a crystal lattice, peaks of scattered intensity are observed.

The Braggs law is given by $2dsin\theta = n\lambda$ where d is the interplanar distance between the crystal planes, θ is the angle between the incident beam and sample crystal plane, n is diffraction order, and λ is the wavelength of the X-rays. When Bragg's law is satisfied, the reflected beams interfere constructively, failing, which leads to destructive interference.

The electrons that surround the atoms interact with the incident X-ray photons. X-ray powder diffraction is used in materials due to its non-destructive nature. The diffraction peak pattern can be utilized to identify the materials using the JCPDS (Joint Committee of Powder Diffraction Standard) database. The observed changes in peak width and its position can be used to obtain the crystallite size and phases [12].

Grazing angle Incidence-XRD:

For thin films, X-ray $\theta/2\theta$ scattering produces a weak signal from film and an intense signal from the substrate due to the penetration depth of X-rays. The problem is minimized by increasing the penetration depth in the film and reducing that in the substrate in Grazing incidence X-ray diffraction (GI-XRD) mode. The phase and structural properties of the deposited BST films are studied by X-ray diffraction (GI-XRD-Bruker D8 Discover is shown in fig. 2.9(b)) at 40 kV and 30 mA with a Cu-K α radiation source of wavelength ~1.5406 Å. The GI-XRD analysis was performed to check the composition and phase of grown films. In GI-XRD, the X-ray beam enters into the film with a lower incidence angle, which leads to an increase in the X-Ray path length in the thin film and reduction of it in the substrate. The higher penetration of the beam in the film gives a significant signal from the film. The main advantage of GI-XRD is that the electric field at the critical angle is amplified locally by a factor of four, making the signal stronger. The XRD patterns are recorded in the range of 20°- 80° Diffraction (GI-XRD) mode with the angle of incidence at 0.5°.

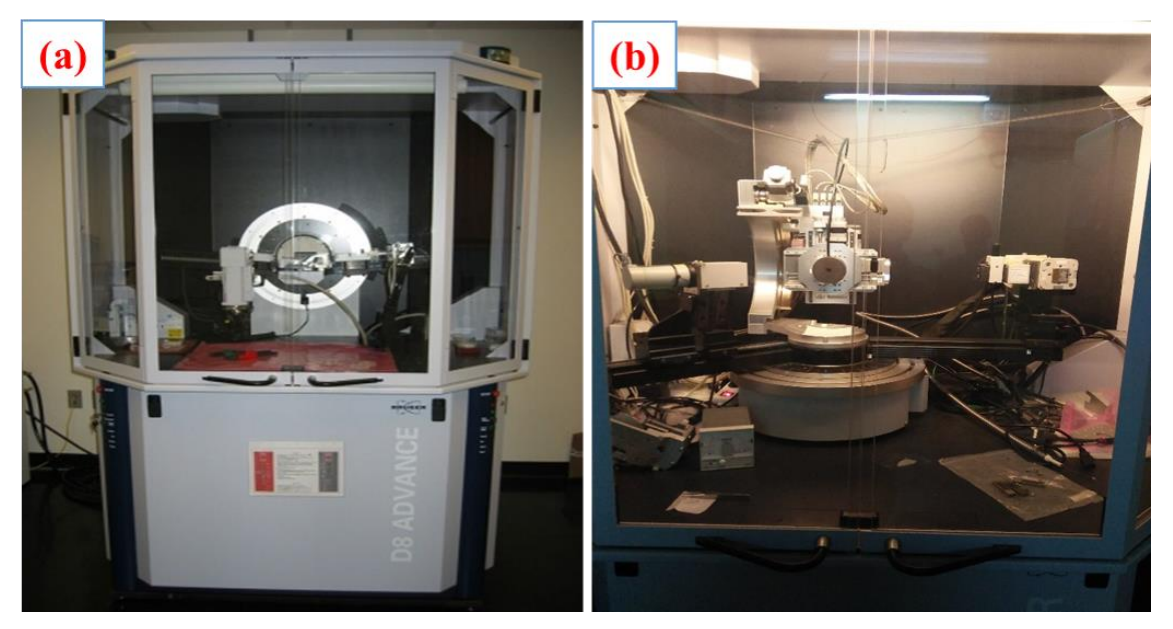


Fig. 2.9. (a) Bruker D8 advanced diffractometer for bulk (b) Bruker D8 discover for thin films (GIXRD).

Advantages of the XRD

(a) Phase Identification

XRD is the most effective technique used to identify the crystal structure and phase purity of the material. Every crystalline material has a specific diffraction pattern. The intensity of the peak and its position are features of a particular phase, and the pattern thus gives a fingerprint of a specific material [12].

(b) Crystallinity

XRD can also be used to identify the crystallinity of materials by comparing the integrated intensity of the background pattern to that of the sharp peaks [12].

(c) Crystallite Size:

Debye-Scherer Formula

The average crystallite size can be obtained using Debye-Scherer Formula [11,12]

$$D_p = \frac{k\lambda}{\beta\cos\theta}$$
 (2.2)

Where k=0.94, λ is the wavelength of the radiation, β is the full width at half maximum (FWHM), and θ is the angle or peak position.

2.5.2 Field Emission Scanning Electron Microscopy (FESEM)

Scanning Electron Microscopy is a tool to view the surface morphology of the samples. An electron beam is used to create a magnified image of the surface and the distribution of nanoscale crystallites owing to its excellent resolution in comparison to an optical microscope. The principle of this equipment is that the electrons emitted from a cathode by field emission at high energy is used for imaging. It is in several keV and is accelerated towards the condensing lens, which is focused on the sample with the help of an objective lens. The focused beam is scanned over the surface of the sample under observation by scanning coil. Different types of signals are induced when the electron beam hits each spot on the sample [9, 13, 14].

The signals mainly used for SEM image reconstruction are secondary electrons and backscattered electrons. The detector counts electrons and converts it into a two-dimensional image using incoming signals through the amplifier. The backscattered electrons are elastically scattered electrons that are used for imaging. The secondary electrons are also widely used for topographical imaging [13, 14]. In this work, the SEM images were recorded in an Ultra 55, Carl Zeiss microscope fitted with the Schottky FE Gun as the electron source. The electron accelerating voltage was 25 kV. The vacuum created in the system near the sample and at the gun is of the order of 10^{-6} mbar and 10^{-10} mbar, respectively. A photograph of the instrument is shown in fig. 2.10.



Fig.2.10 (a) Field emission scanning electron microscope (model: Carl ZEISS, Ultra55, Germany) (b) Gold coating sputtering unit for non-conducting samples.

The composition analysis of the BST thin films was carried out using the energy dispersive analysis of X-rays (EDAX) method in the scanning electron microscope [15].

2.5.3. Transmission Electron Microscope (TEM)

Transmission electron microscope (TEM) also uses very small wavelength electron beam for illumination. It has long cylindrical column of length 2m and an electron emitter is fixed at the top end of this cylinder. This guided electron beam passes through the sample of interest and scatters by the internal structure. Higher anode voltages are used to accelerate and attain maximum speed of electrons. As the resolving power is related to wavelength of electrons, the higher resolution is obtained by increasing the accelerating voltage. The typical voltage 200 KV are used for acceleration. The accelerated electrons focused on specimen to get the structural and microstructural information. Magnetic lenses are used to magnify the image and are recorded by CCD camera. This CCD detected image is displayed in real time.



Fig. 2.11. TEM system used for the work (FEI Tecnai G2-STWIN TEM).

The focusing of electrons by magnetic lenses on the sample is the foremost task in the image processing by TEM. These electron waves travelling towards the objective lens forms the diffraction pattern in the back focal plane and this pattern is described by the Fourier transform of the electron wave function at the object plane. In TEM the objective aperture position and size selects the rays or electron paths for image formation. Again, by doing the inverse Fourier transform of wave function at the back focal plane will give the wave function of electron at the image plane [16]. Thus, the relation between object and its diffraction is simply described by its Fourier transform. Selected area electron diffraction (SAED) is useful in determining the phase of few selected areas of the sample. The smaller area selection from the image is purely depends on the size of the aperture and its spherical aberration. HRTEM image cannot be formed by bright or dark-filed techniques. Fourier transforms plays a vital role in HRTEM analysis [17-19].

The bright-field (bf) and High-Resolution Transmission Electron Microscopic (HR-TEM) images of the films were recorded in a FEI Tecnai G2-STWIN TEM fitted with a

LaB6 electron gun. The typical magnification of TEM is in the range of 103 to 106. A small portion (approx. 1 mm ×1 mm size) of the film was scratched and placed on the grids to obtain the microscopic images. The photograph of the TEM used is shown in fig. 2.11. TEM can give complete information about the sample, like morphology, crystallographic information, composition and defect studies also.

2.5.4 Thin film thickness measurement

The BST thin films thickness was measured by using Stylus Profilometer and is shown in fig. 2.12.



Fig.2.12. Stylus Profilometer (XP-200, Ambios Technology, USA).

Surface Profilometer is a [20] technique used for determining the physical thickness of thin films. The requirement for measuring the thickness is the existence of a step, as shown in fig. 2.13. The profilometer works based on the contact of the tip on the surface of the film. A step or groove has to be created between substrate and thin film to measure the film thickness. The stylus will vertically displace at the step, and it will provide the thickness of the film, as shown in fig. 2.13(a). Fig. 2.13(b) shows the thickness profile of

the BST thin film. The masking of the substrate during film deposition over the required area is required to get proper steps rather than scratching the film after deposition. The error associated with the thickness measurement of the BST thin film is ± 10 nm.

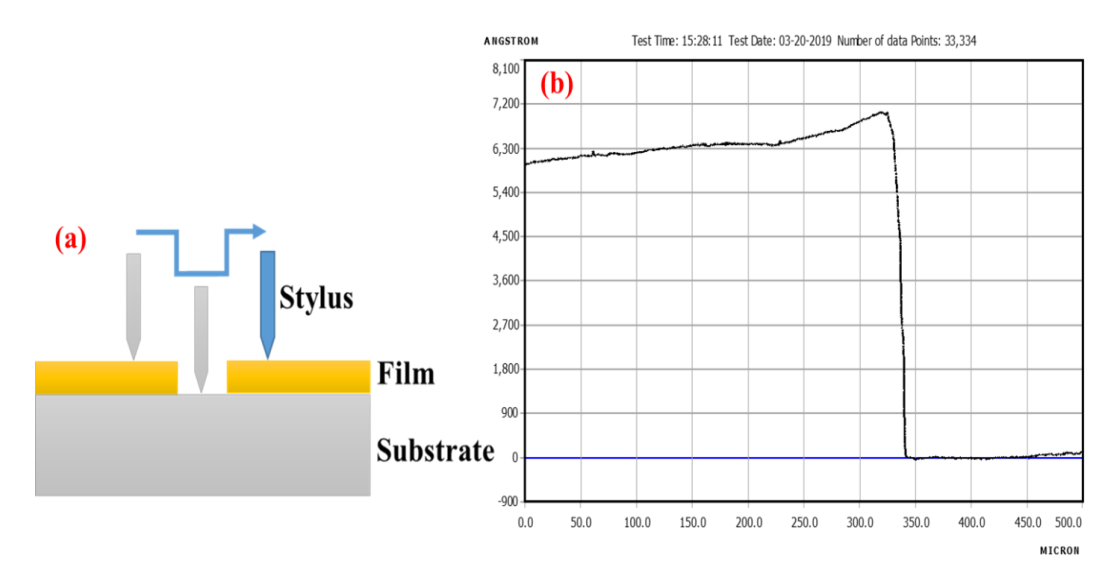


Fig. 2.13. (a) Illustration of stylus profilometer based measurement of film thickness (b)Thickness measurement result for BST thin films.

2.5.5 Band gap measurement from UV-Visible spectroscopy

In this work UV-VIS-NIR spectrophotometer was employed to characterize the optical properties like transmission and reflectance of the BST thin films shown in fig. 2.14. The optical properties of thin films play a key role in the quality assessment and selection of materials for optoelectronic devices. Optical transmittance spectra were recorded in a JASCO V-570 UV-VIS-NIR spectrophotometer with air as the reference. The spectral wavelengths are in the range of 190 - 2500 nm at the UV- NIR regions, respectively. The optical system consists of a double beam system with a single monochromatic source. A Tungsten halogen lamp is used as the source for wavelengths >350 nm and a deuterium lamp is used for wavelengths <350 nm.

The transmission mode was used to understand the optical properties of the films in the electromagnetic field. The transmission spectra of thin film studies show well-defined oscillations as seen in fig. 2.14(b). The oscillations arise due to the interference

between film and substrate which confirm the optical quality of the deposited thin films. The optical band gap is calculated by using the Tauc's relation [21-23]. The error associated with the bandgap calculation is 0.02 eV.

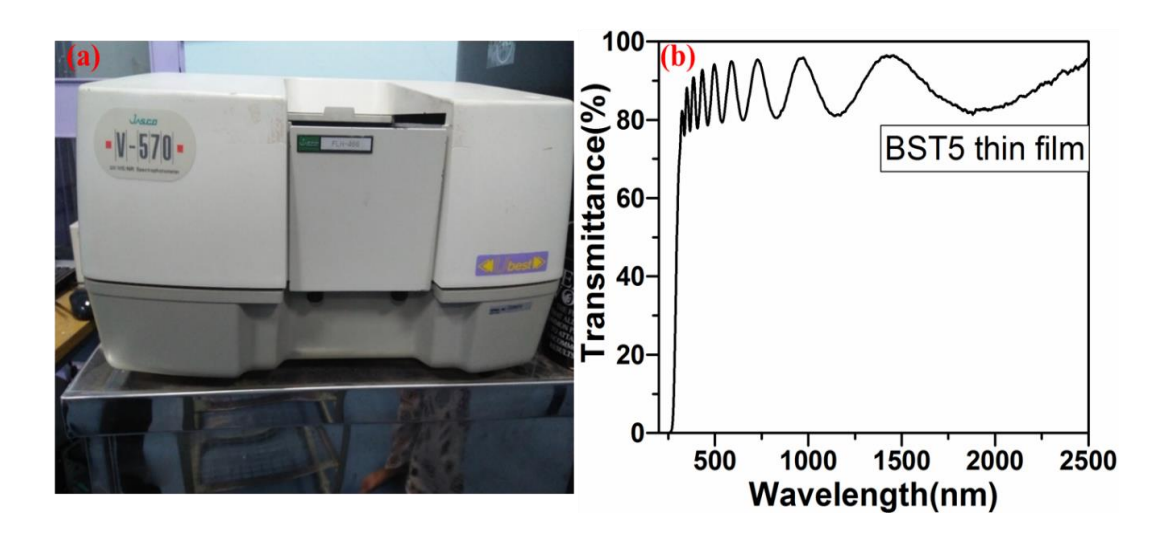


Fig. 2.14. (a) UV-VIS-NIR spectrophotometer (JASCO V-570). (b) Shows the transmission spectra of BST thin film.

2.5.6 Raman spectroscopy

Raman spectroscopy is a sensitive method for studying purity of phase and the chemical composition based on their vibrational modes. Raman spectroscopy can be utilized to reveal the molecular structure of inorganic and organic materials [24]. Raman spectra in solids arise due to inelastic scattering of the incident light caused by the band vibration known as phonons or vibrational modes of the medium. Raman spectra consist of many peaks related to several vibrational frequencies. In complex molecules, it is very difficult to identify those peaks as several peaks could merge to form complex bands. In the present study, Raman spectroscopic measurements was carried out using a Raman spectrometer (Witec Alpha 300) having Nd-YAG laser source with wavelength 532 nm. The power of the laser beam was adjusted in order to provide a high signal to noise ratio. Photograph of the Raman spectrophotometer is displayed in fig. 2.15.

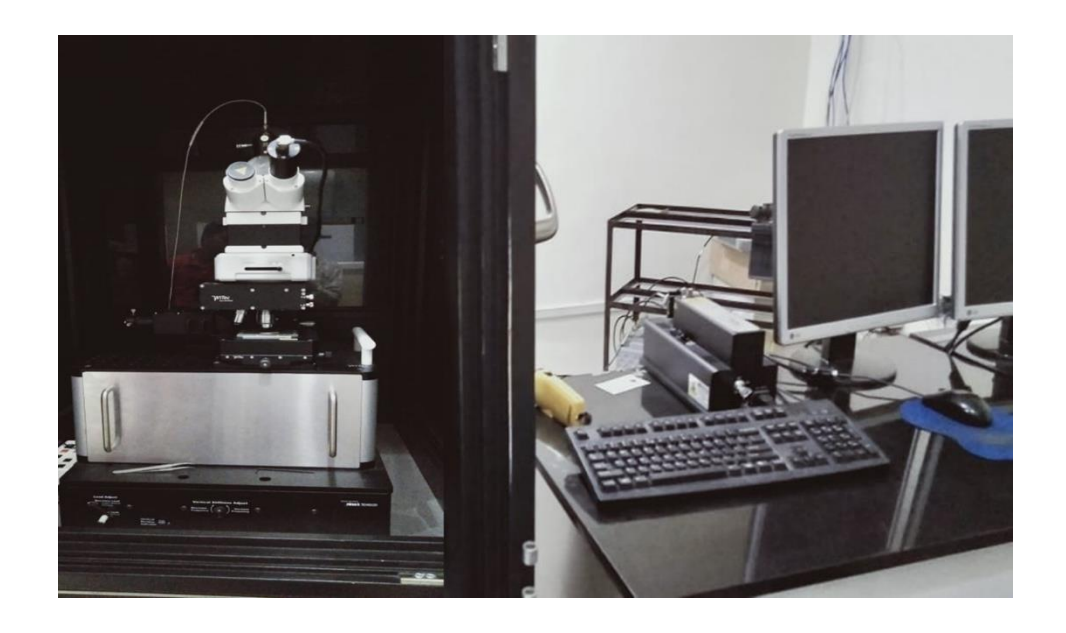


Fig. 2.15. Photograph of the Raman spectrophotometer (Witec Alpha 300).

2.6 Electrical measurements

2.6.1 Leakage current measurement

Leakage current is measured by a ferroelectric test module (TF1000 analyzer, aixACCT systems, Germany) shown in fig. 2.16. The system of ferroelectric test TF Analyzer 1000 is originated to give the facility for different measurements on ferroelectric materials to investigate its main electric characteristics. The ferroelectric test TF 1000 contains a function generator, an analog input board, and a wide bandwidth virtual ground amplifier with a driving unit. This system offers hysteresis measurements from 0.1 Hz to 1000 Hz bandwidth depending on the excitation voltage in virtual ground mode.

The leakage current measurement is performed by applying a special step-shaped voltage waveform to the sample and measuring the current response by the virtual ground amplifier.



Fig. 2.16. TF 1000 Analyzer of aixACCT GMBH, Germany for leakage current measurement.

The current reading is averaged in the region from 70% to 90% of the step time, giving a precise value for the leakage current. To minimize the ferroelectric contribution to the leakage current, the duration of each step was set to 5s, as shown in fig. 2.17, which was large enough to eliminate the effect of ferroelectric switching [25,26].

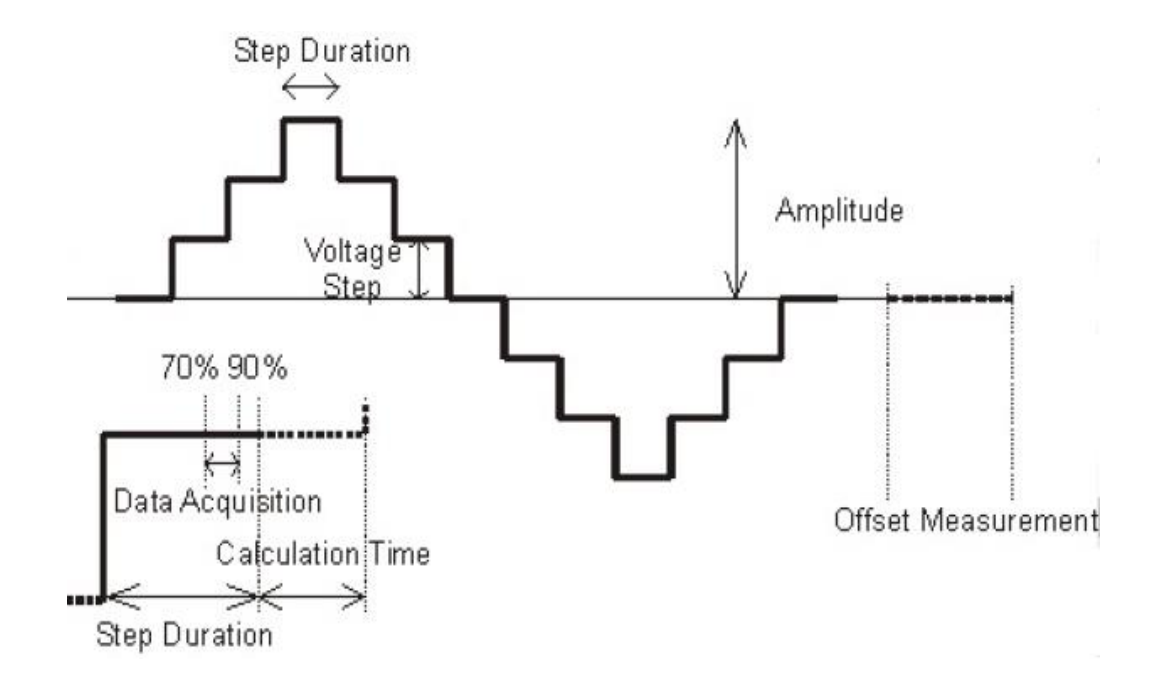


Fig. 2.17. Wave form for leakage current measurements [Hysteresis software version 2.4.0.0 user manual, aixACCT GMBH, Germany].

2.7 Device fabrication

The processing steps that were used fabricating test device structures in this work are 1. Cleaning the films, 2. Photoresist coating on films, 3. UV- Exposure, 4. Development, 5. Deposition of gold 6. Lift-off. All the process steps in the present work are performed in the cleanroom. The explanation of various processing steps are given below.

2.7.1 Test structure fabrication

The schematic of the process of the device fabrication on ferroelectric thin films is shown in fig. 2.18. Both the devices, Circular Patch Capacitor (CPC) and Interdigital Capacitor (IDC), are fabricated using the processes mentioned above. The bottom layer metal is deposited by RF sputtering. PLD is used to deposit ferroelectric layers, and a subsequent photolithography process is carried for patterning. After device structure

fabrication by the lift-off process, the test device structures are ready for the microwave characterization.

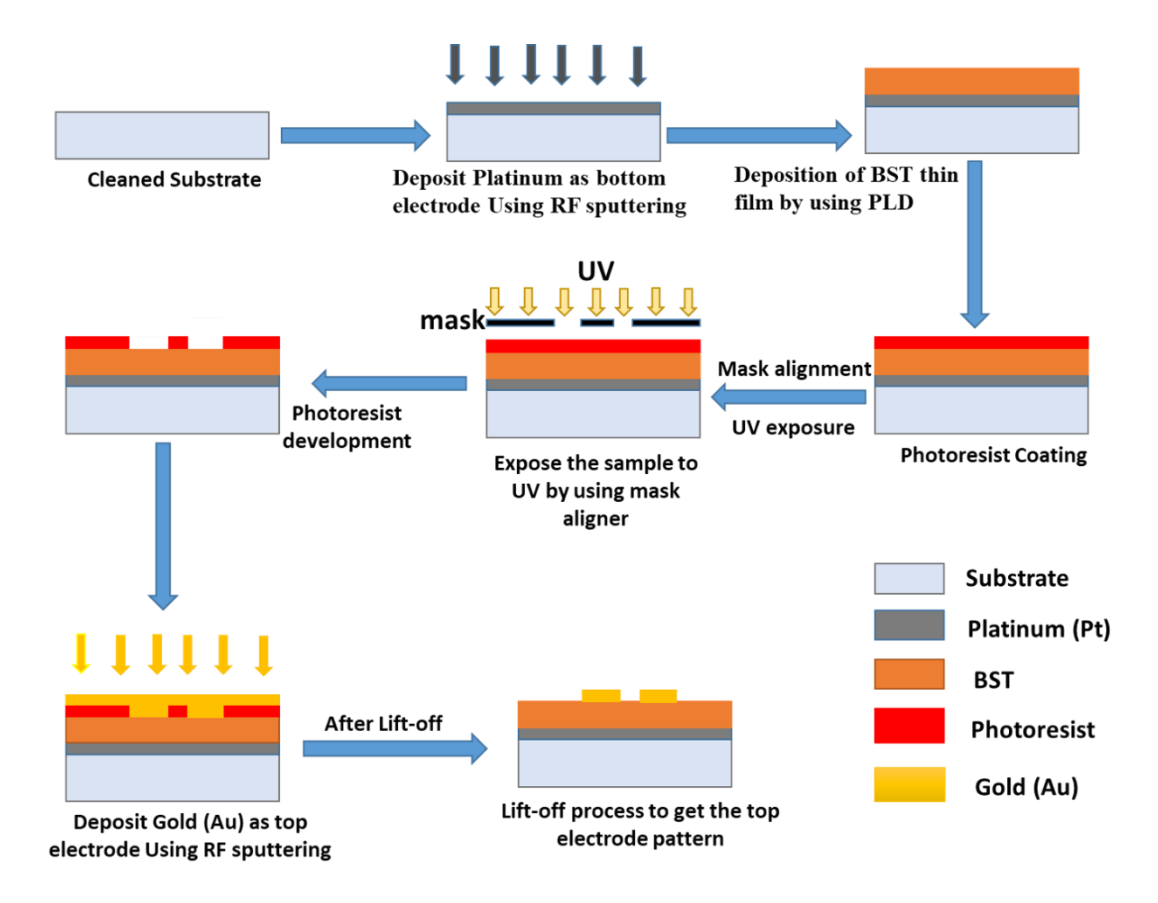


Fig. 2.18. Schematic of the device fabrication process used to fabricate test structures with ferroelectric thin films.

2.7.2 Circular Patch Capacitor (CPC) fabrication

The schematic (cross-section and top view) of the varactor design is as shown in fig. 2.19. It has the configuration Au/BST/Pt/Si. The circular patch capacitor (CPC) has been chosen to design the MIM (metal-insulator-metal) structure because of its simplicity in fabrication and characterization. It is used for the microwave dielectric property measurements of BST thin films. Parallel plate capacitors with the circular patch (CPC) electrodes were fabricated on platinized silicon substrates and gold (Au) as the top electrode. Lift-off process is used to pattern the top electrode consisting of a central circular patch surrounded by a concentric ground plane. The schematic cross-section and a

microphotograph of the CPC structure fabricated are shown in fig. 2.20. The capacitance C of this capacitor is measured between the inner circular patch and the outer circular ring using a GSG (Ground Signal Ground) 250-micron pitch probe and a probe station connected to the Agilent E8361C Vector Network Analyzer [27-29].

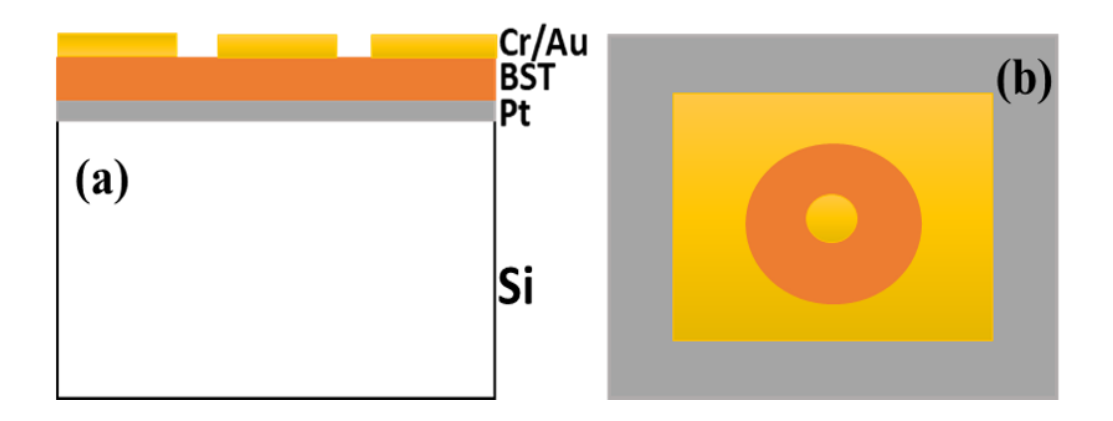


Fig. 2.19. (a) Schematic of the cross section of a Circular Patch Capacitor (CPC) test structure for microwave measurement of BST thin film on Pt/Si, top electrode: Cr-Au; (b) Top view of the CPC test structure: Centre (80μm) and outer circle (300μm).

In order to perform the microwave characterization, before starting the measurement, a standard substrate (CS -5) was used to perform the on-wafer calibration using the open, short and load structures present in the calibration substrate. Then, the scattering parameter of the one port device (S11) is measured for a specified frequency range, which has already been calibrated. The measured S11 is transformed into impedance for the test structure, ZT [31] by using the equation below.

$$Z_T = Z_0 \frac{1 + S_{11}}{1 - S_{11}} = R + JX$$
 (2.3)

where, Zo =50 Ohm is the characteristic impedance. The capacitance and loss tangent of the device under test (DUT) can be derived by using,

$$C = -\frac{1}{wX}$$
 $\tan \delta = \frac{R}{X}$

The microwave dielectric properties were calculated using the following equations.

$$\varepsilon_r = \frac{C \cdot d}{A \cdot \varepsilon_0} \tag{2.4}$$

Relative
$$Tunability = \frac{\varepsilon_{\text{max}} - \varepsilon_{\text{min}}}{\varepsilon_{\text{max}}}$$
 (or) $\frac{C_{\text{max}} - C_{\text{min}}}{C_{\text{max}}}$ (2.5)

Here, A and d are the capacitor area and film thickness respectively of the capacitor under test [30-32].

This structure that has been chosen as the bottom electrode does not need to be patterned, and the etching of BST is not required to expose the bottom electrode for probing. The outer circular patch establishes virtual grounding with the bottom electrode when the dc bias is applied as the area of the patch is large.

2.7.3 Interdigitated capacitor (IDC) fabrication

The IDC structure, which was deposited on BST thin films and used for microwave dielectric measurements, are shown in fig. 2.20. The bottom electrode is not compulsory for this structure, which requires a higher voltage and shows comparatively lower tunability. The tunability at microwave frequency is investigated using Agilent E8361C Network Analyzer and using a programmable voltage source. Voltage is applied to the IDC test structure through the coplanar waveguide probe. Measured S-parameters are used to calculate the capacitance of IDC using the following formula [33-36].

$$C = \frac{\text{Im}[S_{11}]}{\pi . f. Z_L \left(1 + \text{Re}[S_{11}]\right)^2 + \text{Im}[S_{11}]^2}$$
(2.6)

Where Z_L is the characteristic impedance and f is frequency.

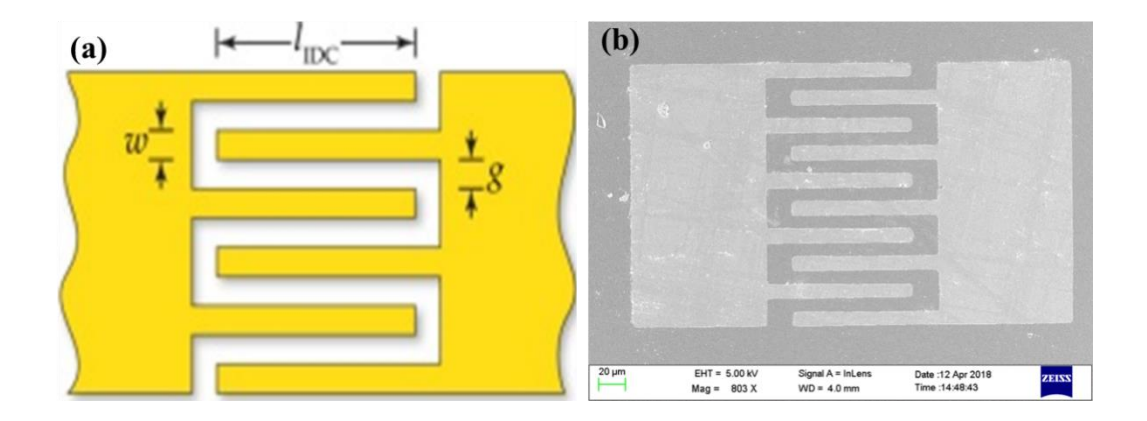


Fig. 2.20. (a) Schematic of IDC structure (b) FESEM image of fabricated IDC.

2.8 Microwave Dielectric property measurements of BST thin films

The S-Parameter measurements of fabricated CPC and IDC employing the BST films to be characterized were done using a probe station using an Agilent E8361C Vector Network Analyzer, as shown in fig. 2.21. The devices were probed by Ground-Signal-Ground (GSG) configuration through the 3.5 mm coaxial cables, and the DC bias voltages were applied using Bias Tees. The Bias Tee is used to protect the network analyzer from the high applied voltages. The DC bias was applied to the electrodes (radial stubs) and the bias lines using DC probes using a programmable voltage source. A full two-port calibration was performed using the GGB standard substrate (CS10) over 0.5 GHz to 4 GHz. Two types of two-port calibrations, namely i) SOLT and ii) TRL are used based on the device type and frequency of operation [37-38].

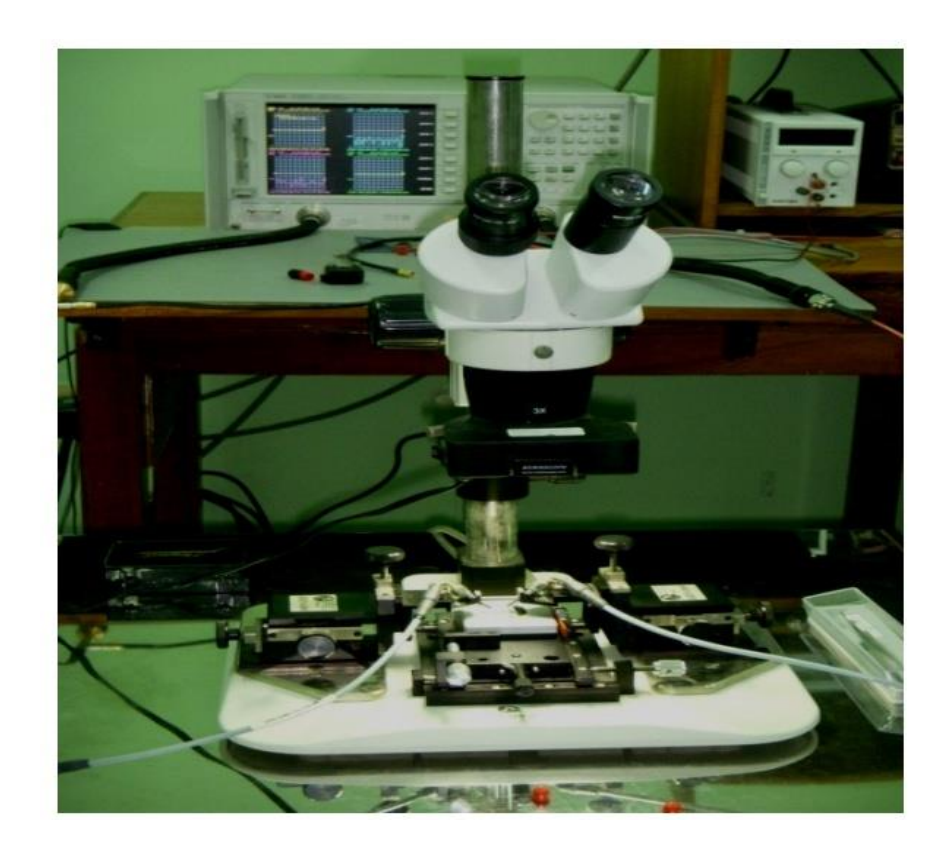


Fig. 2.21. On wafer probing measurement setup with probe station, VNA and DC voltage source.

2.8.1 SOLT Calibration

The short-open-load-thru is the most popular calibration method because of high precision co-axial standards (shorts-open-loads-thru) and they are easy to build. The SOLT calibration is based on a well-known standard because all the standards ae defined along the same plane of reference as shown in fig. 2.22b. This standard allows to find out the 12 types of errors as shown in fig. 2.22a. The accuracy of SOLT calibration significantly relies on the quality of the standard. Even a small deviation of standards can lead to large error. Furthermore, characterizing SOLT standards at frequencies beyond 20 GHz is laborious.

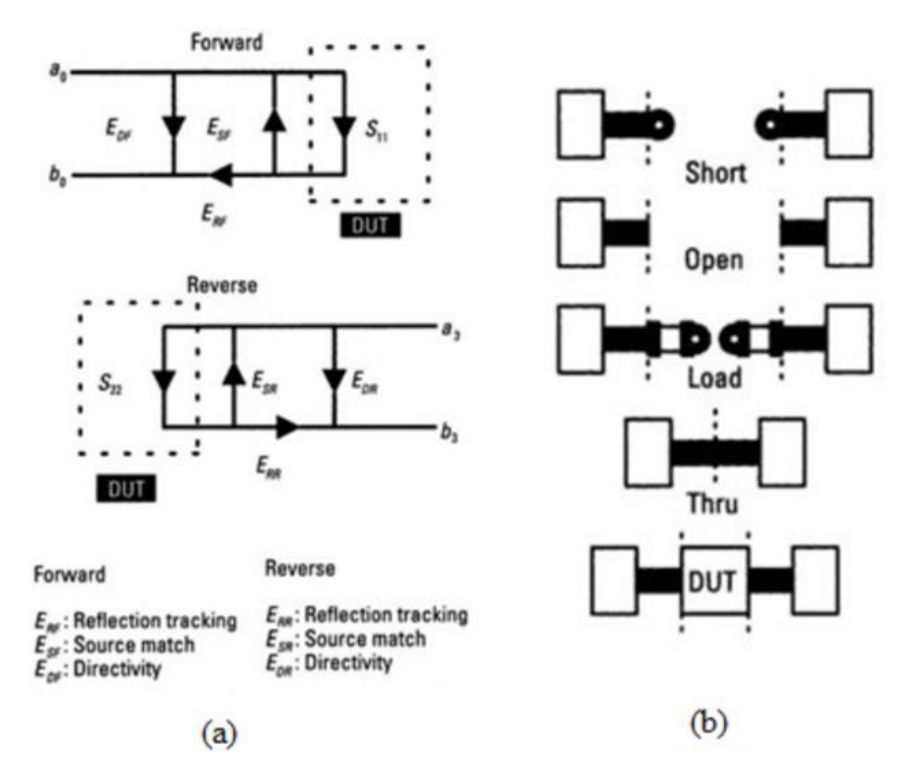


Fig.2.22. (a) One port vector calibration for port-1 and port-2 (b) Microstrip SOLT standards. Dotted line denotes the reference plane [39].

2.8.2 TRL Calibration

The Thru-Reflect-Line (TRL) calibration is based on the transmission line and simple to understand and easy to fabricate standards. A short length of the transmission line will act as a 'Thru' and the midpoint of thru will set the electrical reference plane shown in fig. 2.23. The 'Reflect' can be either an 'Open' or a 'Short'. The OPEN operates over a wider bandwidth than the Short. The characteristic impedance of the 'Line' will act as the reference impedance of the RF system.

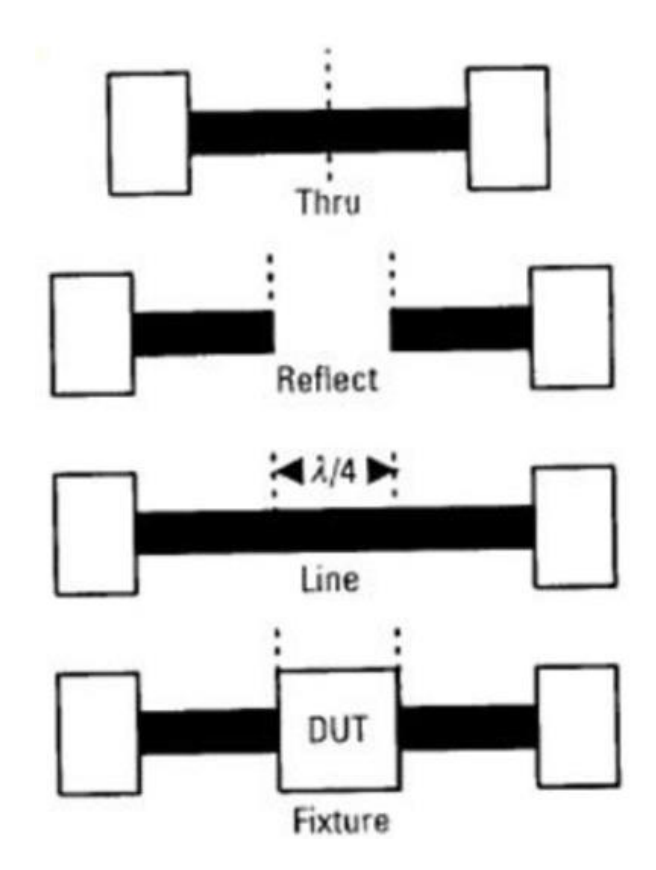


Fig. 2.23. Microstrip TRL standards. The electrical reference plane is at the center of the Thru [39].

References

- [1] C. Suryanarayana, Progress in Mater. Sci., 46, 1 (2001).
- [2] S-J. Kang "Sintering, densification, grain growth and microstructure" (Elsevier, Amesterdam) 2002.
- [3] Venkata Saravanan, Crystalline Barium Strontium Titanate thin films on Amorphous Fused Silica Substrates for Frequency Agile Microwave Devices, thesis (2009).
- [4] D. Agrawal, Journal of Materials Education, 19, 49 (1999).
- [5] Milton Ohring, *Materials Science of Thin Films: Deposition and Structure* (2/e), Academic Press, USA, 2002.
- [6] Katuri L Chopra, *Thin Film Phenomena*, Mc Graw-Hill Book Company, USA, 1969.
- [7] Robert Eason (Ed.), *Pulsed Laser Deposition of Thin Films: Applications-Led Growth of Functional Materials*, A John Wiley & Sons, Inc., Publication, New Jersey, 2007.
- [8] Douglas B. Chrisey, Graham K. Hubler, *Pulsed Laser Deposition of Thin Films*, Wiley, 1994.
- [9] Yang Leng (ed.), *Materials Characterization*, 2/e, Wiley-VCH Verlag GmbH & Co, Germany, 2008.
- [10] Peter E. J. Flewitt and Robert K. Wild, Physical Methods for Materials Characterization, CRC press, 2017.
- [11] D. Cullity, (Addison-Wesley, Reading, MA) 1956.
- [12] B.D. Cullity S.R. Stock, Elements of X-Ray Diffraction, Third Edition 2001.
- [13] K.D. Vernon-Parry, III-vs Review 13, 40 (2000).
- [14] Qingrui Yin Binghe Zhu Huarong Zeng, Microstructure, Property, and Processing of Functional Ceramics, page 314. Metallurgical Industry Press, 2003.
- [15] www.Edax.com
- [16] B fultz and J M Howe, "Transmission electron microscopy and diffractometry of materials" 3rd edition Springer Berlin Heidelberg New York (2008).
- [17] A Eades, Acta Microscopica 17, 101 (2008).
- [18] M D Graef, "Introduction to conventional transmission electron microscopy" Cambridge University Press, (2003).

- [19] S. Ramakanth, Magnetism and Laser Induced Crystallization of BaTiO3, and Ultrafast Demagnetization of Ni films, Thesis, 2017.
- [20] K. Creath, Morales A. In: Malacara D, editor. Contact and non-contact profilers in optical shop testing. 2nd ed. New York: Wiley; p. 691, 1992.
- [21] R. Swanepoel, J. Phys.E: Sci.Instrum, 16, 1214 (1983).
- [22] J.C. Tauc, F. Abeles., Optical properties of solids, North-Holland, Amsterdam, 1972.
- [23] H. Y. Tian, W.G. Luo, A.L. Ding, J. Choi, C. Lee, K. No, Thin Solid Films. 408, 200 -205 (2002).
- [24] C. N Banwell and E. M. McCash (Fundamental of Molecular Spectroscopy) Tata McGraw-Hill Pub. Com. Ltd, New Delhi, India (1995).
- [25] Ajeet Kumar, Structure-Property Correlations In Ultra-High Strain PLZT

 Ceramics Prepared Via High Energy Mechanical Milling (Ph.D Thesis), UoH,

 Hyderabad, 2016.
- [26] Hysteresis software version 2.4.0.0 user manual, aixACCT GmbH, Germany.
- [27] Spartak Gevorgian, Ferroelectrics in Microwave Devices, Circuits and Systems:

 Physics, Modeling, Fabrication and Measurements, Springer-Verlag, London, 2009
- [28] S. Govergian, A. Tangantsev and A. Vorobiev, *Tuneable Film Bulk Acoustic Wave Resonators*, Springer, 2013.
- [29] K. Sandeep, J. Pundareekam Goud and K. C. James Raju, Appl.Phys. Lett.111,012901 (2017).
- [30] K. Khamchane et al., J. Appl. Phys., 99,034103 (2006).
- [31] S. Sheng, P et al., J. Phys. D: Appl. Phys, 42, 01550.160 (2009).
- [32] K. Venkata Saravanan, K. Sudheendran, and K. C. James Raju, Electronic Materials
- [33] G.W. Farnell, I.A. Cermak, P. Silvester and S.K. Wong, IEEE Trans on Sonics and ultrasonics SU-17,188(1970).
- [34] H.N.AL. Shareef, D. Dimos, M.V. Raymond, R.W. Schwartz, C.H. Mueller, J. Electroceramics, 1:2,145(1997).
- [35] Zheyao Wang, Jianshe Liu, and Litian Liu, IEEE Transactions on Instrumentation and Measurement 55(1), 350–356 (2006).
- [36] Ki-Byoung Kim, Chul-Soon Park, *IEEE* transactions on ultrasonics, ferroelectrics, and frequency control, vol. 54, no. 11, November 2007.
- [37] http://www.ni.com/white-paper/11640/en/ dated 15.7.2018

- [38] Ananjan Basu, An Introduction to Microwave Measurements, CRC press, 2015.
- [39] Scott A. Wartenberg, RF measurements of die and packages, Artech House, 2002.

Chapter 3

In-situ crystallization of $Ba_{0.5}Sr_{0.5}TiO_3$ thin films

3.1 Introduction

One of the applications for which thin films of ferroelectrics in their paraelectric state are being researched is for the development of improved tunable devices in the microwave frequency range such as phase shifters, tunable filters, oscillators, delay lines etc. This constant focus on ferroelectric thin films is due to the peculiar combination of piezoelectric and dielectric properties [1-7] in them. The high dielectric permittivity with low loss at microwave frequencies make Ba_{0.5}Sr_{0.5}TiO₃ one of the highly studied ferroelectric material. In addition, it has Curie temperature (T_c) just below the room temperature. The high tuning speed of about ~10 ns and effective power handling properties of Barium Strontium Titanate films makes it ideal for varactors in tunable matching networks development [8-15].

The development of cost-effective and miniaturized lightweight communication devices (mobile phones, portable radar etc.) is hindered by the need for multi-bandwidth operation with reduced size. The solution to this problem is to use frequency tunable devices so that a single device can be made to operate at multiple frequencies. The progress in achieving this is creditable, and numerous reviews are available on the different aspects of tunable devices [16, 17].

As discussed earlier the following properties of Barium Strontium Titanate $(Ba_xSr_{1-x})TiO_3$ (BST) makes it to the top, as it got

- 1. Field dependent dielectric permittivity.
- 2. Low dielectric loss at microwave (MW) frequency range.
- 3. Ba/Sr ratio induced change in (a) Dielectric constant and (b) Curie temperature.

Furthermore, for the films the properties can alter with the deposition method, substrates being used and deposition parameters even within the deposition method. The structure related properties like grain size, structure, orientation and strain can alter with

the deposition parameters and hence the properties as mentioned above. There are reports regarding the variation of dielectric constant with thickness [18, 19]. Therefore, it becomes highly informative to investigate the properties of BST films at different deposition conditions for purposes of optimization and to correlate measurable properties with deposition conditions.

This chapter discusses the deposition of Barium Strontium Titanate (Ba $_{0.5}$ Sr $_{0.5}$ TiO $_3$) thin films by pulsed laser deposition. The substrate used was MgO (100) and the deposition is carried out at a constant temperature of 750°C and the working pressure is in the range of 1×10^{-1} - 1×10^{-4} mbar. The oxygen partial pressure is a crucial parameter controlling the formation of crystalline phase especially the crystallite size. The IDC structures were fabricated on the films to measure the dielectric properties at microwave frequencies. It is found that films deposited at low oxygen pressure and high laser fluence show maximum tunability of 16.5% at 1GHz frequency. Thus, this finding helps to explore the correlation between crystal structure and dielectric properties at microwave frequencies. Hence, in this chapter we discuss qualitatively how the conditions of 1×10^{-4} mbar pressure and 2 J/cm² fluence gives better tunability values.

3.2. Deposition conditions

The structure and lattice parameters of the substrate play a vital role in the growth of the desired material film. In this study, the lattice parameter of cubic MgO (100) is 4.216Å. The deposition parameters are the temperature of 750°C and the films were insitu annealed for 30 min after deposition in the presence of oxygen. The list of deposition conditions including oxygen working pressure and laser fluence are summarized in the table below.

Table 3.1. Nomenclature and deposition conditions of BST thin film samples deposited at constant temperature and variable pressure and laser fluence.

Ba _{0.5} Sr _{0.5} TiO ₃	Temperature	Base	Oxygen	No. of	Fluence
Thin films	(°C)/deposition	Pressure	working	pulses/	(J/cm^2)
Sample Codes	duration in hour	(mbar)	pressure	Time(hour)	
			(mbar)		
MBST5-001	750/1.30	5×10 ⁻⁶	1×10 ⁻¹	20000/1.06	1.4
MBST5-002	750/1.30	5×10 ⁻⁶	1×10 ⁻²	20000/1.06	1.4
MBST5-003	750/1.30	5×10 ⁻⁶	1×10 ⁻³	20000/1.06	1.4
MBST5-004	750/1.30	5×10 ⁻⁶	1×10 ⁻⁴	20000/1.06	1.4
MBST5-005	750/1.30	5×10 ⁻⁶	1×10 ⁻⁴	20000/1.06	2

3.3 Measurement of structural, microstructural and microwave dielectric properties

3.3.1. X-ray diffraction (XRD) Studies

X-ray diffraction of the films deposited at above conditions (MBST5-001, MBST5-002, MBST5-003, MBST5-004 and MBST5-005) are given in fig.3.1. The structure and space group of these films are confirmed after comparing with JCPDS file # 39-1395 and is identified as cubic with pm3m space group. The films are polycrystalline in nature with strong reflection along (111) plane.

The XRD patterns corresponding to the samples deposited at higher working pressure do not show any prominent peaks and are therefore partially crystalline in nature and 1×10^{-4} mbar deposited films are polycrystalline in nature, when the fluence increased to 2 J/cm² the film growth is observed along (111) direction. In the range of 1×10^{-3} - 1×10^{-4} mbar the films shown (110) oriented growth but for the films grown at laser fluence of 2 J/cm² the peak has shifted from (110) to (111) which is unique. It is clear that the direction of crystal growth has changed with increased fluence, and the possible cause of it is

explained below. The higher degree of crystallinity and crystallographic orientation at lower oxygen working pressure might be due to the stoichiometric transfer of target elements to the substrate as the collisions between the atomic species decreases at this lower oxygen working pressure and higher laser fluence. Also, this set of conditions must enhance the adatom mobility to enable them to occupy minimum energy positions of the growing crystal. This kind of energy minimization growth is observed in case of gold and aluminum. At lower vacuum adatoms can migrate in the surface for sufficiently larger distance to occupy lowest possible energy states and this leads to film having crystalline parameter close to cubic phase W. J. Kim [2]. Interestingly the (111) direction grown film have more tunability of 16.5% compared to the other films. Since (100) oriented films are known to be more tunable but is not observed here, the higher tunability in (111) films is an indication of better crystallinity in these films. Similar findings are also reported by Sung Eon Moon et al [24]. At lower oxygen working pressure stoichiometric transfer from target to substrate may take place, whereas this stoichiometric transfer reduces at higher working pressure due to the collision of oxygen ions in the plasma with the ions in transit. Hence, one can expect more tunability for these films (MBST5-005). From the observation of diffraction peaks in fig. 3.1, clearly evident that the compressive strain is relaxed with increase in oxygen working pressure. i.e., the lattice parameter and the unit cell volume is increased with decrease in oxygen working pressure and it is shown in fig. 3.1 (ii). Thus, the low oxygen working pressure and high laser fluence conditions are optimized to develop the unstrained films. Therefore, the unstrained films may be responsible for the higher tunability of the films.

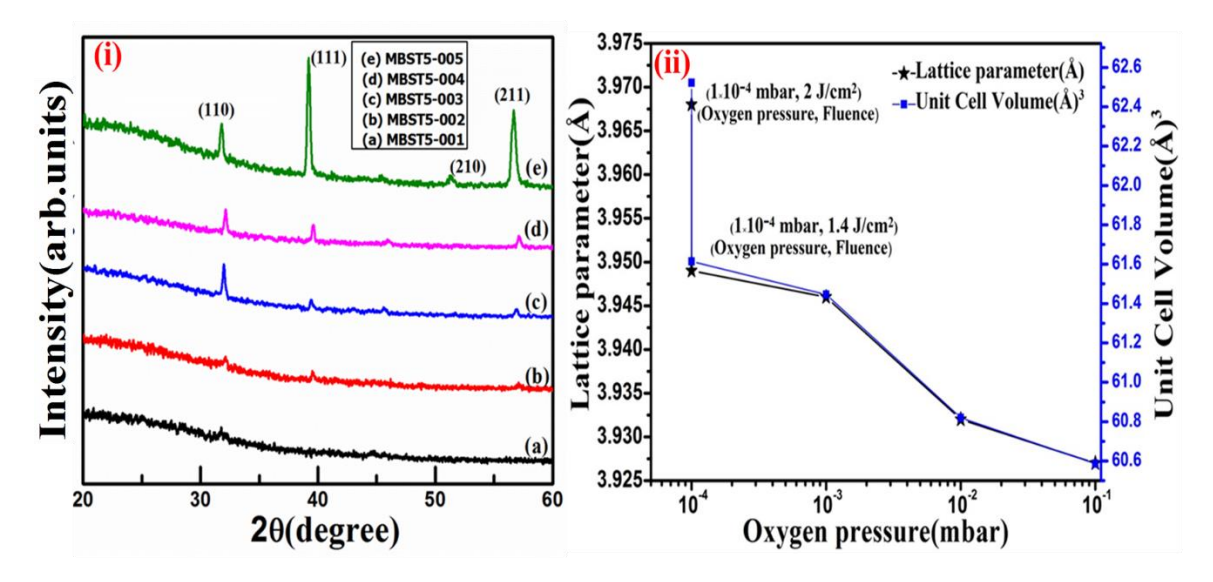


Fig.3.1. (i) XRD pattern of BST5 films on MgO substrates. (ii) depicts the variation of lattice parameter and unit cell volume with oxygen working pressure.

3.3.2 Calculation of Orientation Factor (OF)

The orientation factor and structure ratio values are obtained for MBST5-003, 004 and 005 films from the X-ray diffraction patterns whereas the other two films are only partially crystalline, therefore their orientation factor is difficult to calculate. The preferred orientation of each of the films were calculated, which also expresses the texture behavior of films [25-27]. The orientation factor is given by

$$F = \frac{(P - P_0)}{(1 - P_0)}$$
 here, $P = \frac{\sum I_{(abc)}}{\sum I_{(hkl)}}$ (3.1)

F is defined in connection to a reference plane (a b c) where a, b and c denote the Miller indices. The texture of films is defined as the ratio between the intensity of a family of planes oriented along a particular direction to that of sum of intensities of all reflections [25]. Where P_0 is the texture of the target material. In the present case we have the diffraction pattern in 20° - 60° range for both target and for the above deposited films.

Table 3.2: The values of average crystallite size, texture ratio, orientation factor and tunability (%) for BST5 films

Sample code	Average crystallite size(nm) ± 3nm	Texture Ratio (P/P ₀)	Orientation Factor(F)	Tunability (%)
MBST5-003	28.65	1.619	0.101	7.5
MBST5-004	30.15	1.866	0.122	8.8
MBST5-005	31.28	2.584	0.295	16.5

3.3.3 Microstructural studies by FESEM

The microstructures of MBST5-001 to MBST5-005 are given in fig.3.2. It is clearly evident that the oxygen working pressure has changed the microstructure of the films drastically. In particular the grain size is increased with the reduction of oxygen working pressure. The avg. grain size of films at a magnification of 200 nm are plotted for each film as histograms and inserted as insets in fig. 3.2. The avg. grain size of 70, 110, 140, 170 and 220 nm is obtained for MBST5-001, 002, 003, 004 and 005 films respectively. The films have uniform surface morphology. Thus, it is clear that these conditions are suitable for the nucleation process.

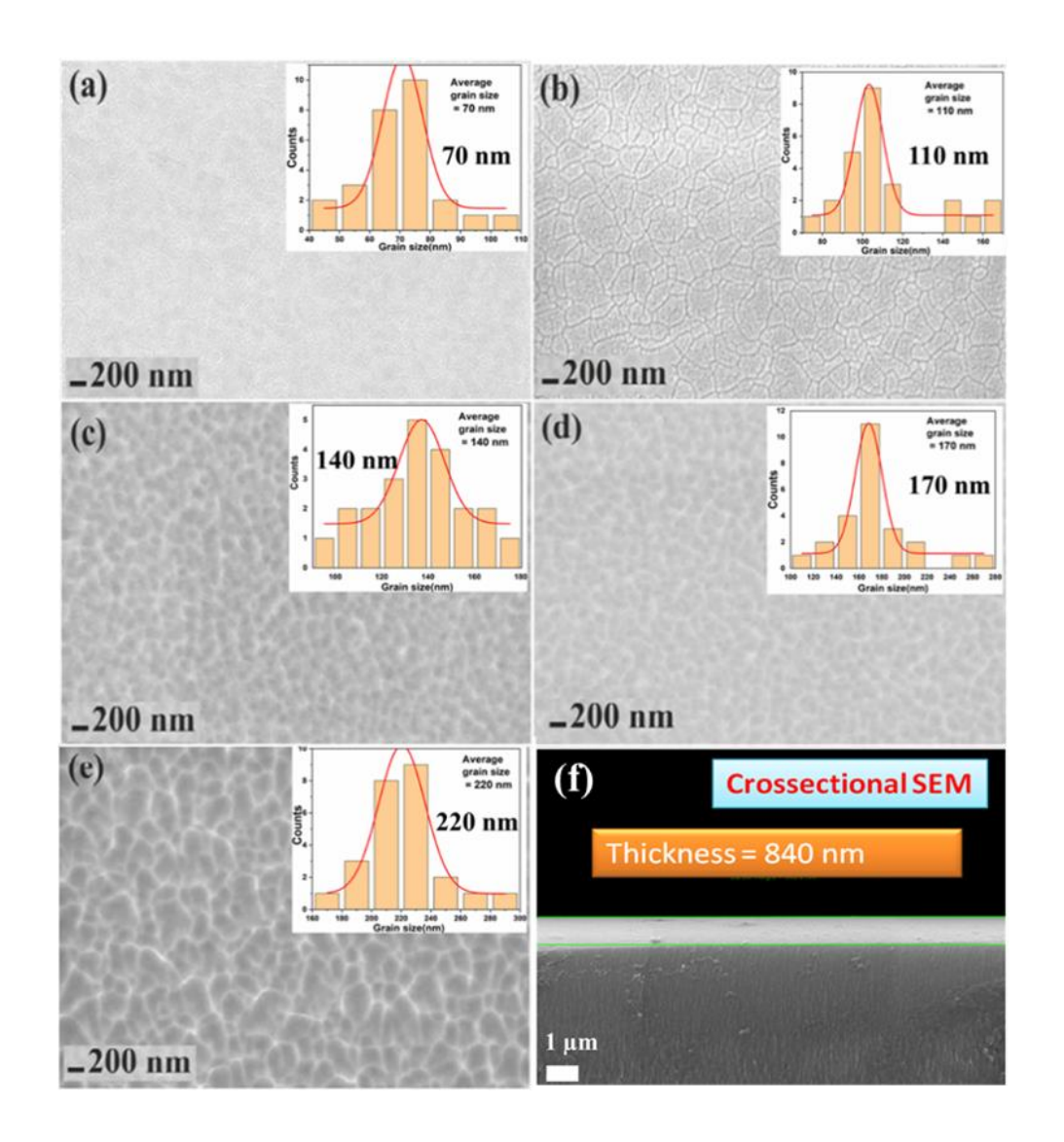


Fig.3.2: The FESEM images of BST5 films grown on MgO substrates (a) MBST5-001 (b) 002, (c) 003, (d) 004 and (e) 005 and (f) The cross-sectional image of MBST5-005.

3.4 Dielectric studies at microwave frequencies

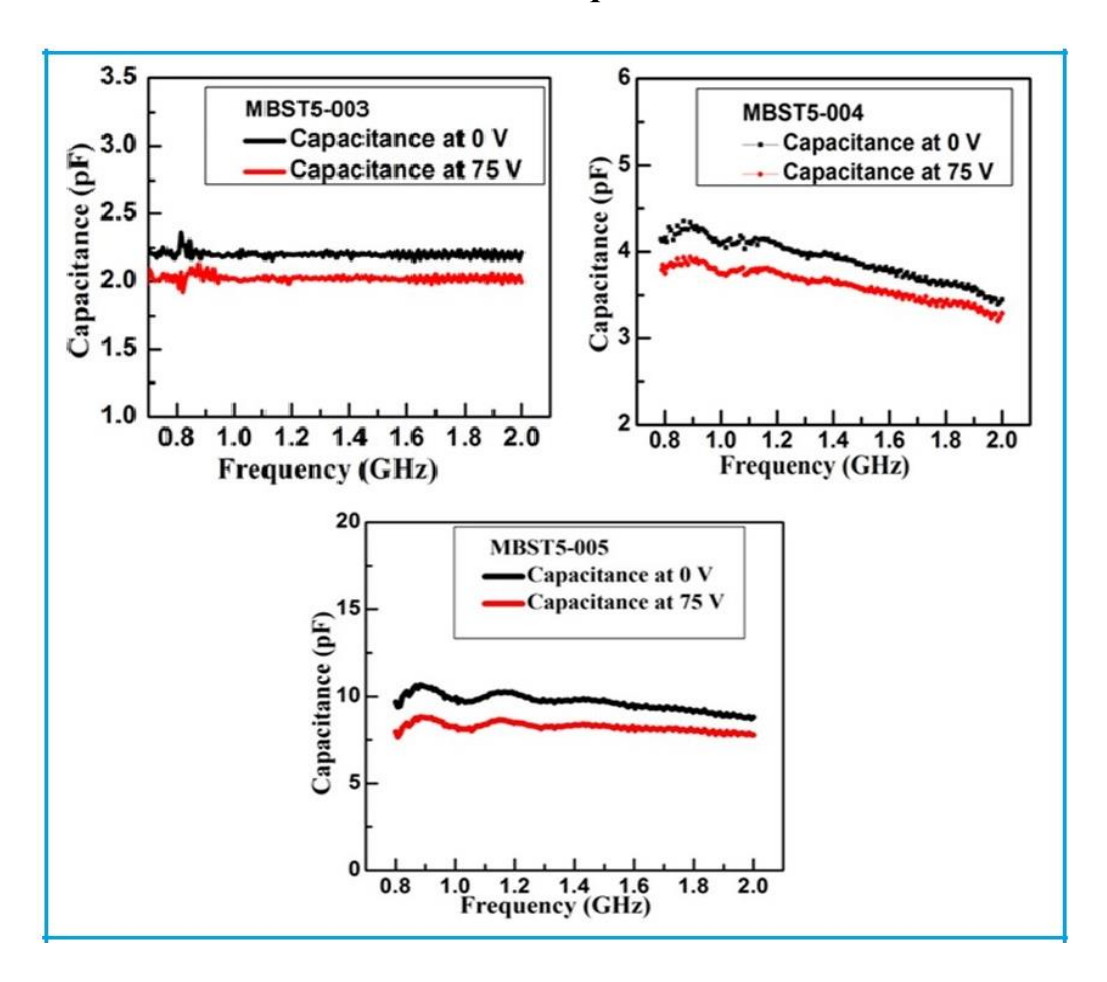


Fig.3.3 Variation of capacitance with frequency for MBST5-003, 004 and 005 films for IDC structures derived from data measured by VNA (vector network analyzer) at two different voltages namely 0 V and 75 V.

The high dielectric constant of films can change in the range 300-700 with the composition ratio, with lower losses at microwave frequencies. The paraelectric phase makes it more suitable for frequency agile devices [28]. The external DC bias dependent permittivity leads to tunability and is defined as

Tunability (%) =
$$\frac{C(0) - C(E)}{C(0)} \times 100$$

Where C(0) is dielectric capacitance at DC bias of zero and C(E) is the dielectric capacitance at DC bias of E. It quantifies the change in permittivity with bias field. For BST5 films, gold IDC structures were fabricated as top electrodes so that their tunability

can be measured by applying a DC electric field. The obtained S parameters were used in the calculation of capacitance using the following formula [29].

$$C = \frac{\text{Im}[S_{_{11}}]}{\pi . f. Z_{_L} (1 + \text{Re}[S_{_{11}}])^2 + \text{Im}[S_{_{11}}]^2}$$

Where f is frequency and Z_L is the characteristic impedance.

The capacitance and tunability of BST5 film on MgO substrate at bias voltage of 0V and 75V are given in fig. 3.3. The maximum tunability of 16.5% at 1GHz is obtained with an IDC structure with bias voltage of 75V for MBST5-005 film. (i.e. the film grown at low oxygen working pressure and high laser fluence of 2J/cm²). The partially crystalline films (MBST5-001 and 002) data is not given in table 3.2 and have shown the lowest tunability of 1-2% only. The vital point to note here is that the capacitance measured do not show frequency dispersion, which is more suitable for device applications. This is the consequence of the crystalline nature of the films and therefore one can claim that highly crystalline and crystallographic orientation acquired film may exhibit better dielectric tunability. U. Ellerkmann et al. [30, 31] studied the film thickness effect on dielectric properties. The findings suggest that there is interconnection between thickness and microwave dielectric properties. It is visible in Table 3.2 that increased crystallite size of the film leads to better tunability. The films MBST5-001 and MBST5-002 show lower tunability values and they are poorly crystalline also.

Eventhough MgO offers itself as a tensile substrate above certain critical thickness (50 nm), BST films are reported to show compressive misfit strain because of cumulative effect of thermal stress and misfit tensile stress relaxation as it is cooled after film deposition [32]. Seung Eon Moon [24] investigated the dielectric properties of epitaxially grown BST thin films and found a strong depence on orientation of substrate and film.

Hence the difference in capacitance observed in our case could be attributed to this anisotropic nature of BST thin film oriented in different directions. Our observation is aligned with W.J Kim [2] whose studies on tetragonally distorted BST thin films have shown a monotonic increase in dielectric properties and quality factor for films deposited in oxygen pressure of 50 mTorr to 1000 mTorr. At low oxygen pressure, substantial number of oxygen vacancies are present, and this increased number of vacancies leads to formation of defect dipole and ionic polarizability and hence the increased polarizability

3.5. Conclusions

In conclusion, BST5 thin films were deposited on (100) MgO substrates using well known PLD technique at different oxygen working pressures. The deposited films were found to vary from semi crystalline to completely crystalline states. With increasing oxygen partial pressure, the film's lattice parameter and unit cell volume decreased. The average crystallite size, texture ratio and orientation factor were extracted from XRD patterns. The tunability of the films with fabricated IDC test structures at microwave frequencies have been measured by applying dc voltage (0-75 V). The (111) directionoriented films showed a maximum of 16.5% of tunability at 1GHz frequency, while the films that were grown in other directions showed very low tunability values. The (111) oriented growth is obtained for the deposition conditions of 2 J/cm² laser fluence and lower oxygen working pressure of 1×10⁻⁴ mbar. Since T_c of BST5 is near to room temperature, the interface (substrate-film) will induce strain in the film at room temperature and this strain may play a crucial role in pseudo cubic phase formation. It is also concluded that the films with more tunability have higher orientation factor values. The films with higher orientation factor might have formed large number of aligned distorted octahedra and this can lead to enhanced macroscopic polarization in the films. Thus, the tunability of films are correlated with microstructural and structural aspects of the films.

References

- [1] C.V. Varanasi, K.D. Leedy, D.H. Tomich, G. Subramanyam, Thin Solid Films, 517, 2878–2881 (2009).
- [2] W. J. Kim, W. Chang, S. B. Qadri, J. M. Pond, S. W. Kirchoefer, D. B. Chrisey and J. Horwitz, Appl. Phys. Lett. 76 1185 (2000).
- [3] Kavita Verma, Seema Sharma, Dhananjay K Sharma, Raju Kumar, Radheshyam Rai, Adv. Mat. Lett. 3(1) 44-49 (2012).
- [4] Aftab Ahmed, Irene A. Goldthorpe, and Amir K. Khandan. Appl. Phys. Reviews. 2, 011302 (2015).
- [5] Q W Huang, L H Zhu, J Xu, P L Wang, H Gu, Y B Cheng J. Eur. Ceram. Soc. 25, 957–962 (2005).
- [6] S L Jiang, H B Zhang, R Z Lin, S B Liu, M D Liu, Integrated Ferroelectrics 70, 1-9 (2005).
- [7] S.S. Gevorgian, E.L. Kollgerg, IEEE Trans. Microwave Theory Tech. 49, 2117(2001).
- [8] W. Chang, L. Sengupta, J. Appl. Phys. 92, 3941(2002).
- [9] H.C. Graham, N.M Tallan, K.S. Mazdiyasni, J. Am. Ceram. Soc. 5, 548(1971).
- [10] Y Li, Y Qu, Mater Res Bull. 44(1) 82–85, (2009).
- [11] P. Bhattacharya, T. Komeda, K.H. Park, Y. Nishioka, Jpn. J. Appl. Phys. Part 1 32 4103, (1993).
- [12] Y.T. Kim, C.W. Lee, Jpn. J. Appl. Phys. Part 1 35 6153, (1996).
- [13] V. Craciun and R. K. Singh, Appl. Phys. Lett. 76, 1932 (2000).
- [14] K. Venkata Saravanan, K. Sudheendran, M Ghanshyam Krishna and K.C. James Raju, Ferroelectrics 356,158-165 (2007).
- [15] Ashok Kumar, Sriraj G. Manavalan, Surface and Coatings Technology, 198, 406 413 (2005).
- [16] M. K. Roy and Jerzy Richter, Proceedings of IEEE ISAF, 348 351(2006).
- [17] P Bao, T J Jackson, X Wang and M J Lancaster, J. Phys. D: Appl. Phys. 41, 063001(2008).
- [18] F. Zimmermann, M. Voigts, C. Weil, R. Jakoby, P. Wang, W. Menesklou,E. Ivers-Tiffee, Journal of the European Ceramic Society 21, 2019–2023 (2001).
- [19] Jong-YoonHa, Ji-WonChoi, Chong-YunKang, S.F. Karmanenko, DooJinChoi,

- Seok- JiYoon, Hyun-Jai Kim, J. Electroceram. 17,141–144 (2006).
- [20] N. Scarisoreanu, M. Filipescu, A. Ioachim, M.I. Toacsan, M.G. Banciu, L. Nedelcu, A. Dutu, M. Buda, H.V. Alexandru, M. Dinescu Applied Surface Science 253,8254–8257 (2007).
- [21] S.G. Lu, X.H. Zhu, C.L. Mak, K.H. Wong, H.L.W. Chan, C.L. Choy, Materials Chemistry and Physics 79, 164–168 (2003).
- [22] D. Roy and S. B. Krupanidhi, Appl. Phys. Lett. 62, 1056 (1993).
- [23] S. G. Lu, X. H. Zhu, C. L. Mak, K. H. Wong, H. L. W. Chan, and C. L. Choy, Appl. Phys.Lett. 82, 2877 (2003).
- [24] Sung Eon Moon, Eun-Kyoung Kim, Min-Hwan Kwak, Han-CheolRyu, Young-Tae Kim, Kwang-Yong Kang, Su-Jae Lee, and Won- Jeong Kim, Appl. Phys. Lett. 83, 2166 (2003).
- [25] Can Wang, B. L. Cheng, S.Y. Wang, H.B. Lu, Y.L. Zhou, Z.H. Chen, G.Z. Yang, Thin Solid Films 485, 82 89 (2005).
- [26] P. Padmini, T. R. Taylor, M. J. Lefevre, A. S. Nagra, R. A. York, and J. S. Speck, Appl. Phys. Lett. 75, 3186 (1999).
- [27] F. K. Lotgering, J. Inorg. Nucl. Chem. 9, 113 (1959).
- [28] E. Marsan, J. Gauthier, M. Chaker and K. Wu. IEEE NEWCAS Conf. 279-282 (2005).
- [29] Zheyao Wang, Jianshe Liu, and Litian Liu, IEEE Transactions on Instrumentation and Measurement 55(1), 350–356 (2006).
- [30] K. Venkata Saravanan, K. Sudheendran and K. C. James Raju, Electronic Mater. Lett.8, 571 (2012).
- [31] U. Ellerkmann, R. Liedtke, U. Boettger and R. Waser, Appl. Phys. Lett. 85, 4708 4710 (2004).
- [32] Z. G. Ban and S. P. Alpay, J. Appl. Phys. 91, 9288 (2002).

Chapter 4

In-situ crystallization of $Ba_{0.6}Sr_{0.4}TiO_3$ thin films

4.1. Introduction

BST material is under continuous exploration for the past 3 decades, and it is due to the application of this material in devices like electro-optic modulators, and tunable microwave devices [1-8]. BST is known for its high tunability, high dielectric constant and low loss in the microwave frequencies [9-16]. Several thin film depositions techniques are used for the development of BST thin films [16-21]. There are several reports which claim that the properties of these materials are affected by oxygen vacancies, grain size, and thickness of the film, etc. [22-25]. The RF sputtering and chemical vapour deposition (CVD) techniques are well known for developing large area thin films, as the large area films got good application potential. However, the films grown by RF sputtering have disadvantages due to its low deposition rate and poor oxygen stoichiometry while CVD uses hazardous organic gases as precursors. [26-31]. The pulsed laser deposition (PLD) technique is an alternative to overcome these difficulties as the laser target interaction transfers the same stoichiometry of target to the substrate [30-31]. However, the stoichiometric transfer of target elements to the substrate is only possible after the complete optimization of deposition parameters such as target substrate distance, laser fluence, oxygen working pressure, etc. [32-35]. The optimization of these parameters results in the development of strained films, which results in changes in morphology, optical and dielectric properties of the films [36-39].

In particular, Wang.et.al reported for BST that varying oxygen pressure resulted in a change in dielectric properties, and films that are deposited at 0.001 mbar oxygen pressure have smoother surfaces and lesser O₂ vacancy [40]. The main aim of this chapter is to study the influence of laser fluence on the optical and microwave dielectric properties of BST films. Here we considered the films of Ba_{0.6}Sr_{0.4}TiO₃ (BST6) compound for the

investigations and studied the effect of deposition parameters on microstructure, microwave dielectric and optical properties.

Thus, in this chapter, BST6 films were deposited by PLD at a constant working pressure and changed the laser fluence. XRD confirms the Phase of BST6 films and the strain is calculated using XRD patterns. The microstructure, strain and lattice parameter calculations were cross checked by HRTEM. The Tauc plot is used for the calculation of bandgap from transmission spectra in the range of 190-2500 nm. The films with good microstructural and optical properties used for the microwave dielectric property measurements by circular patch capacitor (CPC) method.

4.2 Experimental details

The PLD system has a KrF laser of wavelength 248 nm and a pulse duration of 20 ns with rep rate 5 Hz. The $Ba_{0.6}Sr_{0.4}TiO_3$ (BST6) films were deposited by this PLD system in a spherical chamber. The chamber is evacuated to a base pressure of 5×10^{-6} mbar and then filled with O_2 to a working pressure of 8×10^{-3} mbar in order to overcome the O_2 deficiency in the material. A 5 cm distance was maintained between the target and substrate. The total process of deposition and annealing was carried out at $700^{\circ}C$ temperature in the presence of O_2 for 1hour.

Table 4.1. The deposition conditions used for Ba_{0.6}Sr_{0.4}TiO₃ thin films on a fused silica substrate with an oxygen working pressure of 8×10⁻³ mbar. 10,000 pulses of laser shots are used with fluences as given in the table.

Ba _{0.6} Sr _{0.4} TiO ₃ thin film Sample Codes	Fluence (J/cm ²)
(a) BST6-01	1
(b) BST6-02	1.2
(c) BST6-03	1.4
(d) BST6-04	1.8
(e) BST6-05	2

The Laser fluence was optimized for good microstructure and optical properties on platinum-coated fused silica substrates. On the optimized films, Circular Patch Capacitors (CPC) were fabricated for microwave measurements using an on-wafer probe station with a Ground-Signal-Ground probe of 250 μ m pitch using an Agilent E8361C Vector Network Analyzer (VNA).

4.3 Results and discussions

4.3.1 X-Ray diffraction analysis

The XRD patterns of BST6 films deposited on fused silica substrates, at different laser fluence values are shown in fig. 4.1. By matching with the standard JCPDS card no (file # 34-0411), the phase formation is confirmed to the cubic phase with a space group of Pm3m. The XRD pattern in fig. 4.1 reveals the polycrystalline nature of the films.

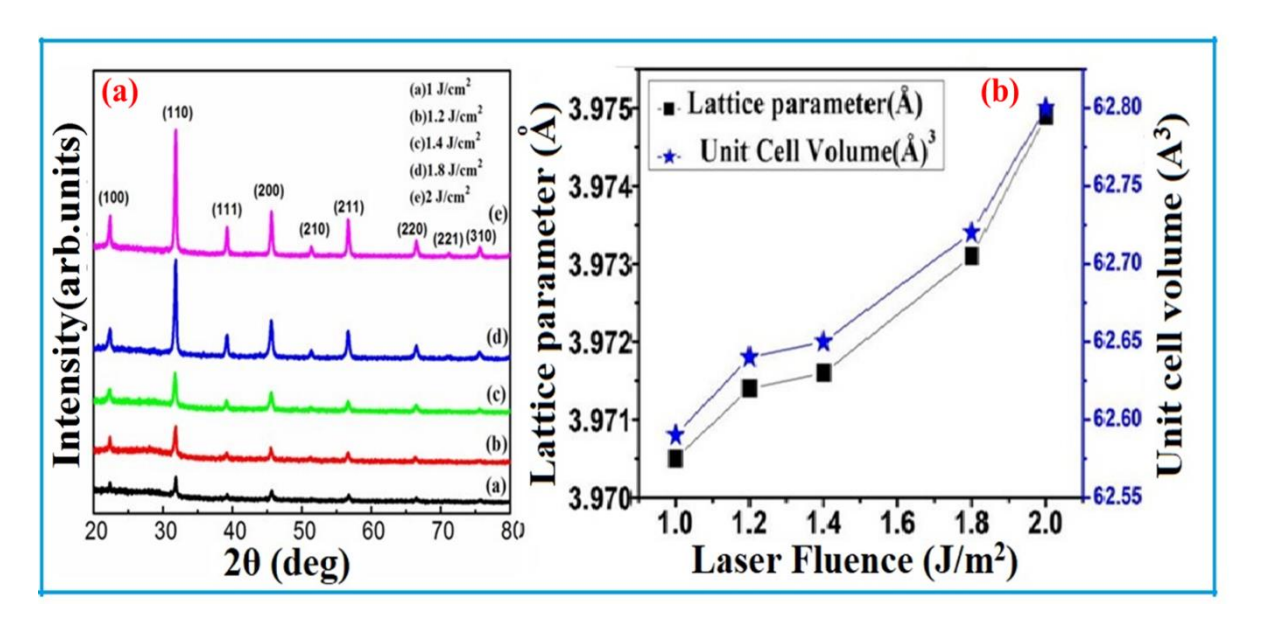


Fig.4.1. (a) XRD patterns and (b) lattice parameter and unit cell volume of the BST6 films deposited at various laser fluences.

From the XRD patterns, it is clear that as the laser fluence during deposition increases, the crystalline nature of films are increased. The minimum laser energy is required to create plasma of target material, which in turn deposited to the substrate to make thin films. The high energy guarantee excess energy transfer to the target material. With an increase in laser influence, more energy is incident on the target material. With more energy available on the target for the incident ions will result in the increase in kinetic energy of adatoms which will lead to better crystallization. Also, the films have developed a strain in them, which increases with laser fluence and it is evident from the shift of XRD to lower angles and hence increased lattice parameters and unit cell volume. With increasing laser fluence, the lattice parameter value reached a value corresponding to that of unstrained films.

The crystallite size, strain and diffracted angle are related by the following equation in Williamson-Hall method.

$$\beta\cos\theta = \frac{0.94\lambda}{D_{DH}} + 4\epsilon\sin\theta.$$

where D_{WH} = avg crystallite size, ϵ = strain in the crystal and β is the full width at half maxima. The crystallite size obtained by above equation by ploting $\beta\cos\theta$ vs $4\epsilon\sin\theta$ as shown in fig. 4.2.

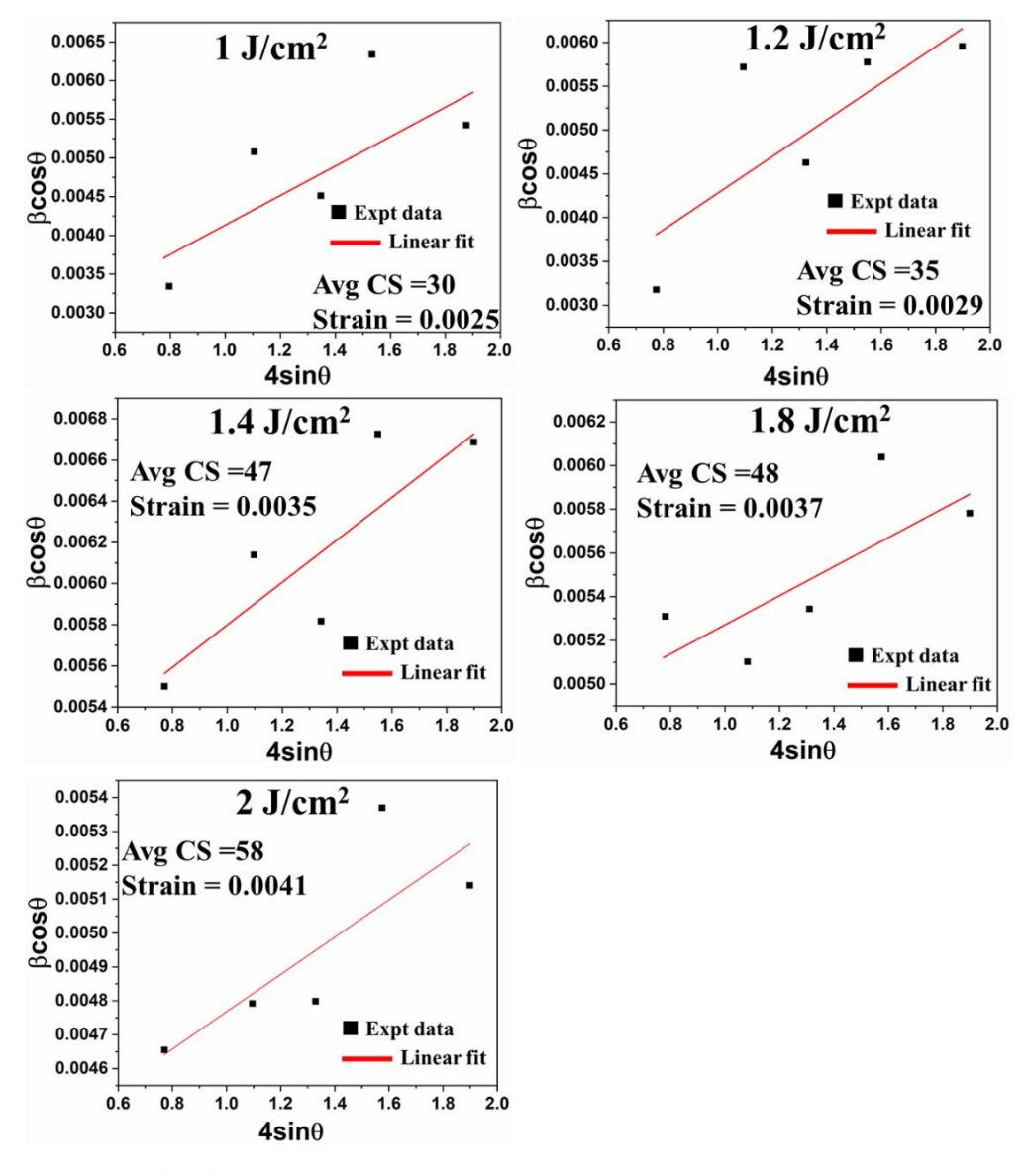


Fig. 4.2. W-H plots of BST6 films grown at different laser fluence.

The crystallite size is calculated by Williamson-Hall method as shown in fig. 4.2. The variation of crystallite size and strain with laser fluence are plotted in fig. 4.3. The crystallite size has increased from 30 nm 59 nm as the laser fluence increases from 1 J/cm² to 2 J/cm².

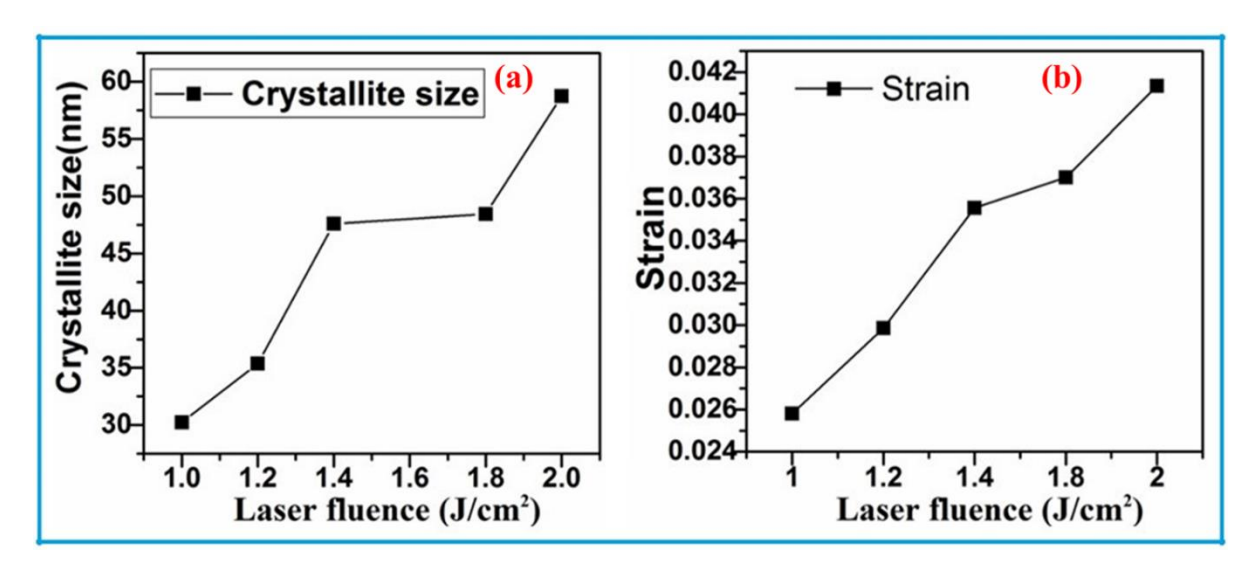


Fig. 4.3. (a) Crystallite size and (b) Strain of BST6 films deposited at different laser fluence.

4.3.2 Microstructure

The morphological and microstructural studies of these films were carried out by FESEM. As the laser fluence used for deposition increases, the grain formation can be observed. From fig. 4.4, it is clear that up to 1.2 J/cm² fluence, the surface morphology is smooth, and as the fluence reached to 1.8 J/cm², it shows the grain formation and finally, for the fluence of 2 J/cm², it clearly shows the agglomerated cluster formation. Thus, the high fluence condition during deposition is supporting the grain growth and nucleation process. The grain size is obtained 70 nm and 130 nm for the films deposited at 1.8 J/cm² and 2 J/cm² laser fluence as shown in fig. 4.4.

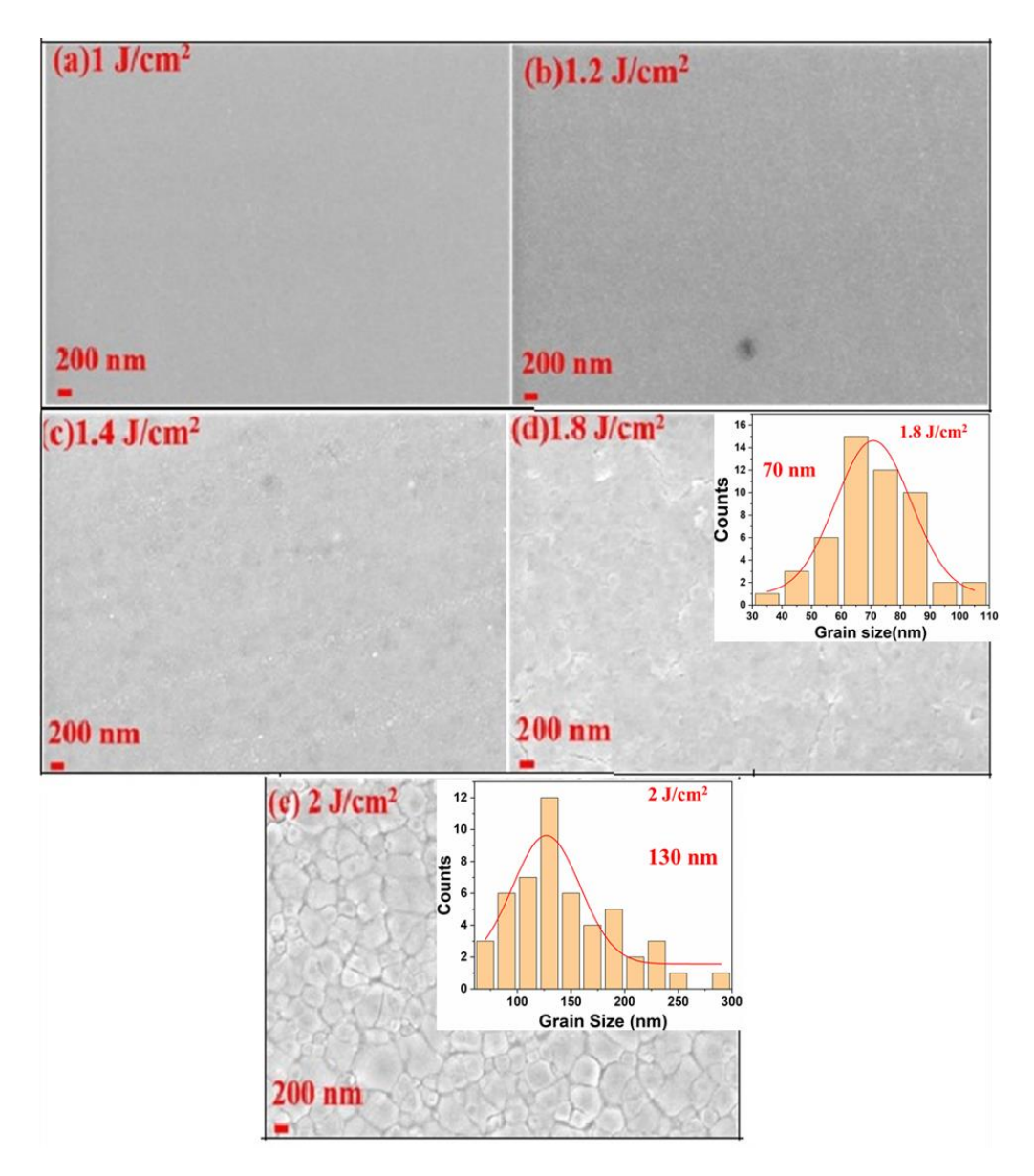


Fig.4.4. Microstructure of different BST6 films grown at different laser fluence.

4.3.3 Structural studies by Transmission Electron Microscopy (TEM)

The TEM studies are also carried out for these films. In fig. 4.5(a)(i-v), the bright-field images of samples are shown. It is clearly seen that the crystallite size increased as the fluence of laser during deposition increases, however the crystallites are of irregular shape. Fig 4.5(b) shows the HRTEM images of the films. For all samples(i-v), the HRTEM images gives (110) oriented crystallites and the d spacing is in the range of 2.72- 2.79Å.

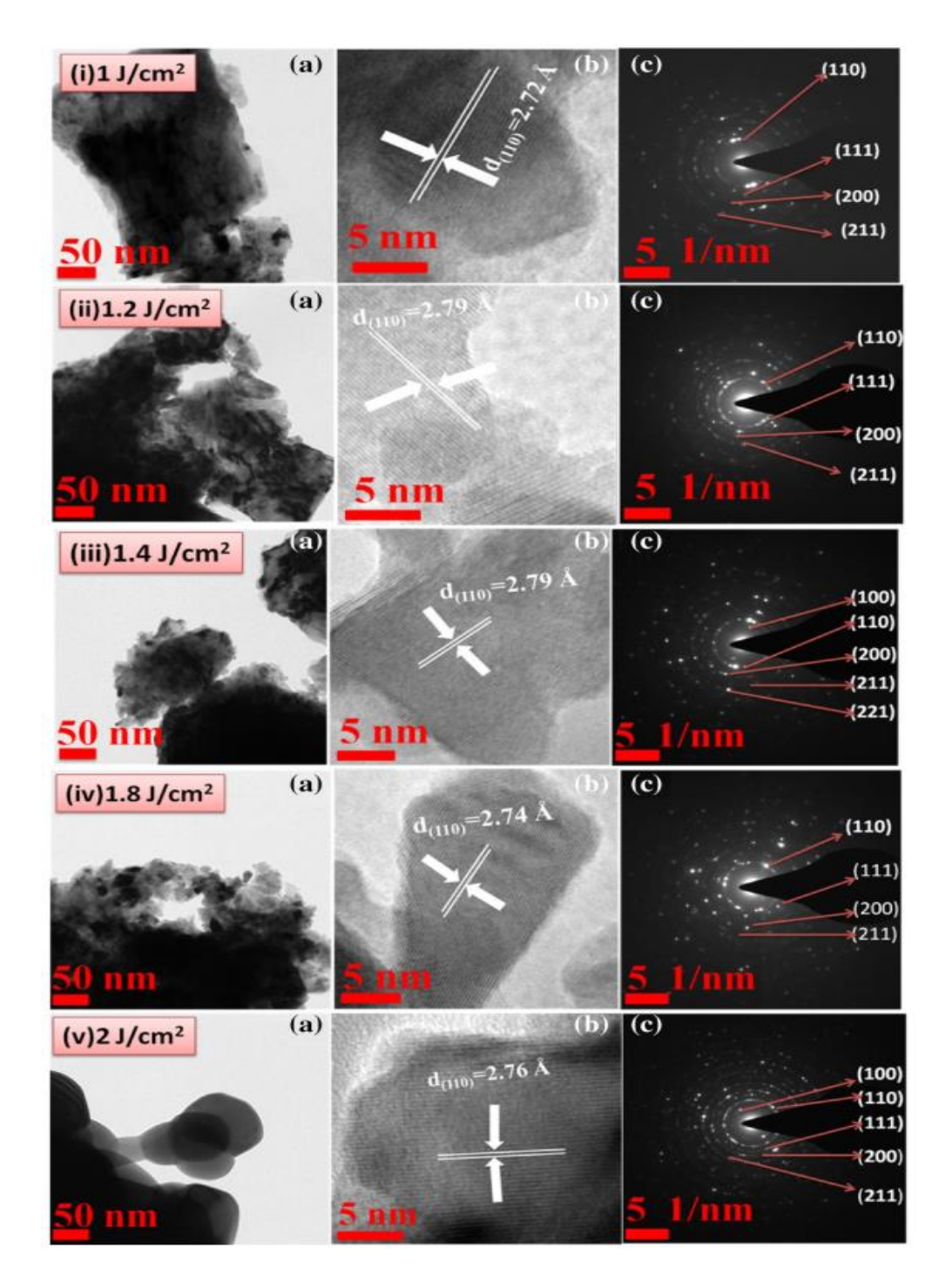


Fig. 4.5. TEM images of BST6 films grown at different laser fluence(a) Bright field images (b) HRTEM and (c) Selected area diffraction (SAED) patterns.

The crystallite size obtained from W-H plots are compared with that obtained using the TEM data. The crystallite values obtained by both methods are given in Table 4.2 and they are in close agreement.

Table 4.2. Crystallite size from XRD and from WH plot along with strain for films deposited at different laser fluence.

Sample code	Laser Fluence (J/cm ²)	Crystallite size XRD (nm) ± TEM (nm) 3 nm ±3 nm		Strain ×10 ⁻²
(a) BST6-01	1	30	31	2.58
(b) BST6-02	1.2	35	34	2.98
(c) BST6-03	1.4	47	44	3.55
(d) BST6-04	1.8	48	48	3.7
(e) BST6-05	2	58	57	4.13

4.4 Optical properties

4.4.1 UV-Visible Spectroscopy - Bandgap studies

The transmission spectra of films deposited at various fluence are shown in fig. 4.6(a). Figure 4.6(b) shows the Tuac's plots for all these films. The band gap values of these films have decreased from 4.45 eV -3.62 eV with increase in laser fluence during deposition and fringes have changed drastically in the transmission spectra.

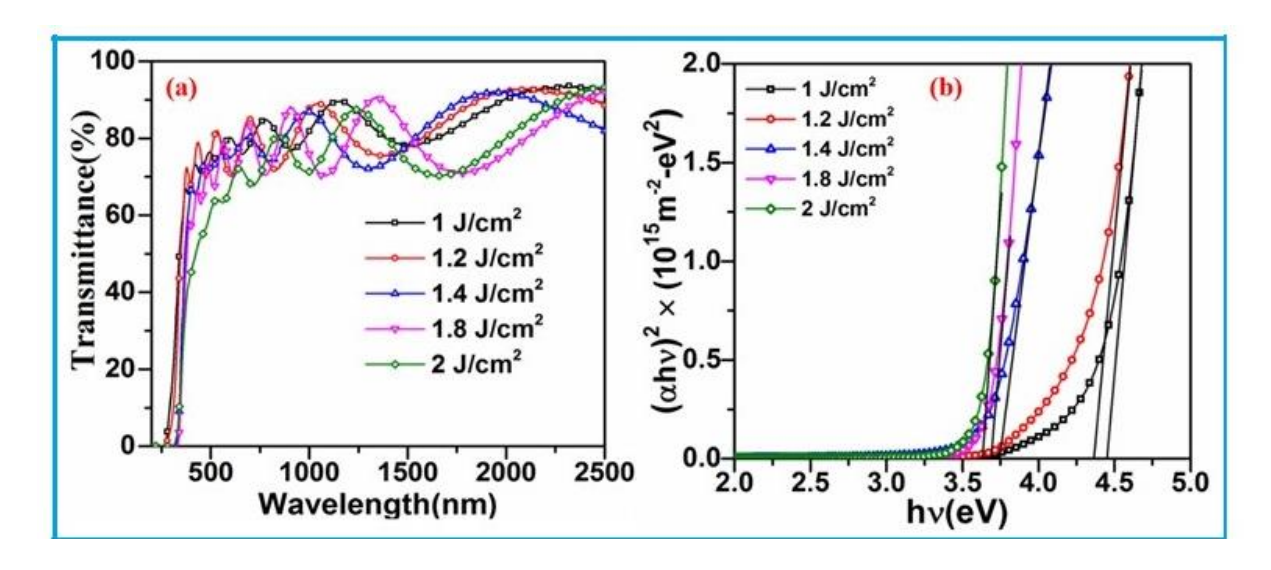


Fig.4.6. (a) Optical transmission and (b) $(\alpha hv)^2$ vs hv plots of BST6 films.

The Tauc's relation is,

$$\alpha h \vartheta = A(h\vartheta - E_g)^{\frac{1}{2}} \tag{4.1}$$

where $h\vartheta$ is the photon energy, A is a constant, ϑ is the frequency and α is absorption coefficient. Thus,

$$\alpha = \frac{\ln(\frac{1}{T})}{d} \tag{4.2}$$

where T is transmittance and d is the thickness of film.

The $h\theta Vs (\alpha h\theta)^2$ is plotted in fig. 4.6(b) and fitted by eq (4.1)

The variation of bandgap energy with laser fluence is given in fig. 4.7. The high fluence grown films are crystalline and they shows sharp rise in absorption, whereas the partially crystalline films do not. The partially crystalline films have states in-between band gap and hence there is no sharp rise.

The band gap of the films decreases from 4.45eV to 3.62 eV as the laser fluence increases from 1 J/cm² to 2 J/cm² respectively [46-50]. Thus, the bandgap values indirectly hints that the crystallization is taking place. For insulator band gap is more than 3 eV and here films deposited at lower laser fluence are not fully crystalized and may have amorphous regions. This is due to the states associated with numerous non stoichiometric phases in the partially crystalline films.

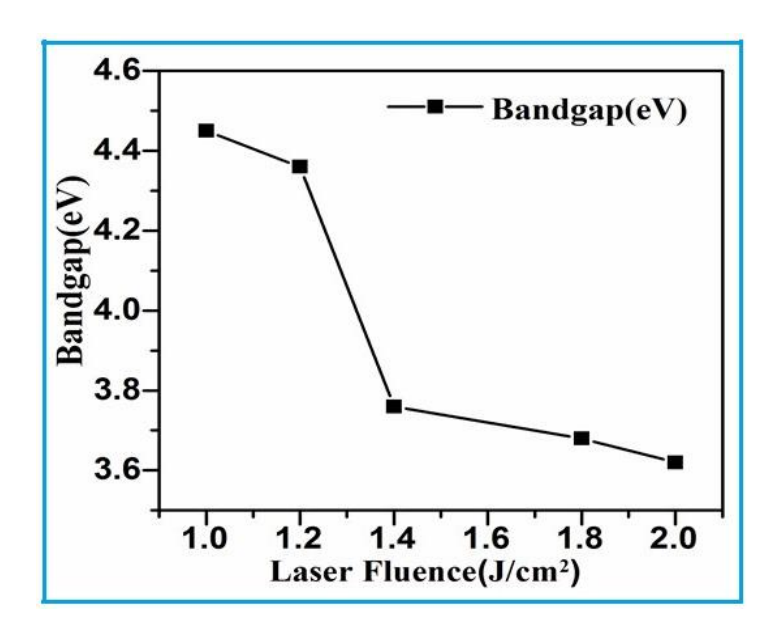


Fig. 4.7. Optical band gap values of BST6 films deposited at different laser fluence.

4.4.2 Raman spectroscopy

Raman spectroscopy is one of the best techniques to study ceramic materials even in their thin films. It comes under the inelastic scattering process. The vibrational modes will be Raman active when they affect the polarizability of the dipoles. The Raman spectra of the above films are taken at ambient and are given in fig. 4.8.

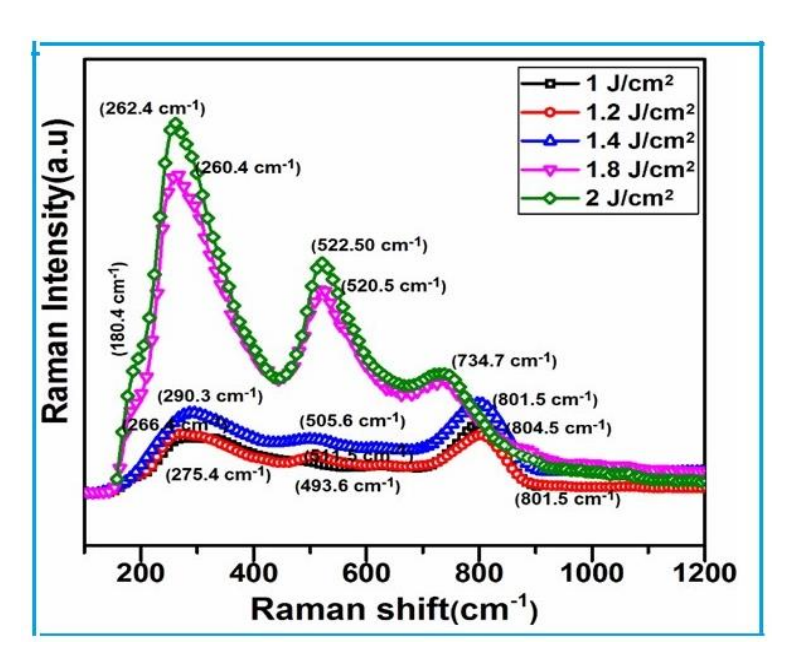


Fig.4.8. Raman spectrum of BST6 films showing improving crystallinity with increase in laser fluence during deposition.

The substrates used for film deposition are Raman inactive and amorphous. Therefore, they do not give any additional contribution to the Raman modes of BST6 films [51,52]. Phonon modes are observed at 260-300, 480-575 and 800-805 cm⁻¹ for the films deposited with 1, 1.2 & 1.4 J/cm² laser fluence, while the films that are deposited with laser fluence of 1.8 & 2 J/cm² have dominant modes.

The increase in Raman mode intensity with an increase in laser fluence during deposition, clearly supports that crystallization of films happens at higher laser fluence. It is also observed that the Raman modes shift to lower frequency and it indicates the presence of increased strain in the films with increasing laser fluence [53-57].

4.5 Microwave Dielectric properties

The BST6 ferroelectric thin films are deposited on the Pt-coated fused silica by pulsed laser deposition at the optimized conditions. A Circular Patch Capacitor (CPC) is fabricated on the films for microwave dielectric property measurements. The Au top electrode of 150 nm thickness was patterned by photolithography [58-61]. An Agilent E8361C Network Analyzer with a probe station is used to carry out the microwave measurements on the fabricated CPC structure. The dc bias applied is changed, and the S-parameters are measured over 0.5 - 4 GHz frequency range. The variation of capacitance and dielectric constant from V=0 to V=35 V volts are shown in fig. 4.9 (b)-(c).

The measured results showed that the films deposited at optimized condition of 2 J/cm² laser fluence exhibit good Microwave Dielectric properties. The thickness of the metal electrode of the CPC has been low compared to that of skin depth, and therefore the loss values obtained are higher which a combination of both material and metallic losses.

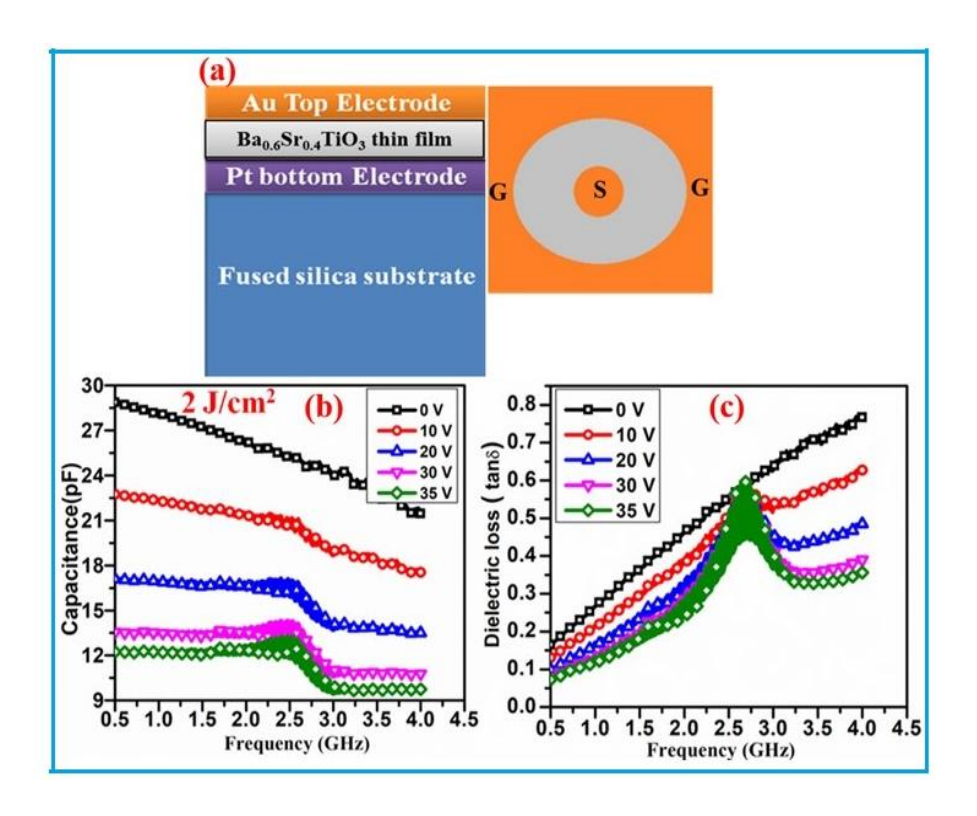


Fig.4.9. Microwave Dielectric properties of 2 J/cm² laser fluence grown BST6 thin films.
(a) Schematic top and cross-sectional view of CPC test structure made on BST6 films. (b and c) Capacitance and dielectric loss (tanδ) variation with frequency.

In the figure plotted above resonance peaks starts appearing once a DC bias is applied across the capacitor. This resonance peak is due to the dc field induced piezoelectric effect caused by electrostriction in BST6. With increase in dc bias field the intensity of the resonance also increases. In case of the paraelectric BST6, unlike a piezoelectric material, there is no spontaneous polarization ($P_S = 0$) and the polarization is due to the applied dc field. Since the DC field applied is much stronger than the AC field, the polarization due to DC field is much greater than that of AC field i.e. $P_{DC} \gg P_{AC}$ and the strain and induced polarization relation [62] is given as below:

$$S = QP_{DC}^2 + (2QP_{DC}) P_{AC}$$
, Q is electrostriction coefficient.

This relation is characterized by the DC bias dependent effective piezoelectric coefficient $g_{DC}=2QP_{DC}$. Hence the polarized paraelectric BST6 when under the AC field acts like a

piezoelectric material converting the electrical oscillations into acoustic wave. Hence paraelectric thin films like BST6 can be used in designing acoustic wave resonators and filters which have additional functionality of being switchable and tunable [62].

Tunability is the characteristic property that gives a change in dielectric constant when the voltage is applied across the film.

It is defined as below

Tunability (%) =
$$\frac{C(0) - C(E)}{C(0)} \times 100$$
 (4.3)

where C(E) and C(0) are the dielectric capacitance values at non-zero and zero dc electric bias field respectively. By the above formula, a tunability of 56% is obtained at 1 GHz frequency for the BST6 films deposited at 2 J/cm² fluence. The dielectric constant of film is around 284 at 1 GHz frequency.

4.6 Conclusions

In summary, a systematic study on the effect of laser fluence (or) laser energy density on structural, microstructural and optical properties of polycrystalline BST6 ferroelectric thin films deposited by Pulsed Laser on fused silica substrates are systematically studied. In particular, the microstructural studies have confirmed that the films are composed of nano-sized grains. The structural and Raman studies indicate that the films are of single phase in nature and also the strain values obtained by Williamson–Hall method are in agreement for XRD and TEM studies. The optical properties like bandgap is calculated by the Tauc plot using transmission spectra and it is well correlated with structural and micro structural properties of BST6 thin films. The microwave tunability of well crystallized BST6 thin films is found to be 56% at 1 GHz.

References:

- [1] M. Haghzadeh, C. Armiento, A. Akyurtlu, IEEE Transactions on Microwave Theory and Techniques. 65, 2030-2042 (2017).
- [2] K. Nadaud, C. Borderon, R. Renaud, A. Ghalem, A. Crunteanu, L. Huitema, F. Dumas-Bouchiat, P. Marchet, C. Champeaux, H.W. Gundel, Applied Physics Letters. 109, 262902 (2016).
- [3] L. Zhang, P. Wu, Y. Li, Z.Y. Cheng, J.C. Brewer Composites Part B: Engineering. 56, 284-289 (2014).
- [4] H. Dong, J. Jian, H. Li, D. Jin, J. Chen, J. Cheng, Journal of Alloys and Compounds. 725 54-59 (2017).
- [5] T. Teranishi, R. Kanemoto, H. Hayashi, A. Kishimoto, Journal of the American Ceramic Society. 100, 1037-1043 (2017).
- [6] X. Ma, S. Li, Y. He, T. Liu, Y. Xu, Journal of Alloys and Compounds. 739, 755-763 (2018).
- [7] P. Wu, M. Zhang, H. Wang, H. Tang, P. Bass, L. Zhang, AIP Advances. 7, 075210 (2017).
- [8] P. Wu, L. Zhang, X. Shan, Materials Letters. 159, 72 (2015).
- [9] P.C. Joshi, M.W. Cole, Applied Physics Letters. 77, 289-291(2000).
- [10] Hongzhe Wang, Yaoxuan Dong, Zengmei Wang, Journal of Alloys and Compounds.745,651-658 (2018).
- [11] Xi Ning, Shuming Chen, Jinying Zhang, Hui Huang, and Lei Wang, Applied Physics Letters 107, 052905 (2015).
- [12] G. Subramanyam, M.W. Cole, N.X. Sun, T.S. Kalkur, N.M. Sbrockey, G.S. Tompa, X. Guo, C. Chen, S.P. Alpay, G.A. Rossetti, K. Dayal, L.Q. Chen, D.G. Schlom, J. Appl.Phys. 114, 191301 (2013).
- [13] J. Liao, X. Wei, Z. Xu, X. Wei, P. Wang, Materials Chemistry and Physics. 135, 1030-1035 (2012).
- [14] S.Z. Wang, J.X. Liao, Y.M. Hu, F. Gong, Z.Q. Xu, M.Q. Wu, Materials Chemistry and Physics. 193, 50-56 (2017).
- [15] M.W. Cole, W.D. Nothwang, C. Hubbard, E. Ngo, M. Ervin, Journal of Applied Physics.93, 9218-9225 (2003).
- [16] Y. Gim, T. Hudson, Y. Fan, C. Kwon, A.T. Findikoglu, B.J. Gibbons, B. H. Park,Q.X. Jia, Appl. Phys. Lett. 77, 1200–1202 (2000).

- [17] Y. Lin, Jang-Sik Lee, H. Wang, Y. Li, S.R. Foltyn, Q.X. Jia, G.E. Collis, A.K. Burrell, T.M. Mcclesdey, Appl. Phys. Lett. 85, 5007–5009 (2004).
- [18] T.S. Kim, C.H. Kim, M.H. Oh, J. Appl. Phys. 75, 7998–8003(1994).
- [19] S. Regnery, Y. Ding, P. Ehrhart, C.L. Jia, K. Szot, R. Thomas, R. Waser,J. Appl. Phys. 98, 084904 (2005).
- [20] H. Chang, C. Gao, I. Takeuchi, Y. Yoo, J. Wang, P.G. Schultz, X. D. Xiang, R.P. Sharma, M. Downes, T. Venkatesan, Appl. Phys. Lett. 72, 2185–2187(1998).
- [21] K. Terai, M. Lippmaa, P. Ahmet, T. Chikyow, T. FuJii, H. Koinuma, M. Kawasaki Appl.Phys. Lett. 80, 4437–4439 (2002).
- [22] X. B. Yan, Y. C. Li, J. H. Zhao, Y. Li, G. Bai and S. Q. Zhu, Appl. Phys. Lett. 108, 033108 (2016).
- [23] Wei Luo, Xiangyu Chen, Junwei Fan, Yunxiang Hu, Zhiping Zheng, Qiuyun Fu, Ceramics International 42, 17229–17236 (2016).
- [24] Qing Xu, Di Zhan, Duan-Ping Huang, Han-Xing Liu, Wen Chen, Feng Zhang, Materials Research Bulletin 70, 99–105 (2015).
- [25] Yanlong Bian, Jiwei Zhai, J Sol-Gel Sci Technol 69, 40–46 (2014).
- [26] M. Beres, K.M. Yu, J. Syzdek, S.S. Mao, Thin Solid Films 608, 50–56 (2016).
- [27] J. Greer, A Wiley-Interscience Publication, New Jersey, 2007.
- [28] Kari Remes, Kimmo Leppänen, and Tapio Fabritius, Optics Express.26, 1219 (2018).
- [29] Michael Saliba, Juan-Pablo Correa-Baena, Michael Gratzel, Anders Hagfeldt, and Antonio Abate, *Angewandte Chemie International Edition*, 27, 2554 -2569 (2018).
- [30] Marco Bonelli, Claudio Cestari and Antonio Miotello, Meas. Sci. Technol. 10, N27–N30 (1999).
- [31] Martando Rath, E. Varadarajan, V. Natarajan, M.S. Ramachandra Rao, Ceram Int. 44, 8749-8755 (2018).
- [32] Daniele Preziosi, Anke Sander, Agnes Barthelemy, and Manuel Bibes, AIP Advances 7, 015210 (2017).
- [33] Jorgen Schou, M. Gansukh, Rebecca B. Ettlinger, Andrea Gazzaniga, Maarja Grossberg, Marit Kauk-Kuusik, Stela Canulescu, Applied Physics A 124,78 (2018).
- [34] M. Beres, K.M. Yu, J. Syzdek, S.S. Mao, Materials Chemistry and Physics. 205, 90-96 (2018).

- [35] Hiroaki Nishikawa, Tsukasa Hasegawa, Akiko Miyake, Yuichiro Tashiro, Satoshi Komasa, Yoshiya Hashimoto, APSUSC. 427, 458-463 (2018).
- [35] Hiroaki Nishikawa, Tsukasa Hasegawa, Akiko Miyake, Yuichiro Tashiro, Satoshi Komasa, Yoshiya Hashimoto, APSUSC. 427, 458-463 (2018).
- [36] L. Radhapiyari, A.R. James, O.P. Thakur, Chandra Prakash, Materials Science and Engineering B 117, 5–9 (2005).
- [37] Hongwei Chen, Chuanren Yang, Chunlin Fu, Li Zhao, Zhiqiang Gao, Applied Surface Science 252, 4171–4177(2006).
- [38] Hongwei Chen, Chuanren Yang, Chunlin Fu, Jihua Zhang, Jiaxuan Liao, Liye Hu, Applied Surface Science 254, 3175–3179 (2008).
- [39] Kitae Eom, Taemin Kim, Jiwon Seo, Jaedu Choi, and Jaichan Lee, Journal of Nanoscience and Nanotechnology14, 8762–8765 (2014).
- [40] Can Wang, B.L. Cheng, S.Y. Wang, H.B. Lu, Y.L. Zhou, Z.H. Chen, G.Z. Yang, Thin Solid Films. 485, 82–89 (2005).
- [41] Z. G. Ban and S. P. Alpay, J. Appl. Phys. 91, 9288 (2002).
- [42] Won -Jae Lee, Ho-Gi Kim, and Soon-Gil Yoon, Journal of Applied Physics 80, 5891 (1996).
- [43] Zahra Saroukhani, Nemat Tahmasebi, Seyed Mohammad Mahdavi And Ali Nemati Bull.Mater. Sci., Vol. 38, No. 6, pp. 1645–1650 (2015).
- [44] S. Ramakanth, S. Hamad, S.V. Rao, K.C. James Raju, AIP Adv. 5, 057139 (2015).
- [45] M. Cernea, B.S. Vasile, A. Boni, A. Iuga, Journal of Alloys and Compounds 587, 553–559 (2014).
- [46] J.P. Goud, A. Joseph, S. Ramakanth, K.L. Naidu, K.C.J. Raju, AIP Conf. Proc., AIP Publishing, p. 020293 (2016).
- [47] K. Lakshun Naidu, M. Ghanashyam Krishna, Philos. Mag. 94, 3431–3444(2014).
- [48] R. Swanepoel, J. Phys. [E]. 16, 1214 (1983).
- [49] J.C. Tauc, F. Abeles., North-Holland, Amsterdam, 1972.
- [50] H.Y. Tian, W.G. Luo, A.L. Ding, J. Choi, C. Lee, K. No, Thin Solid Films. 408, 200-205 (2002).
- [51] Y.H. Cheng, X.L. Qiao, J.G. Chen, Y.P. Wu, C.S. Xie, Y.Q. Wang, D.S. Xu, S.B. Mo, Y.B. Sund, Surface and Coatings Technology 160,269–276 (2002).
- [52] J. P. Zhao, Z. Y. Chen, T. Yano, T. Ooie, M. Yoneda, and J. Sakakibara, Journal of Applied Physics 89, 1634 (2001).

- [53] Yu. I. Yuzyuk, Phys. Solid Stat. 54, 1026 (2012).
- [54] R. Naik et.al, Phys. Rev. B, 61, 11367 (2000).
- [55] Q. Zhang, J. Zhai, L. Kong, X. Yao, J. Appl. Phys. 112, 124112 (2012).
- [56] L.Z. Cao, B.L. Cheng, S.Y. Wang, W.Y. Fu, S. Ding, Z.H. Sun, H.T. Yuan, Y.L. Zhou, Z.H. Chen, G.Z. Yang, J. Phys. Appl. Phys. 39, 2819 (2006).
- [57] S.Y. Wang, B.L. Cheng, C. Wang, S.Y. Dai, K.J. Jin, Y.L. Zhou, H.B. Lu, Z.H. Chen, G.Z. Yang, J. Appl. Phys. 99, 013504 (2006).
- [58] K. Sandeep, J.P. Goud, K.C. James Raju, IEEE, pp. 1–3, (2016).
- [59] S. Tappe, U. Böttger, R. Waser, Appl. Phys. Lett. 85, 624–626 (2004).
- [60] K. Sandeep, J. Pundareekam Goud, and K. C. James Raju, Applied Physics. Letters, 111, 012901 (2017).
- [61] J. Pundareekam Goud, K. Sandeep, E. Sivanagi Reddy, Mahmoud.S. Alkathy, K. Lakshun Naidu and K.C. James Raju, Ferroelectrics, 516, 1–8 (2017).
- [62] Spartak Sh Gevorgian, Alexander K Tagantsev, Andrei K Vorobiev, Engineering Materials and Processes-Tunable Film Bulk Acoustic Wave Resonators, Springer London (2013).

Chapter-5

Crystallization of BST thin films using laser irradiation at 300°C

5.1 Introduction

Laser annealing is a well explored technique for silicon technology, since 1980. In those years exploration was to grow low-temperature, poly-silicon species for thin film transistor-liquid crystal displays [1-2] which are commercially used in present day flat screen monitors. Recently, this technique is applied on oxide ferroelectric (FE) thin film material systems as well. Many research groups from all over the world are investigating the suitability of laser annealing for this application as it got the potential to integrate them with Si technology by lowering the average process temperature. Their investigation focus on identifying different ferroelectric materials suitable for bringing different functionalities into silicon. This includes various application fields like memory devices, tunable microwave devices and microelectromechanical systems (MEMS) etc. Laser annealing of various types of ferroelectric thin films such as PZT, PLZT, BZN, LMO, ZnO, BST are reported by research groups from around the world [3-20].

Specifically, S.T. McKinstry's group from Penn State, USA, are involved in studying low temperature crystallization of PZT and PLZT ferroelectric thin films employing laser irradiation. In general, ferroelectric thin films, which are crystallized at high temperatures (~700°C) have best functional properties, but limited device compatibility even in Si (integration to polymer and flexible substrates is excluded) [21, 22]. The integration of ferroelectric thin films onto polymers or on integrated circuits requires lower crystallization temperature (ideally near room temperature). Therefore, this is a process to integrate new functionalities in Si and possibly onto polymers which in turn might be able to bring out new sensors at lower cost [23]. One such prominent ferroelectric material that has been used extensively is Barium Strontium Titanate (BST). BST thin films are processed at higher temperatures of about 700°C. Integrating the BST thin film devices with the system-on-chip (SoC) opens up a whole new level of system capabilities.

The main bottleneck of integrating BST with SoC is that the process temperature of BST is too high. Hence it is worth exploring low-temperature processing of BST [24-26].

This chapter reports the optimization process for obtaining laser crystallization of amorphous thin-film of Ba_{0.5}Sr_{0.5}TiO₃ (BST5) by using KrF excimer laser of 248 nm. The ceramic target of BST5 is used for deposition of BST5 thin films by using pulsed laser deposition technique on fused silica (FS) substrates and are found to be amorphous in nature, when the deposition temperature is 300°C. Laser annealing processes are conducted at 300°C temperature with different optimizing parameters like number of laser pulses, energy density, and pulse repetition rate on the samples deposited at 300°C. To confirm crystallization of BST5 thin films after applying laser pulses, the phase, microstructural, vibrational and optical response are acquired and analysed. The experimental characterization techniques like X-ray diffraction, Field Emission Scanning Electron Microscope, Raman, UV-Vis-NIR spectroscopy, and transmission electron microscopy respectively are used. The results are compared with conventionally deposited BST thin films deposited at 700°C.

5.2. Experimental

5.2.1 Deposition of BST5 thin films

The BST5 thin films are deposited at 300°C and 700°C respectively on amorphous fused silica substrate by pulsed laser deposition (PLD) system. KrF Excimer laser of wave length 248 nm (Coherent-Compex Pro 102 F) with 5 Hz repetition rate is used. The deposition process of BST5 films are carried out in a spherical chamber (Excel Instruments, India). The chamber is evacuated to 5×10^{-6} mbar using turbo pump backed by mechanical pump. The chamber pressure is brought to 8×10^{-3} mbar by introducing oxygen for deposition of thin films. The distance between the target and substrate is

maintained at 5 cm. The depositions are carried out at constant oxygen working pressure and laser fluence of 2 J/cm². After deposition, the BST5 thin films are in-situ annealed for 30 min. in the presence of oxygen. Table 5.1 shows the deposition conditions of BST5 films. The thickness of 600 nm is chosen for the case of laser annealing, because in the conventional BST5 thin films it was found that films thinner than this value is prone to shorting under dc biasing conditions.

Table 5.1: Deposition conditions of Ba_{0.5}Sr_{0.5}TiO₃ films

Samples	Oxygen	Substrate	Repetition	Thickness	No. of	Laser
code	pressure	Temp.	Rate	(nm) ±6	counts	fluence
	(mbar)	(°C)	(Hz)	nm		(J/cm ²)
				From		
				FESEM		
BST5-300	8×10 ⁻³	300	5	600	10000	2
BST5-700	8×10 ⁻³	700	5	600	10000	2

5.2.2 Laser annealing of Ba_{0.5}Sr_{0.5}TiO₃ thin films

The laser annealing conditions of Ba_{0.5}Sr_{0.5}TiO₃ thin films that are used for studying the annealing process by varying different parameters like number of pulses, energy density and repetition rate. The laser annealing of these films is carried out by KrF Excimer laser of 248 nm wavelength. The deposition and laser annealing processes of Ba_{0.5}Sr_{0.5}TiO₃ films are carried out in two different spherical chambers (Excel Instruments, India), one for deposition with focused laser beam and the other with an expanded beam for laser annealing.

Laser annealing is carried out inside the annealing chamber at 300°C temperature (Figure 2.9). The amorphous BST5 thin films are positioned well on a clean metallic surface. Excimer lasers with KrF gas is used, which delivers excitation wavelength of 248 nm. The pulse length is estimated to be 20 ns (at 248 nm) by using a Gaussian fit of the

pulse shape. The average area of irradiation of the film at a typical energy density of 60 mJ/cm² is about 1 cm². The laser energy values are measured using energy meter (tolerance of about $\pm 5\%$). The pressure conditions for the chamber are kept similar to that of the deposition process.

5.3. Results and discussions

5.3.1 Effect of pulse counts

For optimization of laser annealing process to get a crystallized thin film, the first parameter considered is the pulse count. Table 5.2 gives the sample names and conditions with different laser pulse counts. Each of these samples are investigated and summarized in the following section.

Table 5.2: Laser annealing conditions of Ba_{0.5}Sr_{0.5}TiO₃ thin films

Ba _{0.5} Sr _{0.5} TiO ₃ thin films Samples code	No. of Laser pulses	Deposition/ Annealing temperature (°C)	Deposition/ Annealing pressure (mbar)	Rate of repetition of pulses (HZ)	Energy density (mJ/cm ²)
(a) LA 300 FS -50	50	300	8×10 ⁻³	5	60
(b) LA 300 FS -250	250	300	8×10 ⁻³	5	60
(c) LA 300 FS -500	500	300	8×10 ⁻³	5	60
(d) LA 300 FS -1000	1000	300	8×10 ⁻³	5	60
(e) LA 300 FS -2000	2000	300	8×10 ⁻³	5	60
(f) LA 300 FS -3000	3000	300	8×10 ⁻³	5	60

I. Phase and structural analysis

The structural properties and phase of the films were studied by Grazing Incidence X-ray diffraction (GI-XRD-Bruker D8 Discover) at 40 kV and 30 mA with a Cu Kα radiation source of wavelength ~1.5406 Å. The XRD pattern of BST5 films on amorphous fused silica deposited at 700°C and 300°C temperature with constant fluence and oxygen working pressure are shown in fig. 5.1(a). The as-deposited films on FS substrates deposited at 300°C are designated as ADF 300FS and the same deposited at 700°C are designated as ADF 700 FS.

X-ray diffraction patterns of the BST5 films after laser irradiation with 50, 250, 500, 1000, 2000 and 3000 pulses each of 60 mJ/cm² energy density, are shown in fig. 5.1(b). This result indicates signs of crystallization appearing at around 250 pulses, and as the pulse count increases the intensity of the XRD peaks also increases. The XRD pattern of the laser annealed BST5 films with increasing no. of laser pulses shows an increase in crystallinity and a corresponding increase in the peak intensity of reflection from different crystal planes. Similar structural results with laser annealing of ferroelectric films is reported elsewhere [14,15,27-29]. Also, the diffraction peaks of the BST5 films get shifted to lower diffraction angles with increasing no. of laser pulses, which indicates an increase in lattice parameter and unit cell volume [30,31].

The variation of crystallite size with laser pulses is calculated using the Debye Scherrer method as shown in Table.5.3. It is clear that the crystallite size increases with no. of laser pulses from 250 to 2000 and decreases for 3000 pulses. Based on these observations presented in Table 5.3, it is confirmed that the use of 2000 no. of pulses is favorable for crystallization of films than other cases.

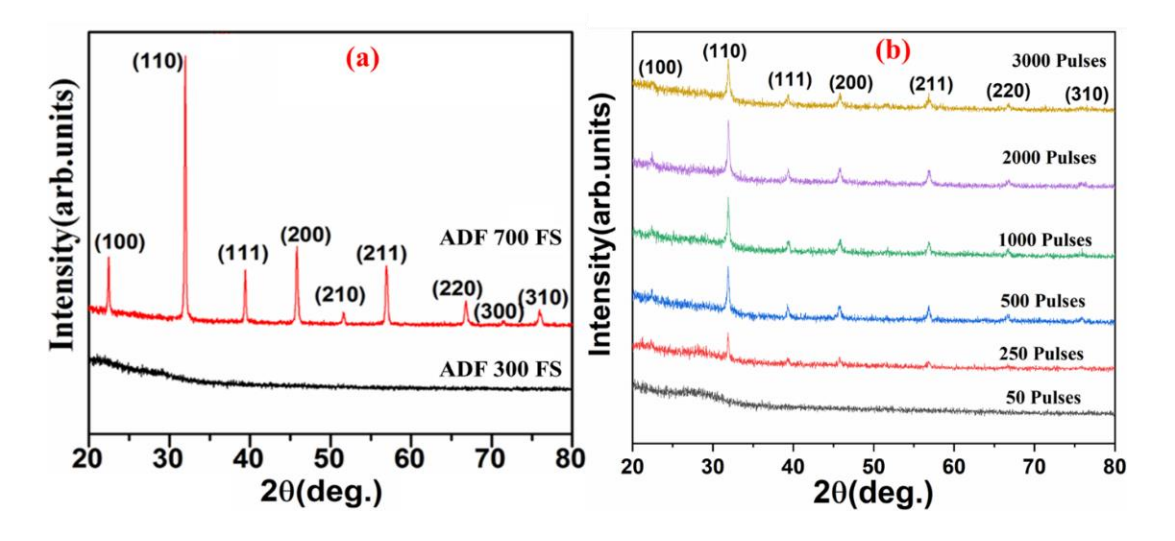


Fig. 5.1. X-ray diffraction pattern of BST5 thin films (a) Deposited at 700°C and 300°C (b) Films on FS substrates deposited and laser annealed at 300°C with 50, 250, 500, 1000, 2000 and 3000 number of annealing pulses.

Table.5.3: Crystallite size and Grain size values of BST5 thin films grown on FS and laser annealed at 300C with different number of laser pulses.

(BST5) Thin film Samples code	Counts (or) No. of Laser pulses	Crystallite size (D-S) (nm) ± 2 nm	Grain size (µm) from FESEM
(a)	50	-	-
(b)	250	19.2	0.51
(c)	500	24.61	0.55
(d)	1000	26	0.79
(e)	2000	27.1	1.01
(f)	3000	23.08	0.48

II. TEM Analysis

The TEM studies for ADF 300 FS and ADF 700 FS are carried out and the results are shown in fig. 5.2. It can readily be seen that the former remains amorphous while the latter gets crystallized into a polycrystalline film. ADF 300FS are laser annealed with laser pulses of 60 mJ/cm² energy density using 50, 250, 500, 1000, 2000 and 3000 pulses at 300°C (LA 300FS -50 to LA 300FS - 3000 respectively) and their bright field TEM images are given in fig. 5.3(i)a-(vi)a. It is clearly seen that the crystallization started from 250 pulses, and the crystallite size increased as the number of laser pulses increases. Also these evolved crystallites are of irregular shape embedded in a background of amorphous matrix. Fig. 5.3 (i)c-(vi)c shows the HRTEM images of the films, the HRTEM images are with (110) lattice fringes of BST crystal and the d-spacing is in the range of 2.72-2.79Å.

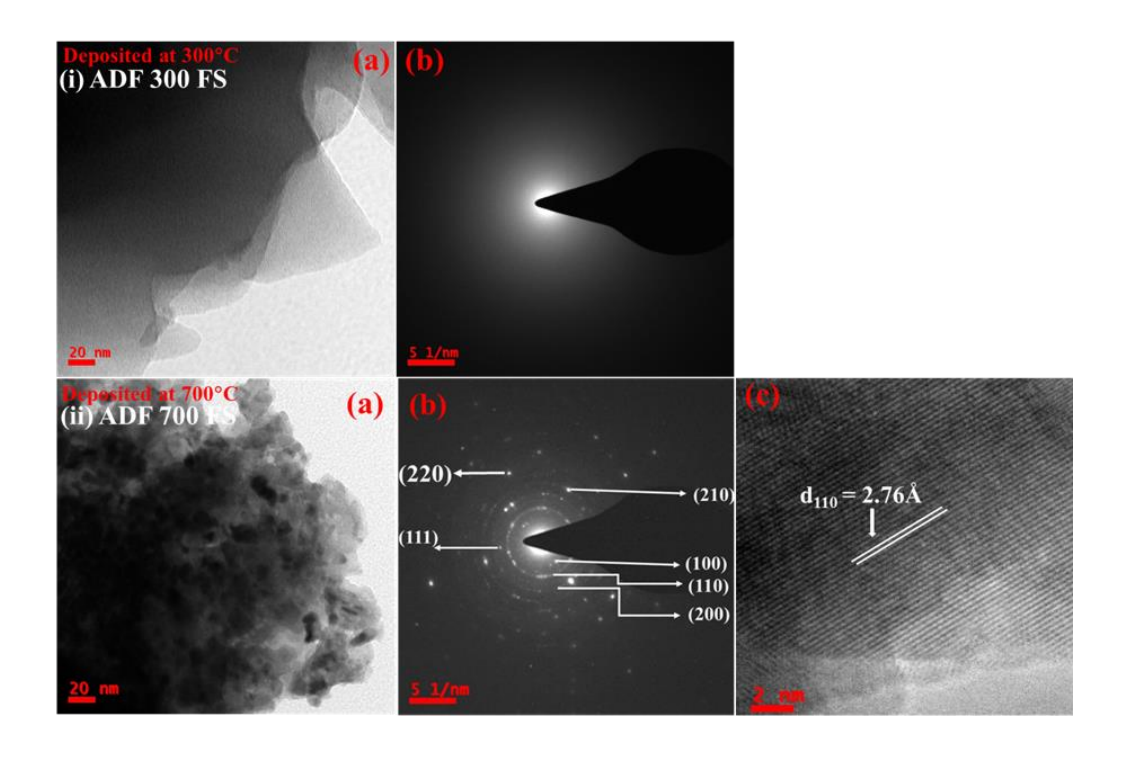


Fig. 5.2. The images in columns (a) (b) and (c) shows the TEM Bright field, selected area Diffraction (SAED) and HRTEM patterns of BST5 thin films respectively.

(i)ADF 300 FS (ii) ADF 700 FS.

From the SAED pattern it confirms the polycrystalline nature for laser irradiated films, which are annealed with 250 to 3000 pulses. These spot diffraction patterns are originating from many small grown nanocrystals as source of diffraction (Fig 5.3 (i)c–(vi)c). The recorded SAED pattern ring diameter matches well with standard JCPDS card no (file # 39-1395) supporting localized BST5 structural growth at all no. of laser pulses applied in the present study. Similar TEM microstructural evolution of ferroelectric films, under conventional and laser annealing cases are reported elsewhere [27,28,32-34]. The crystal structure examined by HRTEM and SAED measurements shows that the LA300FS-250 films consist of nano-size crystallites with dimensions of about 7-12 nm. However, LA300 FS-2000 films give densely packed crystallites as can be seen from the HRTEM shown in fig. 5.3 (v)-c.

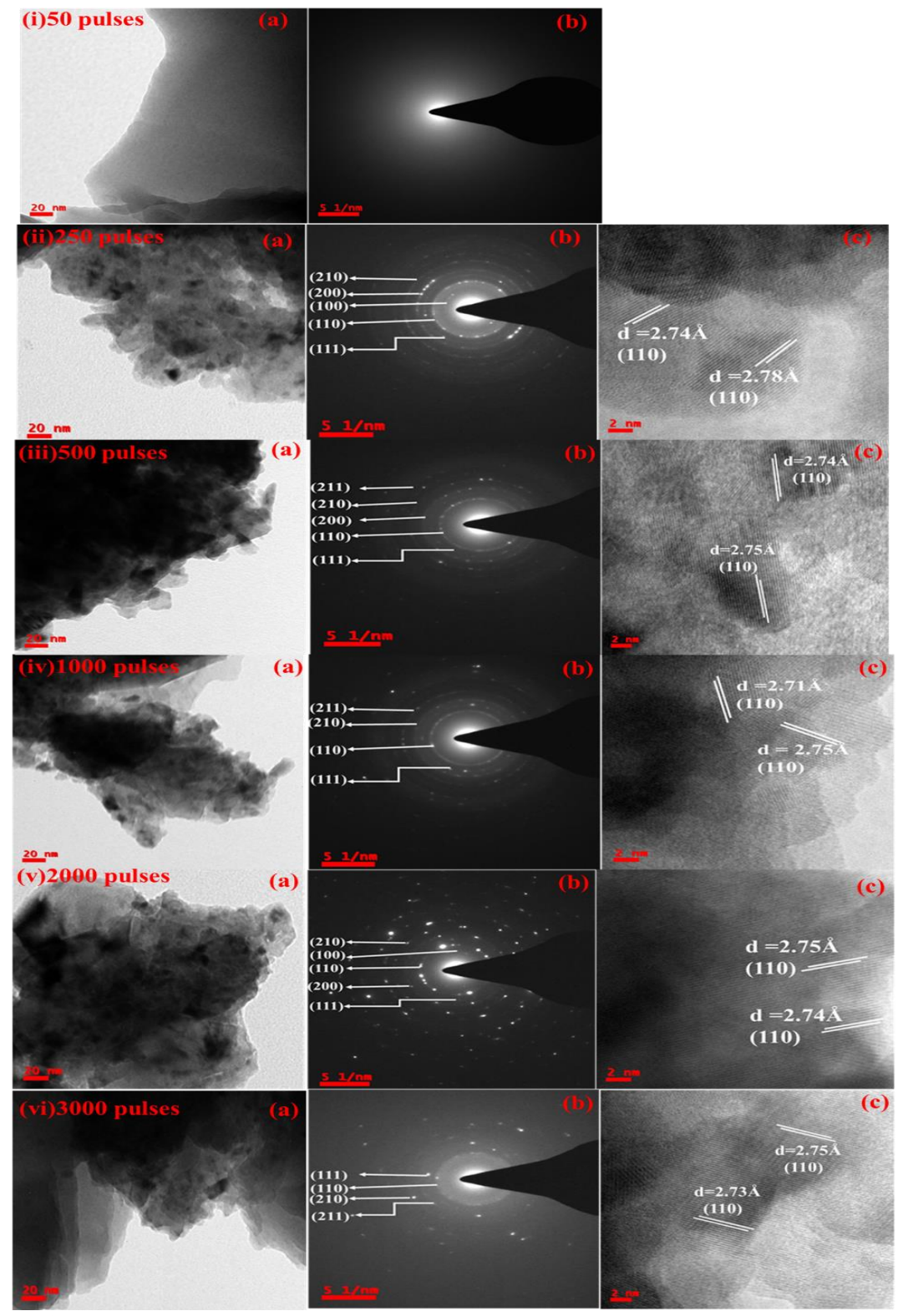


Fig. 5.3. (i)-(vi) TEM images of BST5 films laser annealed with different laser pulses (a) Bright field images (b) Selected area diffraction (SAED) patterns and (c) HRTEM.

III. Microstructure properties

The morphology and surface microstructure of the BST5 films are observed by FESEM. The microstructure and cross-sectional SEM of the as-deposited BST thin films deposited at 300°C (ADF 300 FS) and films deposited at 700°C (ADF 700 FS) are shown in the fig. 5.4. ADF 300 FS films are microstructurally smooth, thereby indicating their amorphous nature. Fig. 5.5 gives the FESEM images of the LA 300FS -50 to LA 300FS-3000 films that are laser annealed at 300°C with a laser energy density of 60 mJ/cm² with 50, 250, 500, 1000, 2000 and 3000 number of pulses respectively. At no. of laser pulses of 50, the films are smooth surfaced. As the no. of laser pulses increased to 250, the FESEM images of BST5 film shows evolution of fine grains.

These observed fine granular structures suggest the crystalline phase evolution, when irradiated (Fig. 5.5) with 250 shots of laser pulses and higher. As shown in the micrographs, grains were formed uniformly in the BST thin films which were irradiated with 250, 500, 1000, 2000 and 3000 number of pulses. The grains have further grown with increasing number of laser annealing pulses as seen by other workers [14,16,35].

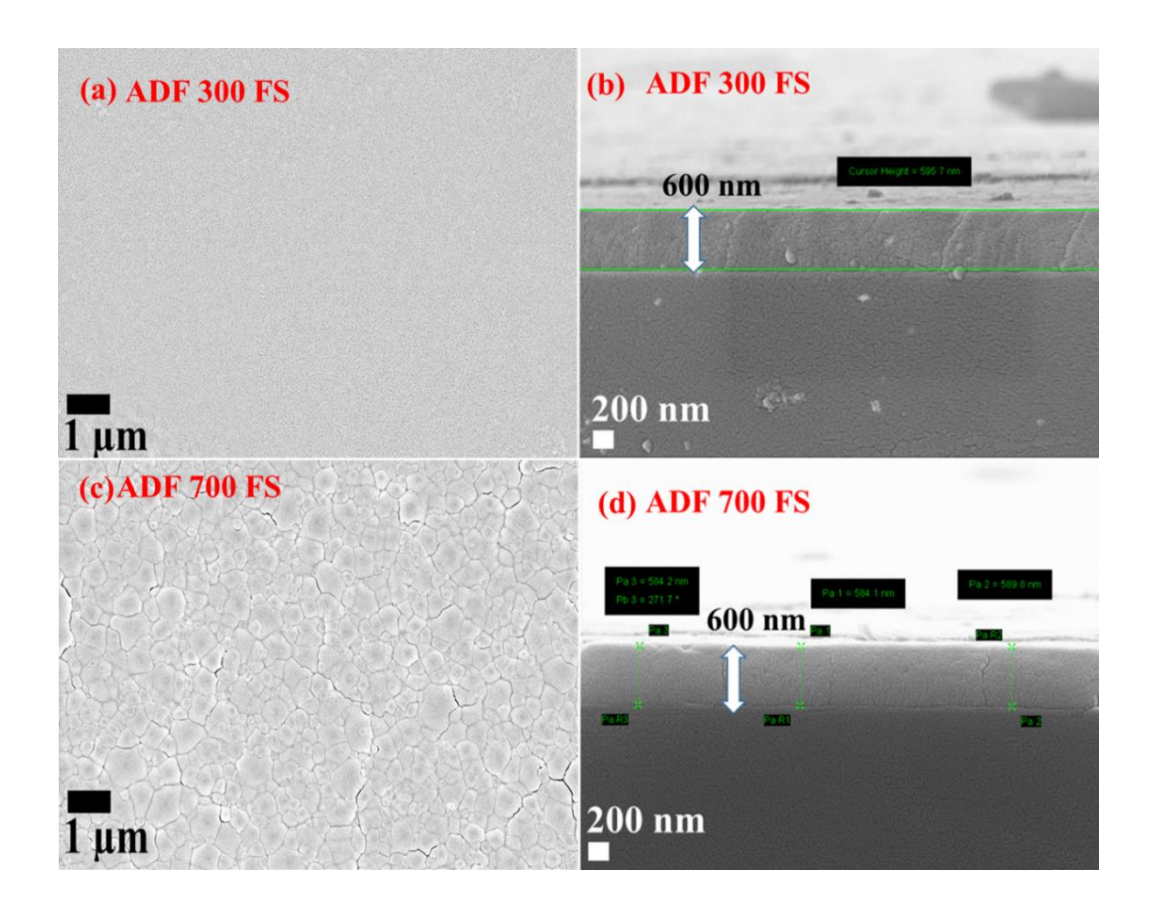


Fig.5.4. FESEM images (a, c) and Cross-sectional SEM (b, d) of ADF 300 FS and ADF 700 FS.

Finally, when the laser pulses reach 2000, FESEM image of the films exhibits different grains with varying sizes as shows in fig. 5.5 histogram. The appearance of well-defined grains at 2000 pulses shows the onset of a favorable condition for nucleation and grain growth in these films. The microstructure of the ADF 700 FS and the Laser annealed film deposited at 300°C with 2000 pulses (LA 300 FS-2000) show that both are dense films with clear grains (smooth surfaced). The surface morphology of LA 300 FS-2000 is smoother with least void and cracks in between clusters, thereby qualitatively better for electrical measurements [36], possibly with better breakdown strength.

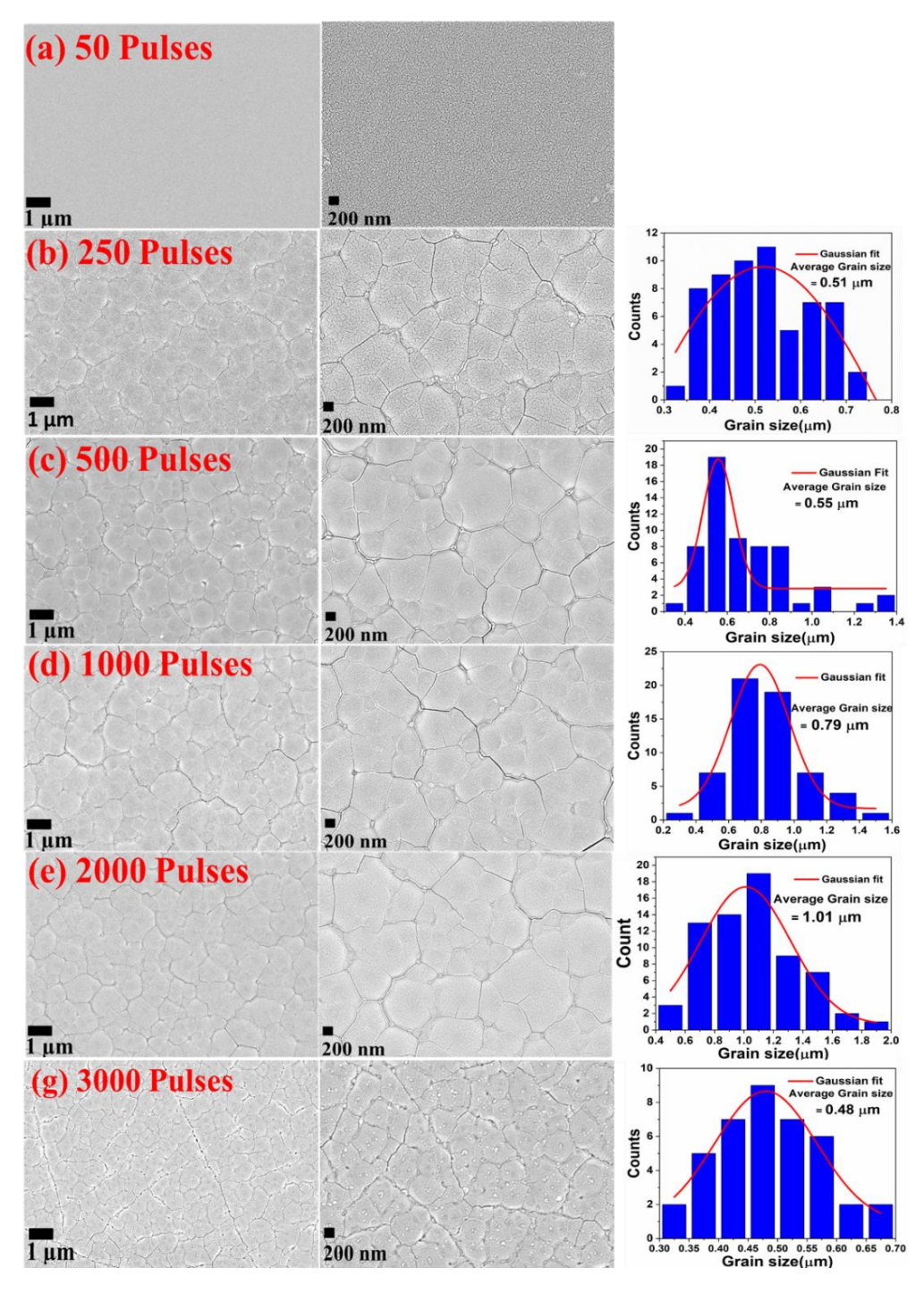


Fig. 5.5. The FESEM images of LA 300FS -50 to LA 300FS - 3000: BST5 films laser annealed with different number of laser pulses. At different magnifications and the histogram of grain sizes observed.

IV. Optical properties:

A. Raman studies

The Raman spectra of the Ba_{0.5}Sr_{0.5}TiO₃ (BST5) thin films are recorded at room temperature (RT). BST5 laser annealed samples LA 300FS -50 to LA 300FS- 3000 are plotted in fig. 5.6. The fused silica amorphous substrates are Raman inactive based on their crystal symmetry, therefore will have no contribution to the film Raman signals. The observed phonon modes are located at around 260-300, 480-515 and 800-805 cm⁻¹ respectively. These are for BST5 thin films annealed with no. of laser pulses of 50, 250, 500, 1000, 2000 and 3000. However, the observed dominant phonon modes are in the range of 180-186, 260-282,520-535 and 720-740 cm⁻¹ for the BST5 conventionally crystallized films [37-43]. Clearly a blue shift of phonon modes occurs for laser annealed films, suggesting evolution of crystallinity and the state of strained crystallites constricted by amorphous matrix around. From the comparison of these observed Raman modes of BST5 thin films after laser annealing with increased laser pulses; it can be inferred that the observed Raman modes for films annealed with lower number of laser pulses are relatively less intense than that of the films annealed with higher number of laser pulses. That is, as the number of annealing laser pulses increases, the phonon mode intensity increases. These observations of Raman spectra suggest that at 2000 pulses, laser annealed films exhibited better crystallinity than that for both higher and lower number of annealing pulses.

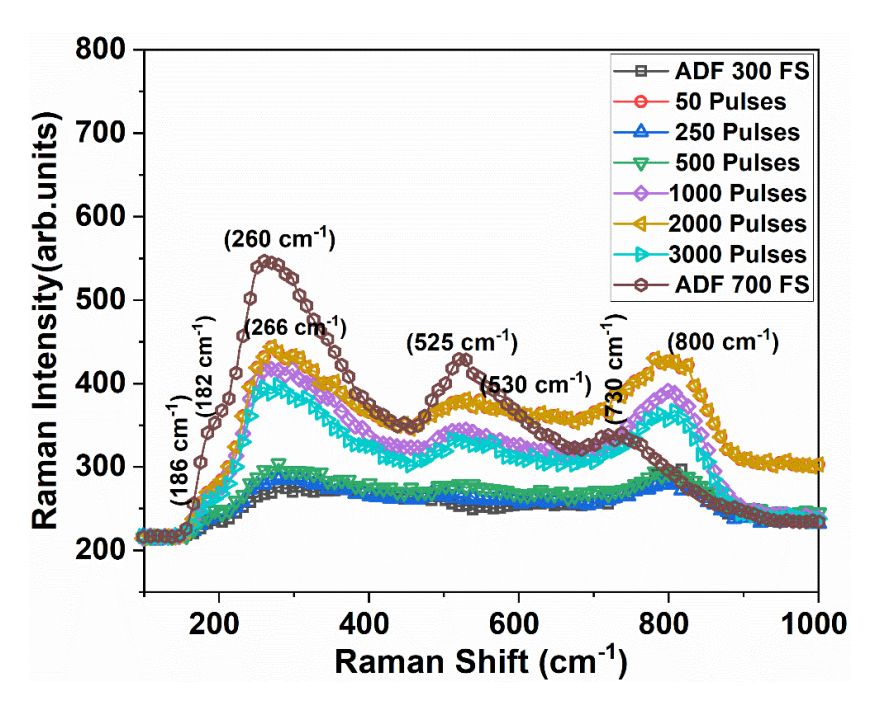


Fig.5.6. Raman spectra of BST5 thin films annealed with different no. of laser pulses in comparison with *in-situ* crystallized films and as deposited films.

B. Band gap studies

The measured transmission spectra for laser annealed films in the wavelength range of 190-2500 nm are shown in fig. 5.7 (a). These films are transparent in the visible and near-infrared regions. All these films have sharp absorption edge around 300 nm, and which is used to determine the optical band gap [44-46]. A substantial change in the interference fringes of transmission spectra can be seen with increased no. of annealing laser pulses.

The optical band gap is calculated by using the Tauc's relation.

$$\alpha h \vartheta = A(h\vartheta - E_g)^{\frac{1}{2}}$$
 5.1

Where A is a constant, $h\vartheta$ is the photon energy, ϑ is the frequency and the absorption coefficient α is given as,

$$\alpha = \frac{\ln\left(\frac{1}{T}\right)}{d}$$
 5.2

Where, d is the thickness of the film, and T is transmittance.

The $(\alpha h\vartheta)^2$ Vs $h\vartheta$ is plotted (Fig.5.7 (b)) and fitted using equation (5.1). The calculated band gap values for films that are laser annealed with different no. of pulses are shown in Table. 5.4. From the Tauc plot (Fig. 5.7 (b)), it is clear that the band gap of the films decreases from 4.58eV to 3.86 eV with no. of laser pulses increasing from 50 to 2000 respectively. Thereafter for 3000 pulses a reverse trend is observed. The decreased band gap is a well-known consequence of crystallization of thin films [31,47]. It could be noticed that annealing with 2000 pulses show bandgap value approaches close to that of conventionally crystallized BST5 films. Hence it is considered as optimal. The band gap of thin film depends on various factors like crystallite size, grains size, lattice parameters and lattice strain and film thickness [52]. Here we obtained crack free large grain high quality thin film for 2000 pulses. If we further increased no. of pulses because of higher thermal stress the films undergoes display visible cracks and forming smaller grains size as shown in fig. 5.5(g). This leads to the observed decrease in bandgap above 2000 pulses [31,47].

Table.5.4: Bandgap values of BST5 thin films annealed with different number of laser pulses.

BST5 thin films	No. of Laser pulses	Band gap
Samples code		(eV)
		±0.02
ADF 300 FS	As deposited at 300°C	4.58
LA 300 FS -50	50	4.53
LA 300 FS-250	250	4.46
LA 300 FS-500	500	3.96
LA 300 FS-1000	1000	3.91
LA 300 FS-2000	2000	3.86
LA 300 FS-3000	3000	3.93
ADF 700 FS	As deposited at 700°C	3.54

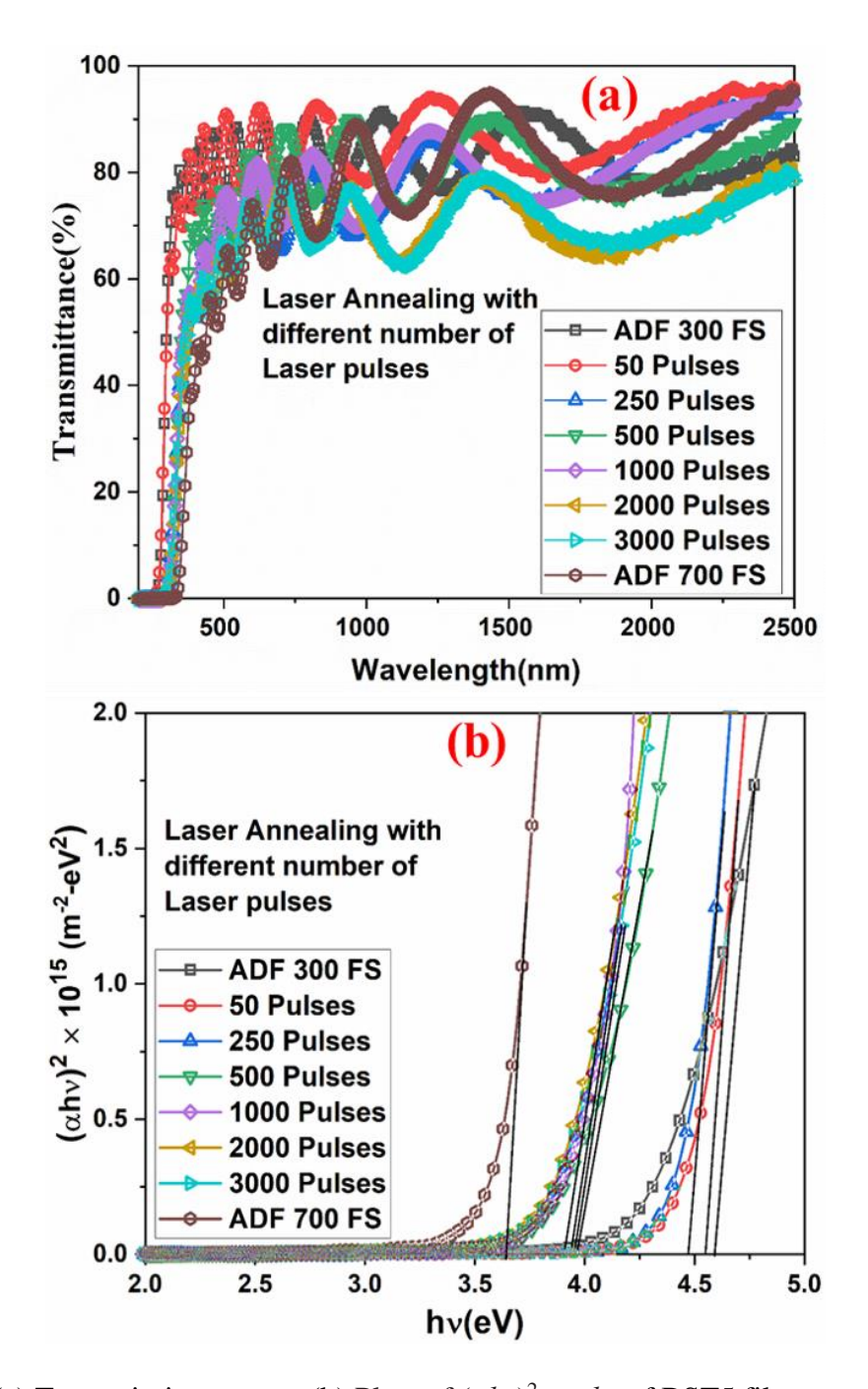


Fig. 5.7. (a) Transmission spectra (b) Plots of $(\alpha hv)^2$ vs. hv of BST5 films annealed with different no. of laser pulses.

5.3.2. Laser annealing: Effect of pulse repetition rate

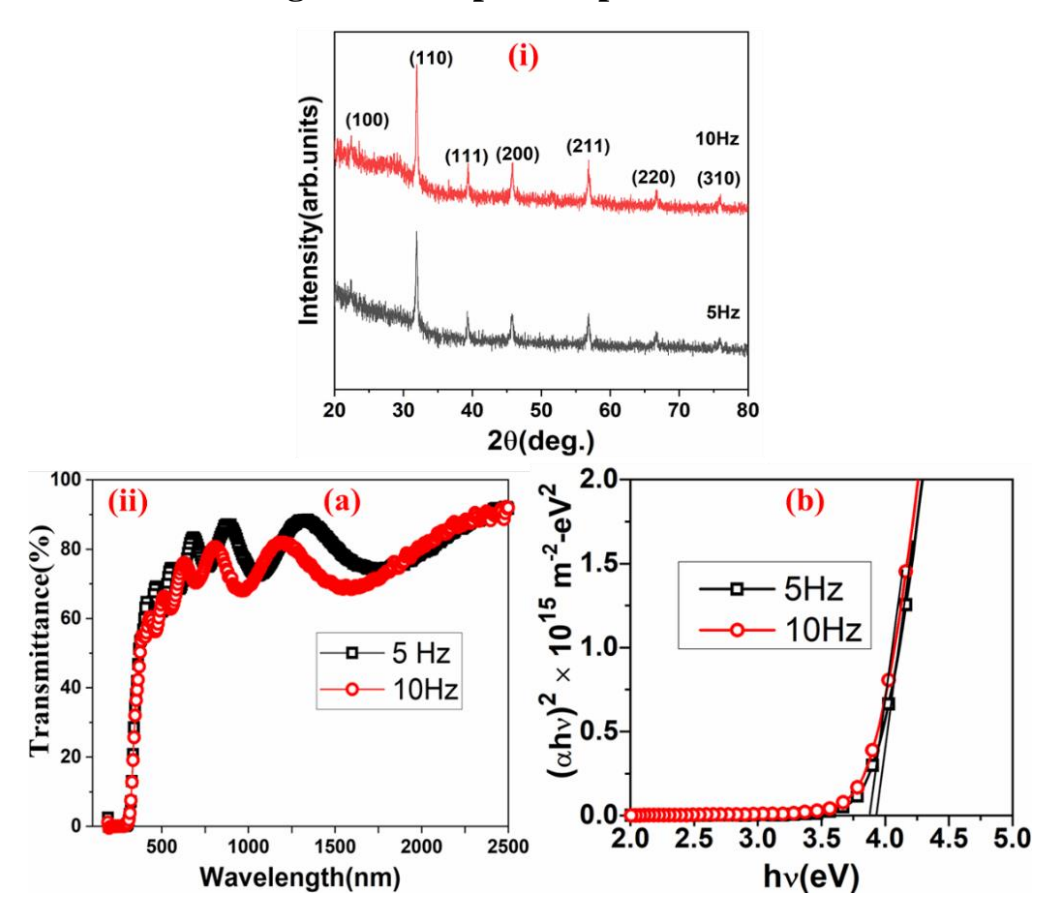


Fig. 5.8. Effect of pulse repetition rate on laser annealed films (i) XRD pattern for films annealed at 5 and 10Hz. (ii) Corresponding optical spectra (a) Transmission spectra (b) Plots of $(\alpha h v)^2$ vs. hv.

Table 5.5: Effect of pulse repetition rate during laser annealing.

Rep.	Energy	Deposition/	No of	Film	Band	Crystallite
Rate	density	Annealing	pulses	Thickness	gap±	size
(Hz)	(mJ/cm^2)	temperature		(nm)	0.02 eV	± 2 nm
		(°C)				
5	60	300	2000	600	3.86	27.1
10	60	300	2000	600	3.82	28

As per the above laser annealing results (see Table-5.3& 5.4) with varying number of laser pulses used for annealing, it is observed that 2000 pulses will yield the optimized crystallization. Thereby, now the 2000 pulses and 60 mJ/cm² energy density are kept

constant. Next the effect of variation in pulse repetition rate (i.e. 5Hz and 10 Hz) is investigated. Fig. 5.8 (i) shows the XRD pattern of laser annealed BST5 films with these repetition rates. From the XRD patterns, it is observed that intensity of XRD peaks increases with increase in pulse repetition rate, i.e. for the case of 10 Hz the crystallite size increases (Table 5.5). UV-VIS-NIR optical band gap for films grown with at 5Hz and 10 Hz repetition rate are computed using the data from fig. 5.8 (ii) to see its effect on band gap. Tauc's relation (Equation 5.1 &5.2) is used for this purpose. Band gap values for films grown at 5Hz and 10 Hz repetition rate are 3.86 and 3.82 eV respectively (Table 5.5). Clearly, band gap narrowing is observed for 10 Hz repetition rate. Bharadwaja et al. reported similar results on the phase pure perovskite PLZT thin films which are laser annealed at a repetition rate of 10 Hz supporting band gap narrowing with crystallization [9].

The laser induced crystallization of the BST thin films have slightly improved when the pulse repetition rate is increased from 5 Hz (B.G.~3.86) to 10 Hz (B.G.~3.82). The decrease in bandgap value is not significant which shows that the laser pulses with still higher rep rate should be used, however, higher rep rate is not possible due to the limitation of the system. To proper anneal the thin films, high rep rate is useful since the material is heated continuously and the surface temperature must be getting maintained as heat can diffuse only to the substrate side. When low rep rate is used, the film is heated with first pulse and temperature and pressure generated could get lowed by the time the next pulse come after a long gap. This will limit the full vertical LIC of BST thin films.

5.3.3 Laser annealing: Effect of laser energy density

Results of the optimization of no. of laser pulses and repetition rate on laser annealing of BST films is tabulated in Table-5.3, 5.4 & 5.5. The optimum conditions are identified as 2000 pulses and 10 Hz pulse repetition rate. After fixing these parameters, the effect of laser energy densities is explored by annealing the BST5 films at 60 mJ/cm² and 66 mJ/cm². Fig 5.9 (i) show the XRD pattern after laser annealing process. The XRD peaks intensity increases and bandgap decreases with increasing laser energy density, along with increase in crystallinity. Table 5.6 summarizes bandgap and crystallite dimension of BST5 films deposited on fused silica and laser annealed. The measured transmission spectra of the laser annealed films in the wavelength range of 190-2500 nm are shown in fig. 5.9(ii). The band gap of the films decreases from 3.82 eV to 3.78 eV with increase in energy density of the annealing beam and bandgap values approach that of the conventional BST5 thin films. These results demonstrate the potential of excimer laser for crystallization of amorphous ferroelectric BST films.

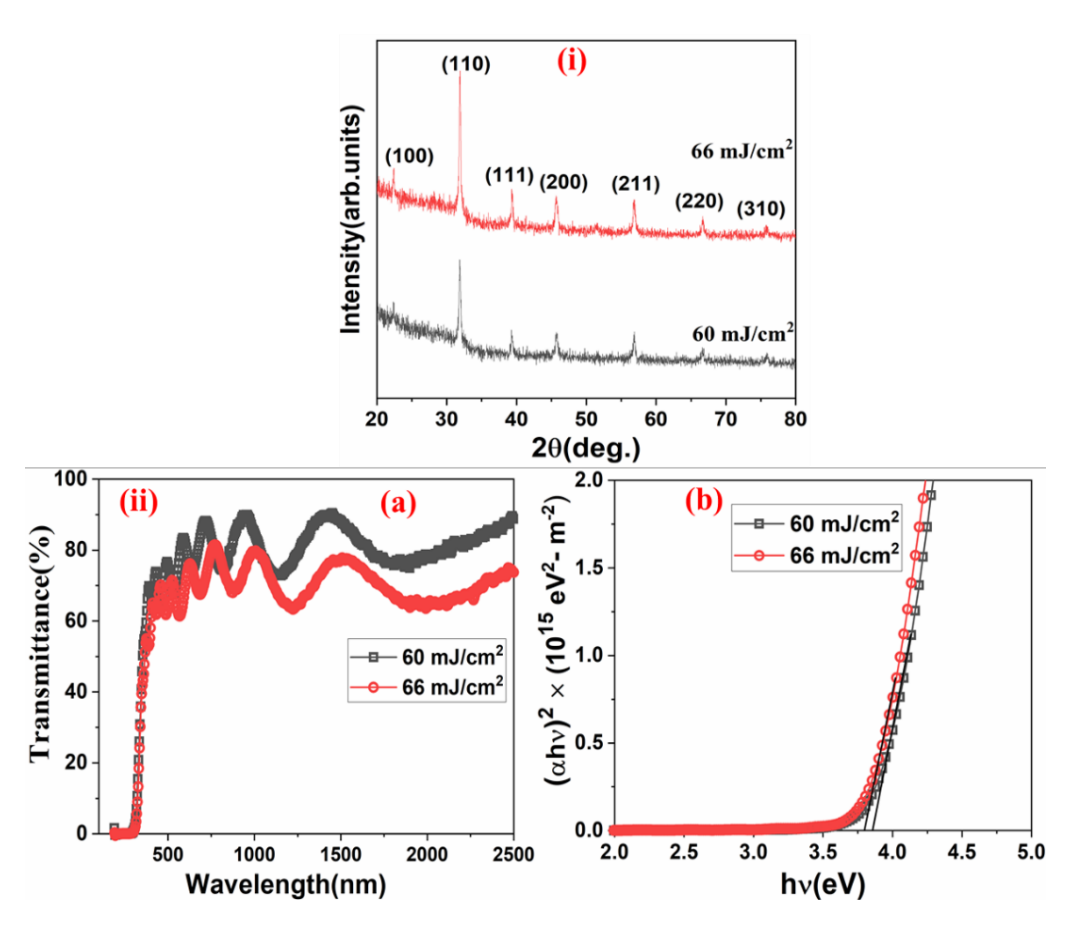


Fig.5.9. Effect of Laser energy density on laser annealed films (i) The XRD pattern (ii) (a) Transmission spectra (b) Plots of $(\alpha h v)^2$ vs. hv.

Table 5.6: Effect of energy density of annealing laser beam

Energy density (mJ/cm ²)	Rep. rate (Hz)	Deposition/ Annealing temperature (°C)	No of pulses	Film Thickness (nm) ±6 nm	Band gap (eV) ±0.02 eV	Crystallite size (nm) ± 2 nm
60	10	300	2000	600	3.82	27.89
66	10	300	2000	600	3.78	29

The laser energy required for the crystallization process is important as in laser ablation. For example, the best electrical properties for PLZT thin films were obtained by exposing them to an excimer laser irradiation of 200 mJ/cm² energy density [9]. In pulsed laser annealing, crystallization starts on the surface of the film due to the heating induced

by absorption of the laser light, and the shock waves generated. Lower energy is not sufficient for the lattice mending process and high energy can ablate the film and hence Energy Density is to be optimized for the LIC process.

5.4. Microwave characterization

The Microwave measurement techniques employed demand the growth of films on a conducting surface. Hence the BST films were grown by the same optimized protocol but on Platinum Coated Silicon (PS). Dielectric properties of Ba_{0.5}Sr_{0.5}TiO₃ (BST5) thin films in the microwave frequency range are measured for the as-deposited film (ADF 300 PS), as-deposited film (ADF 700 PS) and optimized laser annealed (LA 300 PS) films. The active ferroelectric thin layer, i.e. BST5 of thickness around 600 nm was deposited on the Platinized Silicon (111) substrate using the pulsed laser deposition (PLD) system operated at the optimized laser fluence of 2 J/cm². Au of 150 nm thickness is deposited using RF sputtering and is patterned by photolithography to be used as the top electrode [31,48-50].

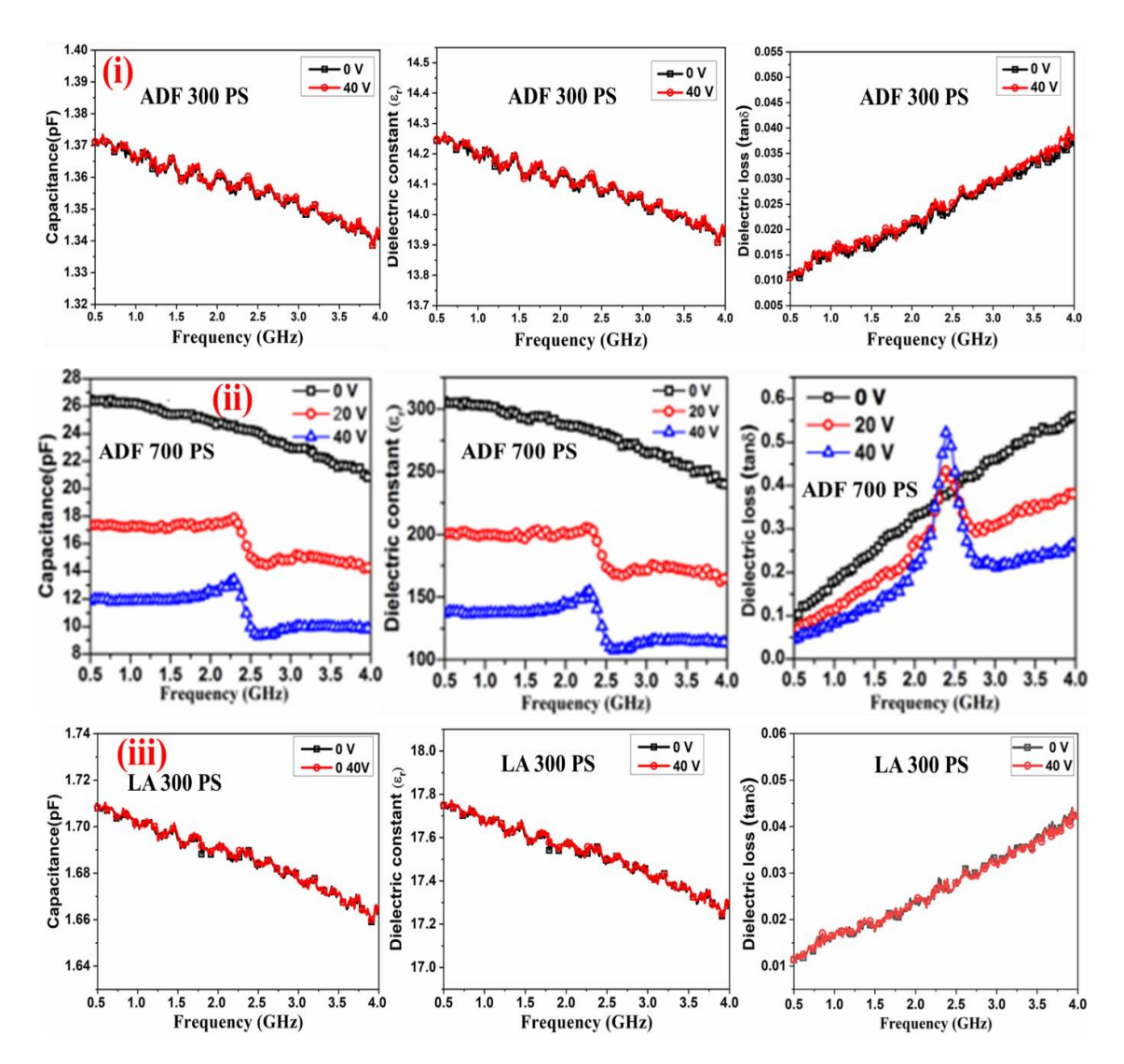


Fig.5.10. Capacitance, dielectric constant & dielectric loss parameters of Ba_{0.5}Sr_{0.5}TiO₃ (BST5) thin-films of (i) ADF 300 PS (ii) ADF 700 PS and (iii) LA 300 PS on platinized silicon substrates.

Microwave measurements of the fabricated Circular Patch Capacitor (CPC) are done using an on-wafer probe station and an Agilent E8361C network analyzer. The Sparameters (S₁₁) are measured for a range of frequencies, and by applying different DC bias voltages. The capacitance of BST5 thin films have been plotted from the frequency range of 0.5 - 4 GHz with, and without biasing as shown in fig. 5.10. [31,48-50]. The Ba_{0.5}Sr_{0.5}TiO₃ thin films have very high dielectric permittivity, and its dependence on external DC bias provides an additional well-known feature extraction, called tunability. The mathematical relation is stated below as:

Tunability (%) =
$$\frac{C(0) - C(E)}{C(0)} \times 100$$
 (5.3)

Where C (0), and C (E) are the dielectric capacitance values at zero and non-zero DC electric bias field respectively. Using equation (5.3) for the ADF 700 PS film, the extracted microwave tunability obtained is 54 % at a frequency of 1 GHz. Similarly, the dielectric constant of the film is 301 at 1 GHz without DC bias (Fig 5.10(ii)).

For low temperature deposited BST films (300°C) no tunability response is obtained (Fig. 5.10(i)). Tunability is a feature characteristic of the crystalline order in a ferroelectric. These films are eventually subjected to laser annealing for crystallization. The microwave dielectric properties of laser annealed BST films are shown in fig. 5.10(iii). In fact, laser annealed BST films also does not show any tunability in microwave frequency range. To further understand this non-tunability nature of the crystallized laser annealed films, TEM cross-section for depth of crystallization is investigated in the next section.

Queralto et. al. [18] has crystallized BST8 thin films with a KrF excimer laser in the oxygen ambient at fluences ranging from 50 to 75 mJ/cm². However, 160 nm thick films, shows the crystallization only up to 70 nm depth. The rest of the film remained amorphous due to the large temperature difference between the film surface and substrate interface due to low thermal conductivity of the amorphous BST and also owing to the nature of the lattice mending process initiated by the pressure wave created by the process. In the present work from the cross-sectional TEM images of BST5 thin films as shown in fig.5.11, it is confirmed that crystallization occurs only up to a limited depth of 120 nm out of 600 nm film thickness. The uncrystallized amorphous layer dominates the dielectric properties of BST films as field is applied across the whole 600 nm thickness.

5.5. Cross-sectional TEM

The laser annealed BST5 thin films are investigated for crystallinity by employing cross-sectional TEM analysis. Intended sample portions are thinned for electron transparency. During the cross-sectional TEM sample preparation, apparatus like Gatan 623-disc grinder and emery paper (silicon carbide grinding paper) are used for polishing. After sample (film sandwiched between substrates) polished up to 40 µm thick and this sample are ion milled for obtaining electron transparent regions using precision ion polishing system or PIPS (Model 691, Gatan) [51].

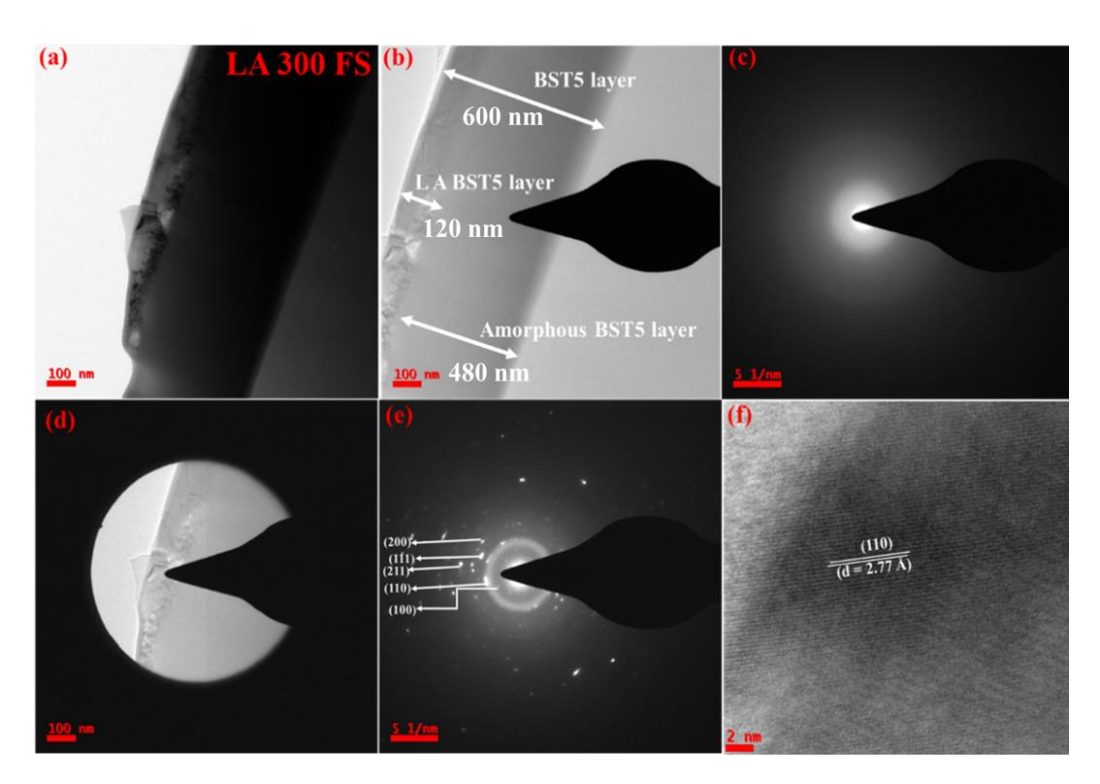


Fig.5.11. Cross-sectional TEM Images of BST5 thin films on fused silica substrates.

The cross-sectional TEM images acquired for optimized LA 300 FS are shown in fig.5.11. The electron transparent wedge-shaped section of 120 nm laser annealed section for crystallization probing in TEM bright field mode is shown in fig 5.11(a). A contrast in brightness can be seen from the wedge edge to FS substrate. To distinguish the beneath amorphous BST5 region from the surface crystallized section SAED mode is employed.

As seen in fig 5.11(d), the amorphous portion of BST5 cannot be completely discarded. TEM BF image of fig.5.11(b) and corresponding TEM SAED shown in fig.5.11(c) supports the amorphous nature of BST5 in as deposited state. Observation of spot pattern (i.e., Fig. 5.11(e)) and HRTEM lattice fringes are in support of crystallization obtained by laser annealing as seen in fig. 5.11(e), and (f) respectively. We can see that the crystallization has resulted in islands of crystallites which are not contiguous. This explains the lack of microwave tunability that is observed. Further optimization is required to achieve microwave tunability in these films.

Optimized parameters for laser annealing tabulated

Table 5.7. The list of optimized parameters for laser annealing

Substrate temperature during film deposition	300°C
Substrate temperature during laser annealing	300°C
Energy density (mJ/cm²)	66
Counts(or) No. of Laser pulses	2000
Rep.Rate (Hz)	10
Film thickness (nm)	120
Oxygen pressure (mbar) (During deposition/ annealing)	8×10 ⁻³

The Table 5.7 lists the optimized parameters for laser annealing of BST thin films deposited by PLD. Based on the conclusions extracted from XRD (crystallization), UV-VIS-NIR (band gap narrowing), and FESEM (clustering leading to grains).

5.6. Conclusions

This chapter is an illustration of laser annealing studies of Ba_{0.5}Sr_{0.5}TiO₃ (BST5) employing optimized PLD deposition at 300°C. As-deposited BST5 films are amorphous. Whereas crystallization of these films, with optimized laser annealing parameters (KrF Excimer laser of wave length 248 nm operated at 10 Hz, 2000 pulses, laser energy density delivered at 66 mJ/cm²) is confirmed by XRD. In fact, crystallite size is observed to increase with the increase in number of pulses (i.e. from 250 to 2000), and is adjudged to be coalescence of nano crystallites. The nano crystallites coalescence leading to larger granular grains evolution is supported by FESEM observations. Moreover, the UV Vis NIR optical spectroscopy investigation results are also in concurrence. A significant band gap narrowing with crystallization is another supporting affirmation.

Cross-sectional TEM investigations are carried out to evaluate the crystallization of optimized BST5 films. These microstructural detailing suggest that up to a thickness of about 120 nm, the film is crystallized with the use of current optimized laser annealing parameters. Based on this, as presented in Chapter-6, a layer-by-layer deposition and subsequent annealing after each deposition was done to obtain the microwave device quality films of 600 nm thick BST5. Clearly these layer-by-layer deposited and laser crystallized films at 300°C will be of extensive use extending from polymer to ceramic substrates, than its conventionally prepared counterparts deposited at 700°C.

References

- [1] I.B. Khaibulin, E.I. Shtyrkov, R.M. Bayazitov and M.F. Galjautdinov, Radiant Eff., 36, 225-233 (1978).
- [2] P. Baeri and E. Rimini, Laser Annealing of Silicon, Mater. Chem. Phys., 46,169-177 (1996).
- [3] Y. Zhu, J. Zhu, Y.J. Song and S.B. Desu, Appl. Phys. Lett. 73,1958-1998 (1998).
- [4] J. G. Cheng, J. Wang, T. Dechakupt and S.T. McKinstry, Appl. Phys. Lett.,87,232905 (2005).
- [5] T. Nakajima, T. Tsuchiya, M. Ichihara, H. Nagai and T. Kumagai, Appl. Phys. Express, 2,023001 (2009).
- [6] O. Baldus and R. Waser, Appl. Phys. A, 80,1553 (2004).
- [7] O. Baldus and R. Waser, J. Eur. Ceram. Soc., 24, 3013-3020 (2004).
- [8] S. Bharadwaja, J. Kulik, R. Akarapu, H. Beratan and S.T. McKinstry, IEEE Trans. Ultrason. Ferrolelect. Freq. Control, 57, 2182-2191(2010).
- [9] S.S.N.Bharadwaja, T. Dechakupt and S.T. McKinstry, H. Beratan,J. Am. Ceram.Soc.,91,1580–1585 (2008).
- [10] A. Rajashekhar, H.-R. Zhang, S. Bharadwaja Srowthi, I.M. Reaney and S.T.McKinstry, J. Am. Ceram. Soc., 99, 43–50 (2016).
- [11] S.U. Park, J.H. Koh, J. Alloys and Comp. 615,1032–1036 (2014).
- [12] W.T. Hsiao, S.F. Tseng, C.K. Chung, D. Chiang, K.C. Huang, K.M. Lin, L.Y.Li,M.F. Chen, Effect on structural, Optics & Laser Technology, 68, 41–47 (2015).
- [13] S.O. Elhamali, W.M. Cranton, N. Kalfagiannis, X. Hou, R. Ranson,D.C. Koutsogeorgis, Optics and Lasersin Engineering, 80, 45–51 (2016).
- [14] S. Halder, U. Boettger, T. Schneller, R. Waser, O. Baldus, P. Jacobs, M. Wehner, Mater. Sci. Eng. B, 133, 235–240 (2006).
- [15] A. Queralto, A. Perez Del Pino, M. De La Mata, J. Arbil, M. Tristany, A. Gomez,X. Obradors and T. Puig, Appl. Phys. Lett., 106, 262903 (2015).
- [16] M.G. Kang, K. H. Cho, S. M. Oh, Y.H. Do, C.Y. Kang, S. Kim, S.J. Yoon, Current Applied Physics, 11, S66-S69 (2011).
- [17] M.G. Kang, K.H. Cho, Y.H. Do, Y.J. Lee, S. Nahm, S.J. Yoon and C.Y.Kang, Appl. Phys. Lett., 101,242910 (2012).
- [18] A. Queraltóa, A. P. del Pino, M. de la Mata, M. Tristany, X. Obradors, T. Puig,

- S.T. McKinstry, Ceramics International, 42,4039–4047 (2016).
- [19] X.M. Lu, J.S. Zhu, W.S. Hu, Z.G. Liu and Y.N. Wang, Appl. Phys. Lett., 66, 2481-2483 (1995).
- [20] S.C. Lai, H.T. Lue, K.Y. Hsieh, S.L. Lung, R. Liu. T.B. Wu and P.P Donohue and P. Rumsby, J. Appl. Phys., 96, 2779-2784 (2004).
- [21] K. Kim and S. Lee, J. App. Phys. 100, 051604 (2006).
- [22] P. Muralt, Piezoelectric thin films for MEMS, Integr. Ferroelctr. 17, 297-307(1997).
- [23] G.K. Fedder, R.T. Howe, T.J. King Liu and E.P. Quevy, Technologies for co fabricating MEMS and electronics, Proc. IEEE, 96, 306-322 (2008).
- [24] R.R. Tummala, IEEE Trans. Adv. Packag. 27, 241-249 (2004).
- [25] J.U. Knickerbocker, P.S. Andry, L.P. Buchwalter, A. Deutsch, R.R. Horton, K.A. Jenkins, Y.H. Kwark, G. McVicker, C.S. Patel, R.J. Polastre, C. Schuster, S.R. McKnight, E.J. Sprogis, B. Dang, IBM J. Res. Dev. 49, 4-5 (2005).
- [26] R.R. Tummala, M. Swaminathan, M.M. Tentzeris, J. Laskar, G.K. Chang, S. Sitaraman, D. Keezer, D. Guidotti, Z.R. Huang, K. Lim, L.X. Wan, IEEE Trans. Adv. Packag. 27,250-267 (2004).
- [27] Jyh-Liang Wang, Yi-Sheng Lai, Sz-Chian Liou, Bi-Shiou Chiou, Chueh-Kuei Jan, and Huang-Chung Cheng, Journal of Vacuum Science & Technology B 26, 41 (2008).
- [28] Min-Gyu Kang, Kwang-Hwan Cho, Young Ho Do, Young-Jin Lee, Sahn Nahm, Appl. Phys. Lett. 101, 242910 (2012).
- [29] X. M. Lu, J. S. Zhu, W. S. Hu, Z. G. Liu, and Y. N. Wang, Applied Physics Letters 66, 2481 (1995).
- [30] J. Pundareekam Goud, S Ramakanth, Andrews Joseph, K. Sandeep, G L N Rao, and K. C. James Raju, Thin Solid Films 626, 126–130 (2017).
- [31] J. Pundareekam Goud, Mahmoud S. Alkathy, Kongbrailatpam Sandeep, S Ramakanth and K. C. James Raju, Journal of Materials Science: Materials in Electronics, 29,15973–15982 (2018).
- [32] J. H. Chen, C. L. Lia, K. Urban, & C. L. Chen, Applied physics letters, 81(7), 1291-1293 (2002).
- [33] H. J. Gao, C. L. Chen, B. Rafferty, S. J. Pennycook, G. P. Luo, and C. W. Chu, Appl. Phys. Lett. 75, 2542 (1999).

- [34] Z. Huang, Q. Zhang, and R. W. Whatmore, Journal of Applied Physics 85, 7355 (1999).
- [35] Adarsh Rajashekhar, Susan Trolier-McKinstry, Pulsed-Laser Crystallization of Ferroelectric/Piezoelectric Oxide Thin Films, Thesis, Pennsylvania State University, May 2017.
- [36] Zhang, H. et al. J. Eur. Ceram. Soc. (2020).
- [37] Y.H. Cheng, X.L. Qiao , J.G. Chen , Y.P. Wu , C.S. Xie , Y.Q. Wang , D.S. Xu ,S.B. Mo, Y.B. Sund, Surface and Coatings Technology 160, 269–276 (2002).
- [38] J. P. Zhao, Z. Y. Chen, T. Yano, T. Ooie, M. Yoneda, and J. Sakakibara, Journal of Applied Physics 89, 1634 (2001).
- [39] Yu. I. Yuzyuk, Phys. Solid Stat. **54**, 1026 (2012).
- [40] R. Naik et.al, Phys. Rev. B, **61**, 11367 (2000).
- [41] Q. Zhang, J. Zhai, L. Kong, X. Yao, J. Appl. Phys. 112, 124112 (2012).
- [42] L.Z. Cao, B.L. Cheng, S.Y. Wang, W.Y. Fu, S. Ding, Z.H. Sun, H.T. Yuan, Y.L. Zhou, Z.H. Chen, G.Z. Yang, J. Phys. Appl. Phys. 39, 2819 (2006).
- [43] S.Y. Wang, B.L. Cheng, C. Wang, S.Y. Dai, K.J. Jin, Y.L. Zhou, H.B. Lu, Z.H. Chen, G.Z. Yang, J. Appl. Phys. 99, 013504 (2006).
- [44] R. Swanepoel, J. Phys. [E]. **16**, 1214 (1983).
- [45] J.C. Tauc, F. Abeles., Optical properties of solids, North-Holland, Amsterdam, 1972.
- [46] H.-Y. Tian, W.G. Luo, A.L. Ding, J. Choi, C. Lee, K. No, Thin Solid Films. **408**, 200–205 (2002).
- [47] S. Ramakanth and K. C. James Raju, Journal of Applied Physics 115, 173507 (2014).
- [48] K. Sandeep, J.P. Goud, K.C.J. Raju, IEEE. (2016). https://doi.org/10.1109/ISAF.2016.7578099.
- [49] S. Tappe, U. Böttger, R. Waser, Appl. Phys. Lett. 85, 624–626 (2004).
- [50] S. Sandeep, J.P. Goud, K.C. James Raju, Appl. Phys. Lett. 111, 012901 (2017).
- [51] D. V. Sridhara Rao, K. Muraleedharan, and C. J. Humphreys, Microscopy: Science, Technology, Applications and Education, 2, p.1232.(2010).
- [52] S. Kumari, N. Ortega, D.K. Pradhan, A. Kumar, J.F. Scott, R.S. Katiyar,J. Appl. Phys. 118, 184103 (2015).

Chapter 6

Full depth crystallization of BST with laser annealing of layers at 300°C

6.1. Introduction

Heating with laser can be localized to the surface layer, which reduces the film-substrate interfacial interaction that happens generally at a higher temperature, which could result in a better film substrate interface. This can also result in crystallized films over substrates that cannot withstand higher temperatures. The Ba_{0.6}Sr_{0.4}TiO₃ thin films have been crystallized partially at 300°C by Kang et al. [1-3] using excimer laser annealing (ELA) exhibiting a single perovskite phase and high dielectric constant of 143 at a frequency of 1MHz the low dielectric loss of 0.028 and low leakage current density of 0.9 mA/cm². There are several issues involved with the laser annealing of BST and other ferroelectric thin films. The process of Laser annealing is affected by the film thickness. Lu et al. [4] crystallized a 600 nm PZT thin films up to 120 nm thickness by using a KrF excimer laser (Fig. 6.1).

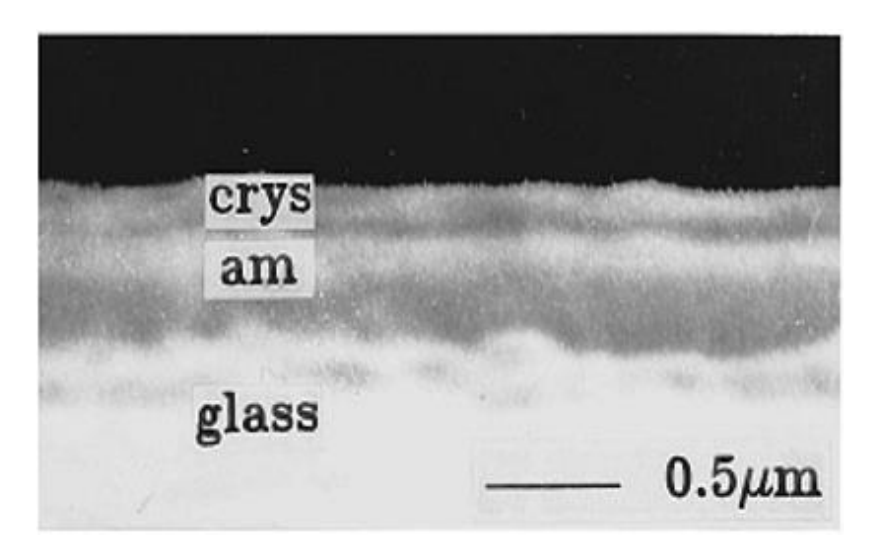


Fig. 6.1. Partial crystallization of PZT thin films (PZT 44/56 of ~600 nm, crystallized upto ~120 nm using Kr-F laser) (Lu et. al. [4]).

Haldar et al. [5] used a Kr-F excimer laser to crystallize BST thin films (thickness ~95 nm), which were deposited by a chemical solution deposition. Queralto et al. [3], fully crystallized 40 nm thick films of BST/LNO/SiO₂/Si with a Kr-F excimer laser (50 to 75

mJ/cm², substrate temperature ~500°C). However, 160 nm thick films, shows the crystallization only up to 70 nm after 12,000 pulses. The bottom portion of the film near to the substrate is amorphous in nature as the substrate is at RT and there is heat gradient from top surface due to the low thermal conductivity of amorphous BST [3]. Fig. 6.1 suggest that laser annealed thin films are partially crystalline. The diagrammatic representation of the partially crystalline films is shown in fig. 6.2.

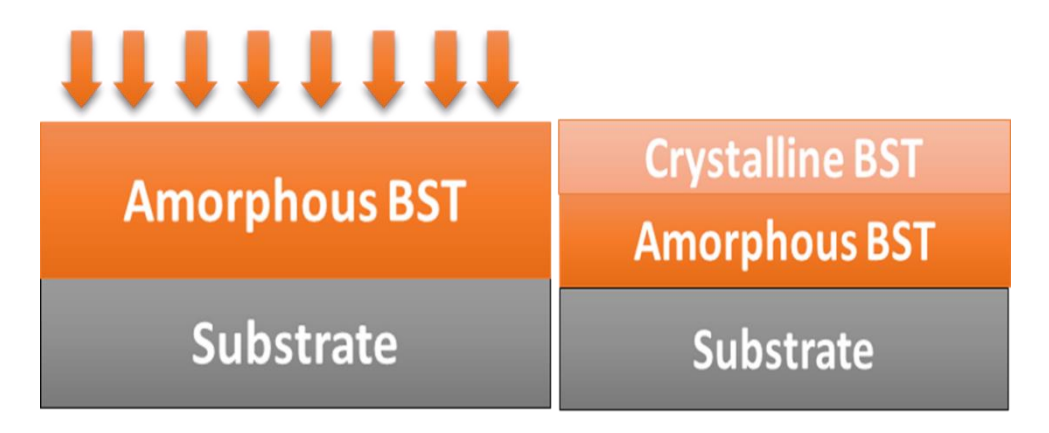


Fig. 6.2. Schematic of partial crystallization of BST thin films.

6.1.1 Laser annealing: Full Depth crystallization

Laser annealing offers top-down crystallization due to high temperature at the surface. Nucleation from the substrate can be achieved by

- Selecting a suitable substrate with lattice matching or
- Using a seed layer or
- Heating a substrate to a sufficient temperature which can provide the nucleation energy at the substrate-film interface.

Full depth crystallization of the thin films can be achieved by

(1) Increasing the dwell time of the laser pulses by extended-pulse laser annealing (Pulse width of Kr-F excimer laser pulses was extended from 25 to 374 ns) by Lai et al [6].

(2) In situ annealing, in which two laser sources can be used, one for the ablation and second for the laser annealing [7].

In the present chapter we have demonstrated a way to crystallize Ba_{0.5}Sr_{0.5}TiO₃ (BST5) thin films at lower temperatures using excimer laser annealing technique by KrF-248 nm. The BST5 thin films were crystallized layer-by-layer after deposition and subsequent laser annealing at 300°C. In this process 600 nm BST5 film was crystallized in which each layer consisting of 120 nm was deposited and subsequently crystallized by laser annealing with optimized laser fluence of 66 mJ/cm². The temperature of 300°C was kept constant for both the deposition and annealing processes. The phase formation and full vertical crystallization of BST5 thin films were confirmed by XRD patterns, Raman, UV-Vis-NIR, and cross-sectional TEM. The bandgap values show a systematic decrease after each laser annealing step. These, layer-by-layer deposited and laser annealed BST5 thin films showed a microwave tunability of 34% at 1GHz by circular patch capacitor method, which is close to the tunability shown by conventionally deposited BST5 films (at 700°C) and therefore it can be used for fabricating ferroelectric thin film based tunable devices like microwave varactors and resonators at low temperatures.

6.2. Experimental details

6.2.1 Deposition and Laser Annealing of Ba_{0.5}Sr_{0.5}TiO₃ thin films

The BST5 films were deposited on amorphous fused silica and platinized silicon Pt/Si (111) substrates by a pulsed laser deposition (PLD) system. The initial vacuum of 5×10^{-6} mbar is created by backing and Turbo pump in the chamber. The film deposition temperature was maintained at 300° C.

Table 6.1: The conditions of films grown by layer-by-layer deposition and subsequent annealing process at the same temperature (300°C).

BST5	Deposit	ion conditions			Annealing conditions			
thin films	Temp.	Rep. Rate (Hz)	Energy (J/cm ²)	No. of pulses	Temp (°C)	Rep. Rate (Hz)	Energy (mJ/cm ²)	No. of pulses
1- layer	300	5	2	2000	300	10	66	2000
2- layer	300	5	2	2000	300	10	66	2000
3-layer	300	5	2	2000	300	10	66	2000
4-layer	300	5	2	2000	300	10	66	2000
5-layer	300	5	2	2000	300	10	66	2000

In the presence of oxygen, in-situ annealing was carried out for 30 min after deposition. The thickness of the BST5 thin films for each layer is around 120 nm. Deposition and Laser annealing of BST5 thin films have been done in the presence of oxygen working pressure of 8×10^{-3} mbar.

Table 6.2: Sample codes used in this chapter.

Sample code	Description of sample
BST5	Barium Strontium Titanate (Ba _{0.5} Sr _{0.5} TiO ₃)
ADF 300 FS	As deposited films at 300°C on fused silica
ADF 700 FS	As deposited films at 700°C on fused silica
ADF 300 PS	As deposited films at 300°C on platinized silicon
ADF 700 PS	As deposited films at 700°C on platinized silicon
LLD 300 FS	Layer-by-layer deposited and laser annealed. Both at 300°C. Substrate fused silica
LLD 300 PS	Layer-by-layer deposited and laser annealed. Both at 300°C on platinized silicon
ADF 300 PCS	As deposited films at 300°C on platinum coated silicon
ADF 700 PCS	As deposited films at 700°C on platinum coated silicon
LLD 300 PCS	Layer-by-layer deposited and laser annealed. Both at 300°C on platinum coated silicon

6.3. Phase and structural properties

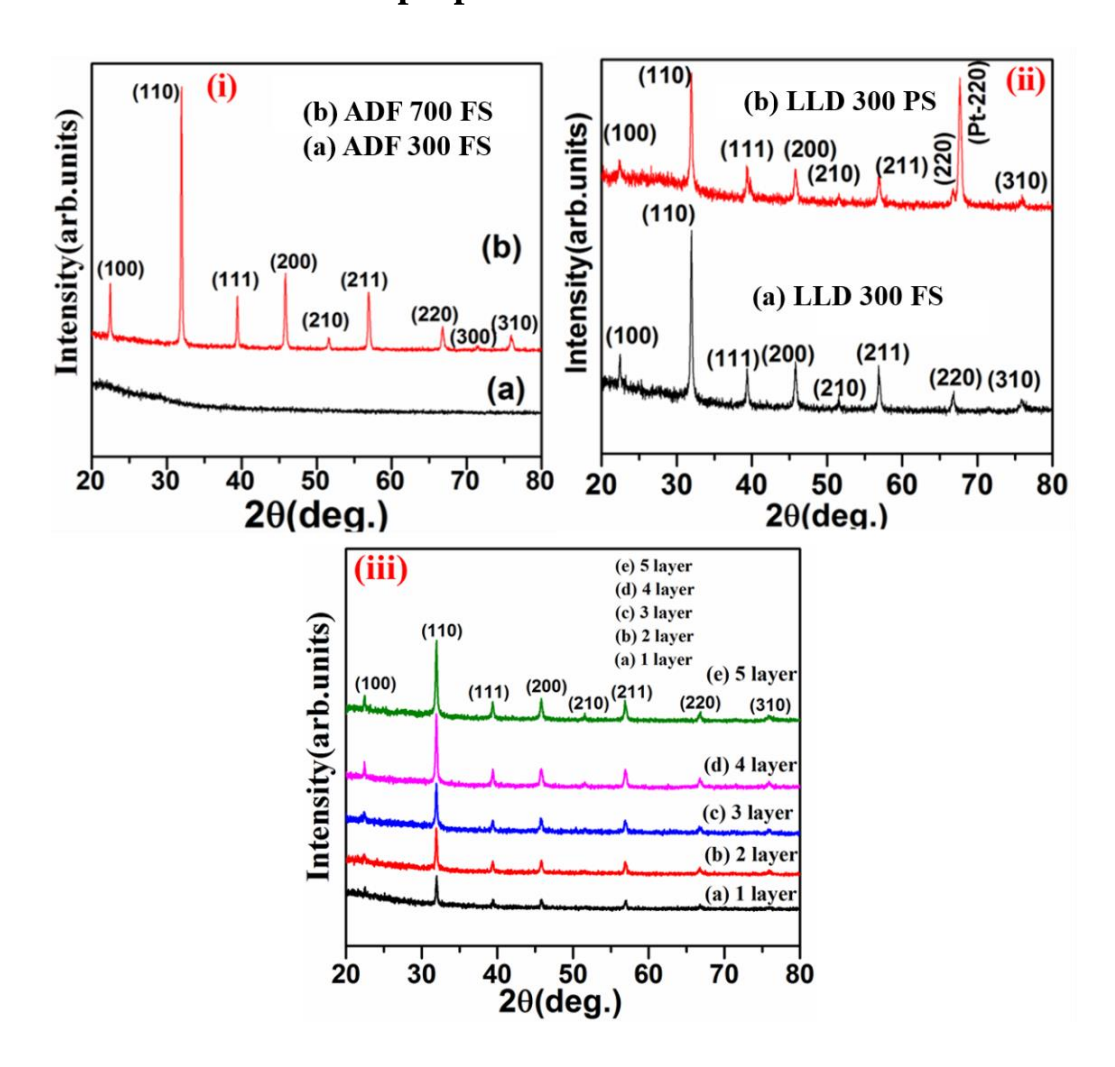


Fig. 6.3. XRD patterns of BST5 thin films (i): (a) ADF 300 FS (b) ADF 700 FS, 6.3(ii): (a) LLD 300 FS and (b) LLD 300 PS 6.3(iii): XRD of each layer deposited on fused silica substrate.

The structural and phase studies of these films were carried out by X-ray diffraction (GI-XRD-Bruker D8 Discover). The fig. 6.3 (i) and (ii) shows XRD pattern of ADF 300 FS, ADF 700 FS as well as LLD 300 FS. The XRD of BST5 thin films ADF 700 FS exhibit polycrystalline nature and films of ADF 300 FS shows amorphous nature, as shown in fig. 6.3 (i). The fig. 6.3 (ii) shows LLD 300 FS and LLD 300 PS. The XRD pattern of ADF 700 FS, as well as LLD 300 FS are identical to that of standard data with JCPDS card no (file # 39-1395) of a cubic structure. Fig 6.3 (iii) shows the XRD pattern of each layer on a fused silica substrate, and after the deposition of each layer followed

by a laser annealing process, the XRD peaks have strengthened with increased intensity, and bandgap got steadily lowered which supports the increase in crystallinity. Therefore, it is clear that the films of LLD 300 FS are crystallized.

6.4 TEM Analysis

The preliminary observation of Bright Field images of (ADF 300 FS), (ADF 700 FS) and (LLD 300 FS) are carried out using TEM. The TEM images (Figs. 6.4 (ii) (a)-(iii) (a)) shows that the crystallites are irregular in shape. The HRTEM images were used to calculate the d-spacing and respective planes are assigned to that. (Figs. 6.4 (ii) (c)-(iii) (c)). Most of the crystallites are grown in (110) direction with d spacing in the range of 2.70-2.76Å. The SAED patterns (Figs.6.4 (i)(b))-(iii)(b)) of films, here (ADF 300 FS) show amorphous nature and (ADF 700 FS) and (LLD 300 FS) shows the polycrystalline nature of films. The ring diameters in SAED patterns are used to calculate the d spacing and they are matched with respective standard JCPDS file (file # 39-1395) supporting localized BST5 crystalline growth in the films that are (LLD 300 FS). Similar TEM microstructural evolution of ferroelectric films, under conventional and laser annealing are reported in literature [8-11]. The bright field images of (LLD 300 FS) shows grain formation. The crystal structure of the samples was examined by HRTEM and SAED measurements. It shows that the LLD 300 FS films consists of nano-size grains with boundaries of average size of about 7-10 nm.

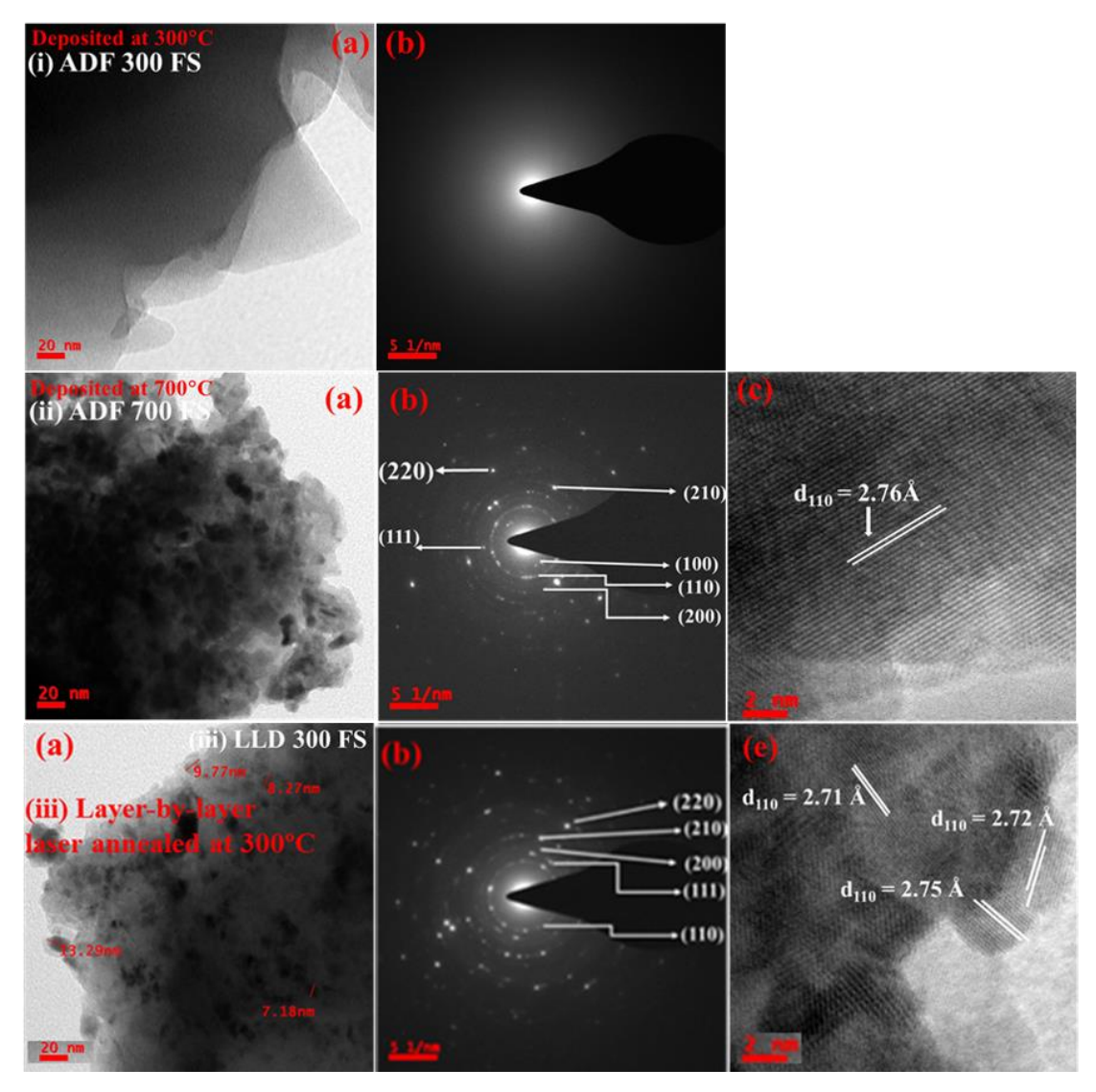


Fig. 6.4. The images in columns (a) (b) and (c) shows the TEM Bright field, selected area diffraction (SAED) and HRTEM patterns of BST5 thin films respectively.

(i) ADF 300 FS (ii) ADF 700 FS and (iii) LLD 300 FS.

Cross-Sectional TEM

The cross-sectional TEM images of as-deposited films at 700°C (ADF 700 PCS) and multilayered laser annealed BST5 thin films prepared at 300°C (LLD 300 PCS) on platinum coated silicon substrates are shown in fig. 6.5. The preliminary observation in cross-sectional TEM Bright Field Images of ADF 700 PCS in fig. 6.5 (a, b) and LLD 300 PCS are shown in fig.6.5 (e, d). TEM BF images demonstrate conventional columnar crystallization. SAED pattern acquired from the region reconfirms the same as shown in

(Figs.6.5 (c)) and (f)). The SAED pattern also demonstrates individual layers of crystallization and confirms the polycrystalline nature of both films ADF 700 PCS and LLD 300 PCS films. The measured d- spacing values from SAED patterns matches with the d-spacing values in JCPDS card file (file # 39-1395) confirming the BST5 crystal structure of the films that are (LLD 300 FS) [8-11].

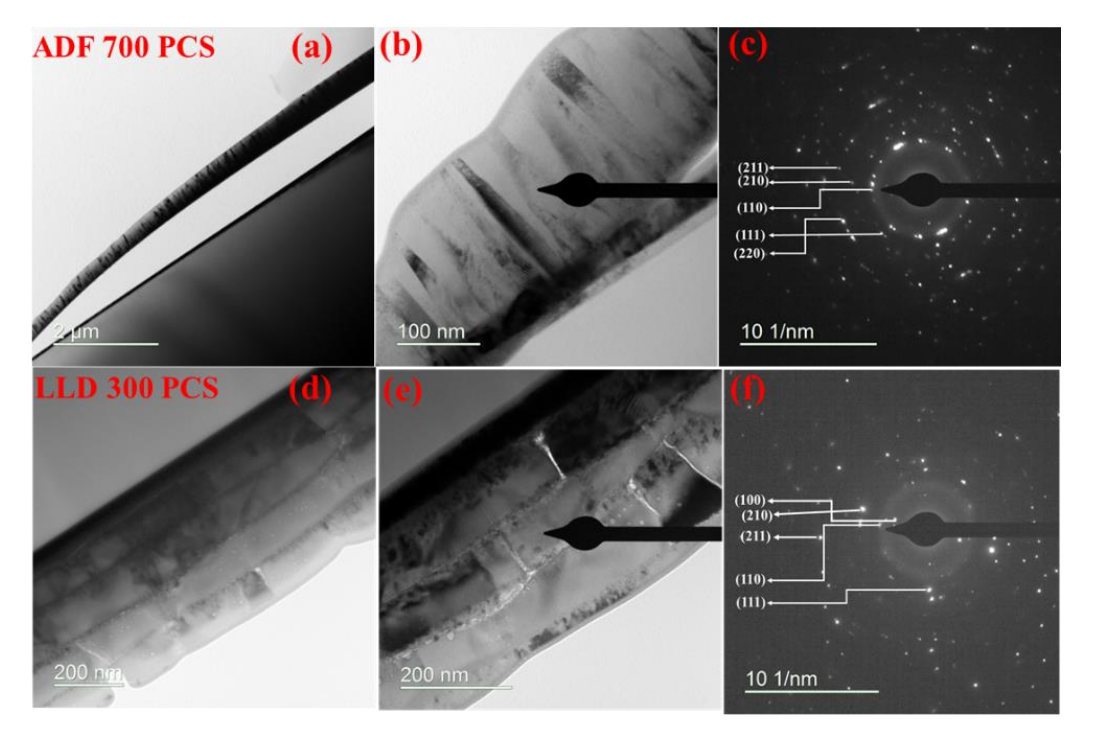


Fig.6.5. Shows cross-sectional TEM Images of BST5 thin films as-deposited (ADF 700 PCS) and multilayered deposited and laser annealed at 300°C (LLD 300 PCS) on platinum coated silicon substrates.

6.5 Microstructure Properties

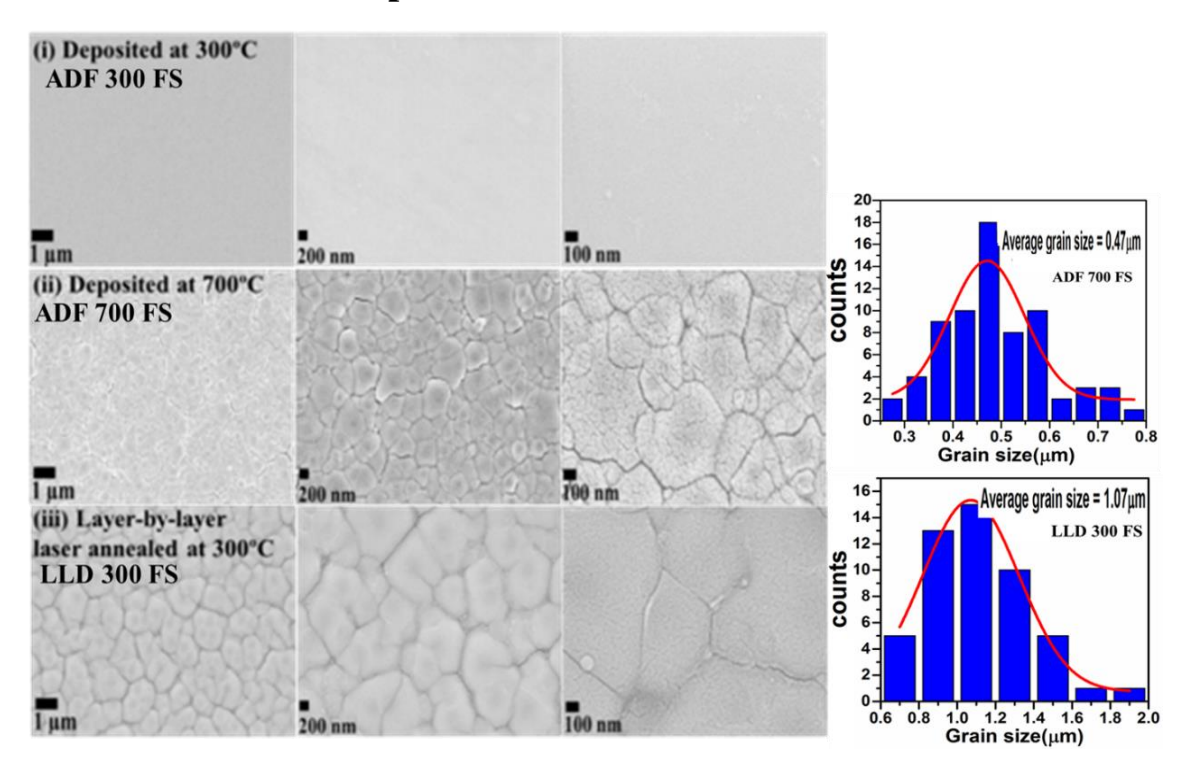


Fig.6.6. FESEM images of BST5 thin films in different magnifications (i) As deposited at 300°C (ADF 300 FS) (ii) As deposited at 700°C (ADF 700 FS) and (iii) Layer-by-layer deposited and annealed both at 300°C (LLD 300 FS) on fused silica.

The microstructure of the samples are observed by FESEM. As deposited BST5 films are microstructurally smooth, thereby indicative of amorphous nature, are shown in fig. 6.6(i) at different magnification. Layered films confirm that each grain is an agglomeration of small clusters. We focus our studies on these smaller grains microstructurally evolved in BST5 films (Fig.6.6). The grain clusters are crystallized and are irregular in shape, as observed in the FESEM micrographs shown in figs.6.6 (ii)-(iii). Similar microstructural evolution of ferroelectric films, like the present case study of BST5, are reported elsewhere [1, 5, 12-14]. The grain growth histograms are also another indication suggesting crystallization.

The microstructure of the ADF 700 FS and LLD 300 FS BST5 thin films were examined by FESEM images (Fig. 6.6) and they show dense films with clear grains

(smooth surfaced), which are suitable for the measurements of electrical properties. Large clusters (\approx 0.47 µm) were found; in the high temperature processed films, while laser annealed thin films have larger clusters of irregular shapes. These cluster dimensions of both ADF 700 FS and LLD 300 FS BST5 thin films were shown in histograms (Fig.6.6). Both these films are microstructurally alike in appearance (existence of nanometric grain), but only slightly different in terms of clustering. LLD 300 FS surface morphology is smoother with least void and cracks in between clusters, thereby qualitatively better for electrical measurements.

6.6. Optical properties

6.6.1 Raman analysis

Raman spectroscopy is known for its non-destructive structural characterization of various materials. Fig. 6.7 shows the Raman spectra recorded at room temperature for conventional 700°C deposited BST5 thin films. Plenty of literature highlighting the Raman phonon modes of the cubic BST5 phase, can be found elsewhere [15-21].

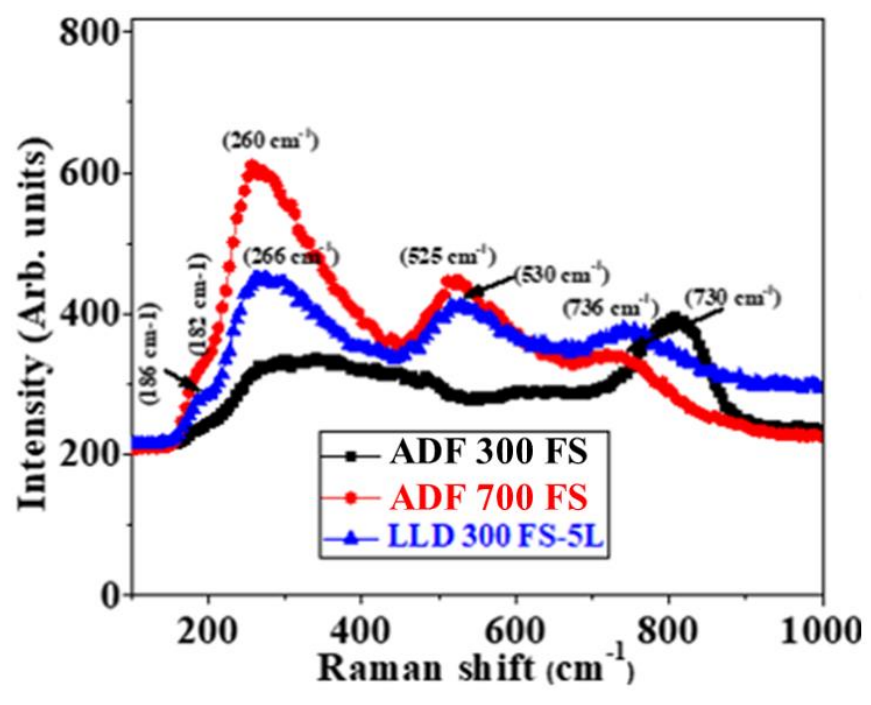


Fig. 6.7. Raman spectra of the BST5 thin films of ADF 300 FS, ADF 700 FS, and LLD 300 FS.

Raman spectra of layer-by-layer deposited and laser annealed at 300°C (LLD 300 FS) films are shown in fig. 6.7. The layered films show Raman modes at 186cm⁻¹, 266 cm⁻¹, 530 cm⁻¹ and 736 cm⁻¹ identical to that of ADF 700 FS films. Therefore, it was confirmed that LLD 300 FS films have become crystalline at 300°C in the cubic phase. The observed peaks (modes) at 182-186, 260-266, 525-530 and 730-736 cm⁻¹ are corresponding to E(TO₂), A₁(TO₂), A₁(TO₃) and A₁(LO₃) phonon modes, respectively [22]. It is interesting to note in fig. 6.7 that most of the Raman modes shifted towards lower wavenumber, in ADF 700 FS, which could be related to a distortion in the octahedral [23].

6.6.2 Bandgap studies

The optical transmission spectra are measured in 190-2500 nm wavelength range for the PLD deposited films and are shown in fig. 6.8. From the transmission spectra it is clear that the films are transparent in the near-infrared and visible regions. The bandgap values were obtained from the Tauc plot for high absorptive region with sharp absorption around 300 nm for all films. It is observed that the transmission spectra edge of the BST5 films undergoes a stage-wise change to higher wavelength (red-shift) for each layer of laser crystallization. The computed bandgap values in table 6.3 are by Tauc relation [24-26].

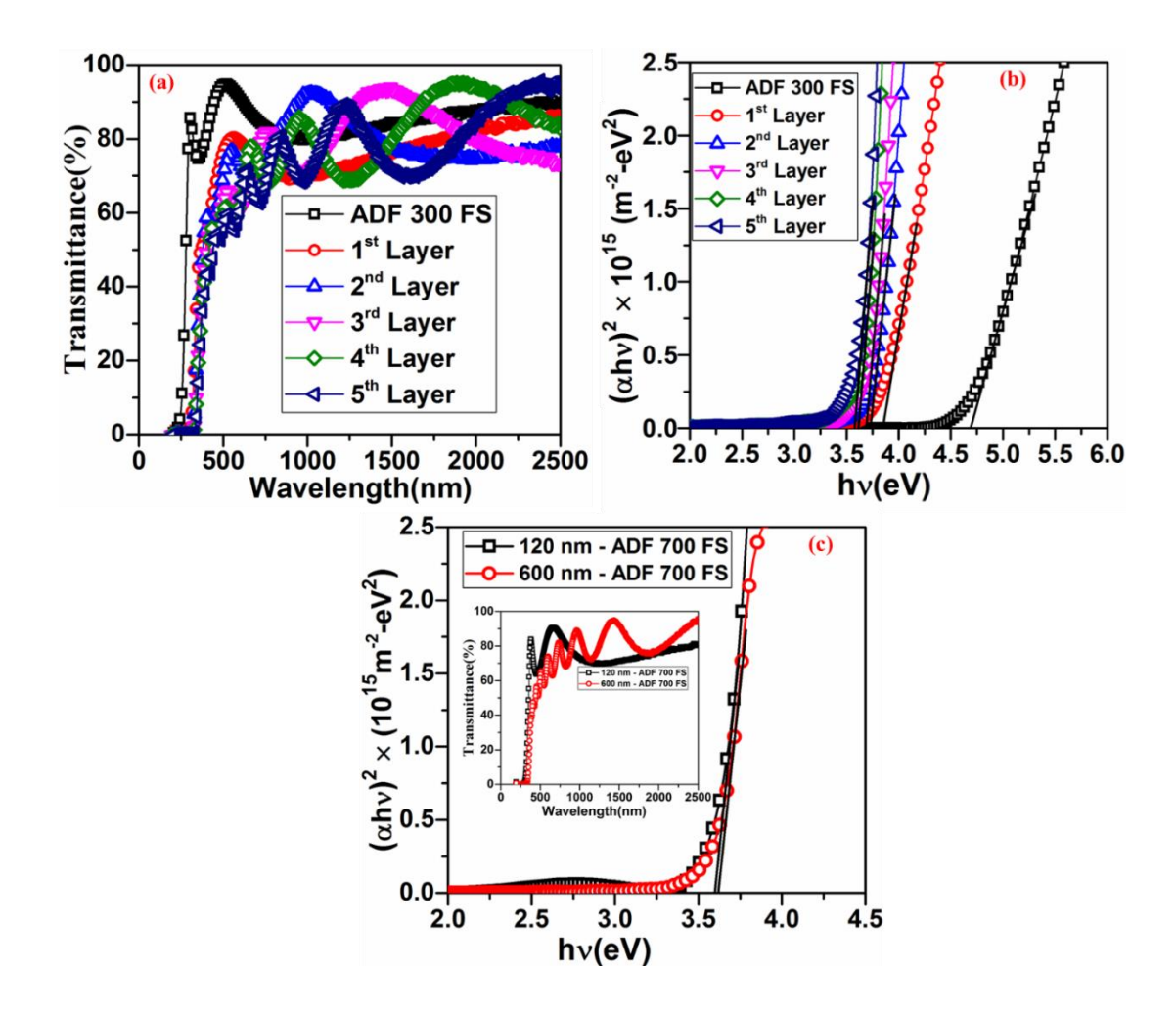


Fig. 6.8. Transmission spectra and $(\alpha hv)^2$ vs. hv plots of BST5 thin films of (a) ADF 300FS, (b) LLD 300 FS and (c) ADF 700 FS.

The bandgap values for BST5 thin films, which are laser annealed layer-by-layer, are listed in Table 6.3. The bandgap of the films decreases from 4.65 eV to 3.56 eV after layer-by-layer deposition and subsequent laser annealing, which also supports the crystallization of BST5 thin films at 300°C [24-26].

The highlight of this UV-Vis-NIR spectroscopic observation is that band-gap value of each layer after crystallization is steadily approaching the bandgap value of the ADF 700 FS film. This shows that the optimized process parameters used by us for crystallization are good enough to realize crystallization.

As crystallization occurs, the grain growth will take place whereas in the initial stages of crystallization, they will be in small size, and therefore it is evident that the smaller size particles show a higher bandgap, and it decreases as the particle size increases.

Table 6.3: Band gap values of layer-by-layer deposited and subsequent laser annealed BST5 thin films.

S. No	Sample codes	Band gap (eV)
1	ADF 300 FS	4.65
2	1-Layer1	3.85
3	2-Layer	3.75
4	3-Layer	3.7
5	4-Layer	3.62
6	5-Layer	3.56
7	ADF 700 FS	3.54

6.7. Microwave dielectric properties

Figure. 6.9 shows the schematic (cross-section and top view) of the varactor designed using the deposited films. It has the stacking configuration Au/BST/Pt/Si. A Circular Patch Capacitor (CPC) is fabricated on the films for microwave dielectric property measurements. The Au top electrode of 150 nm thickness was patterned employing photolithography.

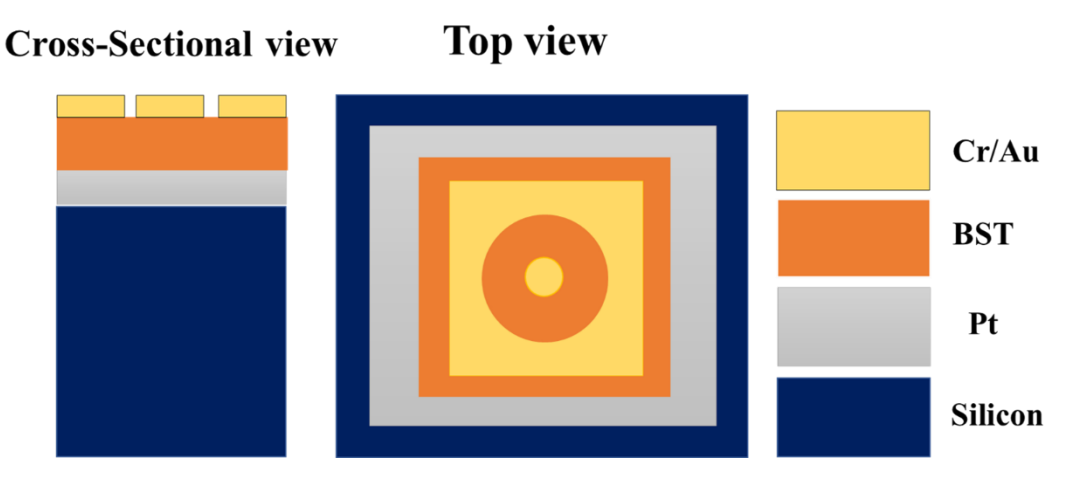


Fig. 6.9. Schematic (cross-section and top view) of the varactor using the BST5 film as the dielectric layer.

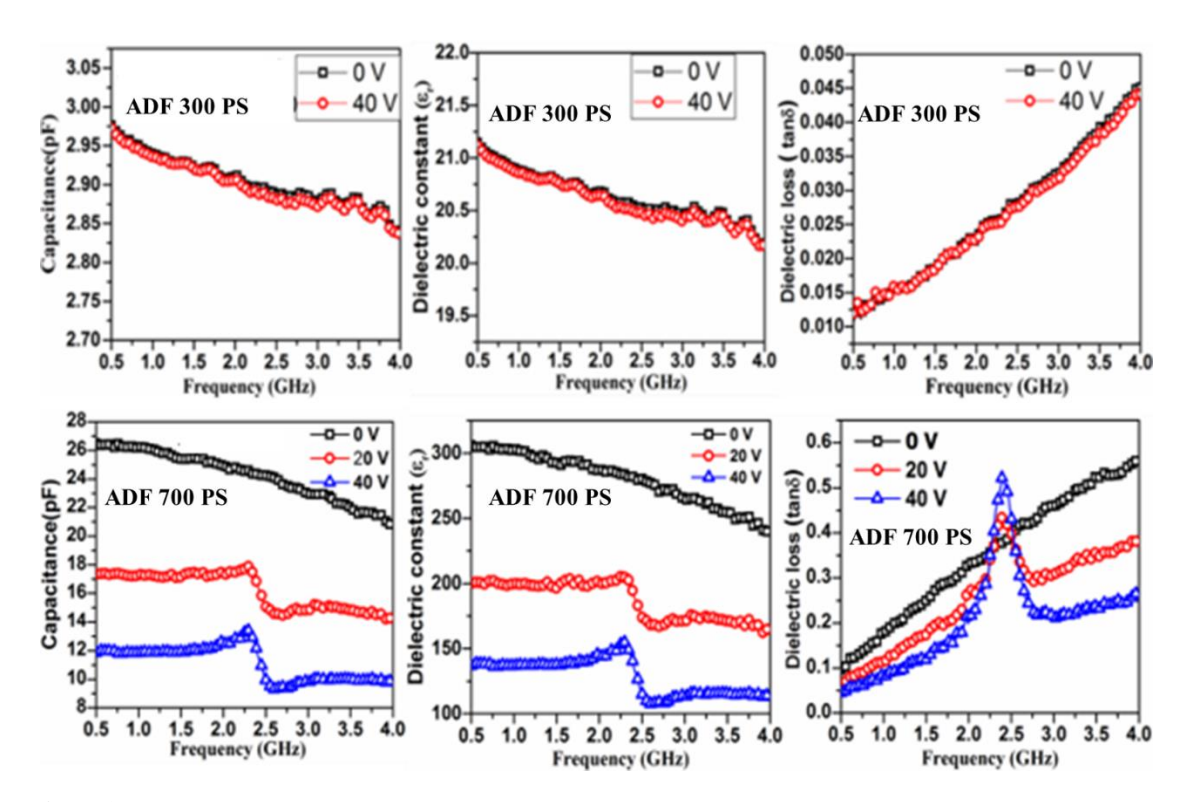


Fig.6.10. Capacitance, dielectric constant & dielectric loss of Ba_{0.5}Sr_{0.5}TiO₃ (BST5) thin-films of ADF 300 PS and ADF 700 PS on platinized silicon substrates.

Microwave dielectric properties of ADF 300 PS and ADF 700 PS BST5 thin films with the optimized deposition fluence of 2 J/cm² are shown in fig. 6.10. The BST5 ferroelectric thin film of thickness 600 nm, was deposited on platinized silicon (111) substrate by pulsed laser deposition (PLD) technique. A top electrode of gold with 150 nm thickness was deposited by RF sputtering and patterned using photolithography [27-30].

Microwave measurements in the frequency range of 0.5 GHz - 4 GHz using a vector network analyzer (Agilent E8361C network analyzer) and on-wafer probing setup are carried out for the layer-by-layer deposited and annealed films. The capacitance, dielectric constant and dielectric loss variation with frequency for these films are shown in fig. 6.11(a-c). The necessary biasing is provided by using a bias tee.

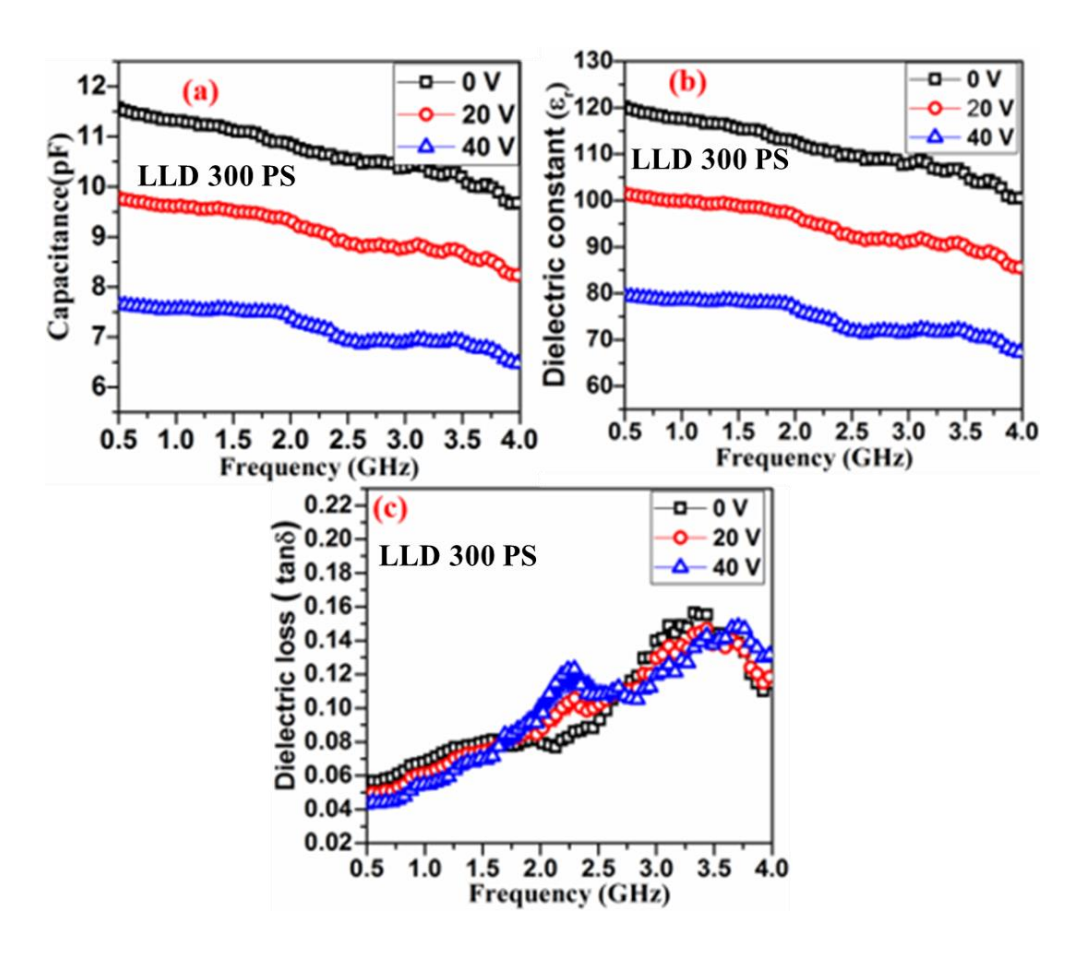


Fig.6.11. (a-c) Capacitance, dielectric constant & dielectric loss of BST5 thin films of LLD 300 PS.

The BST5 thin films have higher values of dielectric permittivity and their strong dependence on external DC electric field bias provides an additional feature called tunability defined as:

Tunability (%) =
$$\frac{C(0) - C(E)}{C(0)} \times 100$$
 (6.1)

where C (0) and C(E) are the dielectric capacitance values at zero and non-zero dc electric bias field respectively. Using equation (6.1), the microwave tunability is calculated at a frequency of 1GHz and is given in Table 6.4 for films deposited on platinized silicon substrates. The microwave tunability, dielectric constant and dielectric loss of 700°C

deposited film, 300°C deposited film (without annealing) and layer-by-layer deposited and laser annealed films are tabulated in Table 6.4.

Table 6.4 gives the microwave dielectric constant and loss tangent as well as tunability measured for different BST5 thin films. Conventionally deposited BST5 thin films at 700°C (ADF 700 PS) gives a tunability of 54% but no tunability response is observed in BST5 films deposited at 300°C (ADF 300 PS). The microwave tunability of layer-by-layer deposited films that are laser annealed at 300°C (LLD 300 PS) gives tunability of 34%, which is close to the conventionally deposited films grown at 700°C. From the above observation, it can be seen that LLD 300 PS can be used for fabricating ferroelectric thin film based tunable microwave devices like varactors and resonators at low temperatures, thereby making the processes compatible with polymers in flexible Electronics.

Table 6.4: Comparison of microwave dielectric properties of following BST5 films: ADF 300 PS, ADF 700 PS and LLD 300 PS.

BST5 thin film Sample codes	Microwave tunability (1 GHz)	Dielectric constant (ε _r)	Dielectric loss (tanδ)
(i) As-deposited	No response	23	0.09
film at 300°C			
(ADF 300 PS)			
(ii) As-deposited	54%	301	0.16
film at 700°C			
(conventional)			
(ADF 700 PS)			
(iii) Layer by layer	34%	118	0.06
deposited and laser			
annealed at 300°C			
(LLD 300 PS)			

In the present study, laser annealing of amorphous BST thin films has resulted in mixed microstructure, which results in the low dielectric loss with high permittivity and moderate tunability. The microstructure is a mixture of amorphous and crystalline regions as seen from the TEM micrographs. Therefore, we can expect influence from both the

phases in the properties as well as the influence of one on the other. Tunability being a ferroelectric property can be exhibited only by the crystalline phase. As the volume fraction of the crystalline phase increases the tunability should increase. Indeed, the same trend is being observed with no tunability for amorphous film and highest for in-situ thermally crystallized films and intermediate for the LLD processed films. Similarly, lowest value of dielectric constant is found with the amorphous films while the in-situ crystallized films gave the highest values with LLD process yielding in between results. Loss values follows a similar trend with LLD process yielding an unusually low value which makes this process very attractive for device applications. The intermediate result obtained for the LLD process agrees with the TEM based observations that the laser annealing process yields a partially crystalline process. Since crystallization is already observed, full crystallization should be possible with appropriate process optimizations. However even the partially crystalline samples exhibit microwave dielectric properties that are quite attractive for tunable microwave device applications.

As mentioned, the microstructure also plays a crucial role in the dielectric properties of these thin films. The FESEM surface observation of both ADF 700 PS and LLD 300 PS films presented earlier, suggest nano-grains clustering. It is reported that in case of paraelectric films an optimum cluster size, also affects their microwave tunability [31].

6.8. Electrical Properties

6.8.1 Leakage current studies for BST thin films deposited at high temperature

Understanding of leakage current behavior in thin films with the bias field is essential for device applications. Leakage currents were measured by a ferroelectric test module (TF1000 analyzer, aixACCT systems, Germany). The leakage current density (J) vs. electric field (*E*) characteristics of the BST5 thin film is shown in fig. 6.12. Leakage current study was carried out for the PLD-deposited BST5 thin films to understand how far the DC bias field excited dc conductivity would affect the microwave characteristics and operation of these films when used in tunable microwave device applications as well as to see the onset of electrical breakdown in these films. Leakage current density increases rapidly with a substantial increase in applied electric field (fig. 6.12) [1,5].

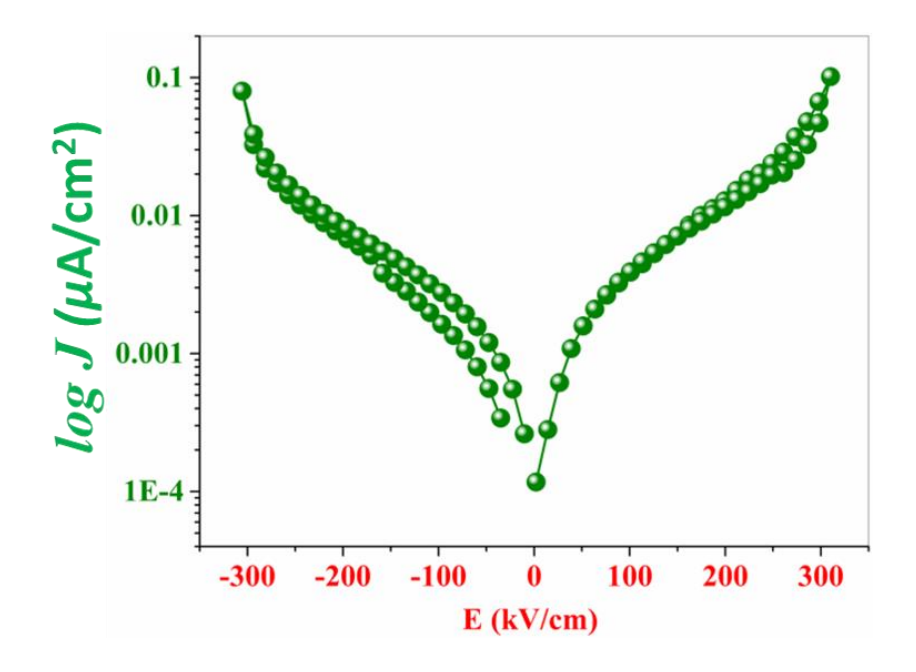


Fig. 6.12. The plot of leakage current density vs. electric field for the BST5 thin film ADF 700 PS.

The $\log(J)$ versus $\log(E)$ curve is shown in fig. 6.13 and based on the different slopes it exhibits, curve is divided into three distinct regions (I, II and III). In the region-I, the slope of the curve is 1.24 and the electric field of ~70 kV/cm and the leakage current follows the Ohmic law in this region. The slope value ≥ 2 in J-E curve indicates the contribution from space charge under high electric field and can be explained by the theory of space charge limited conduction (SCLC). The SCLC occurs when the injecting electron density at the cathodic interface per given time is larger than the density of electrons passing across from the cathode to anode. In region-II (from 70 to 220 kV/cm), the slope of the J-E curve has increased to 5.53 and further increase in electric field in region-III (220-315 kV/cm) results in the slope value of ~10.69. This indicates that SCLC gradually becomes dominant with increasing electric fields.

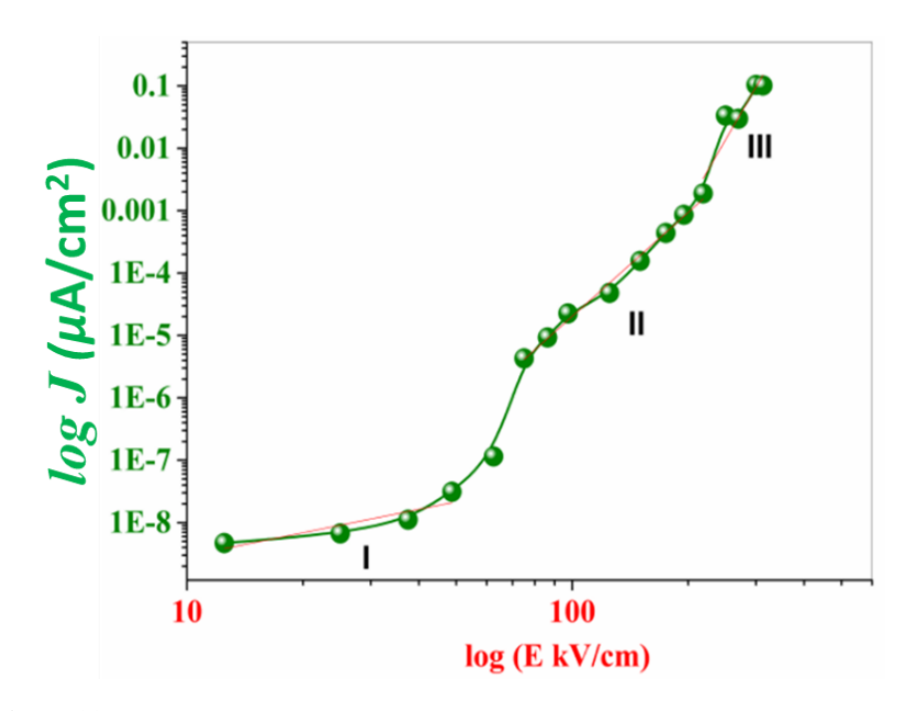


Fig. 6.13. The plot of log J vs. log E for the BST5 thin films ADF 700 PS.

6.8.2 Leakage current studies on laser annealed films

The *J-E* characteristics of the as deposited films (ADF 300 PS) is as shown in fig. 6.14 (i) (a) and Laser annealing (LLD 300 PS) BST5 thin films are shown in fig. 6.14 (ii) (a) and (b). The increase in electric field leads to an increase of leakage current density values.

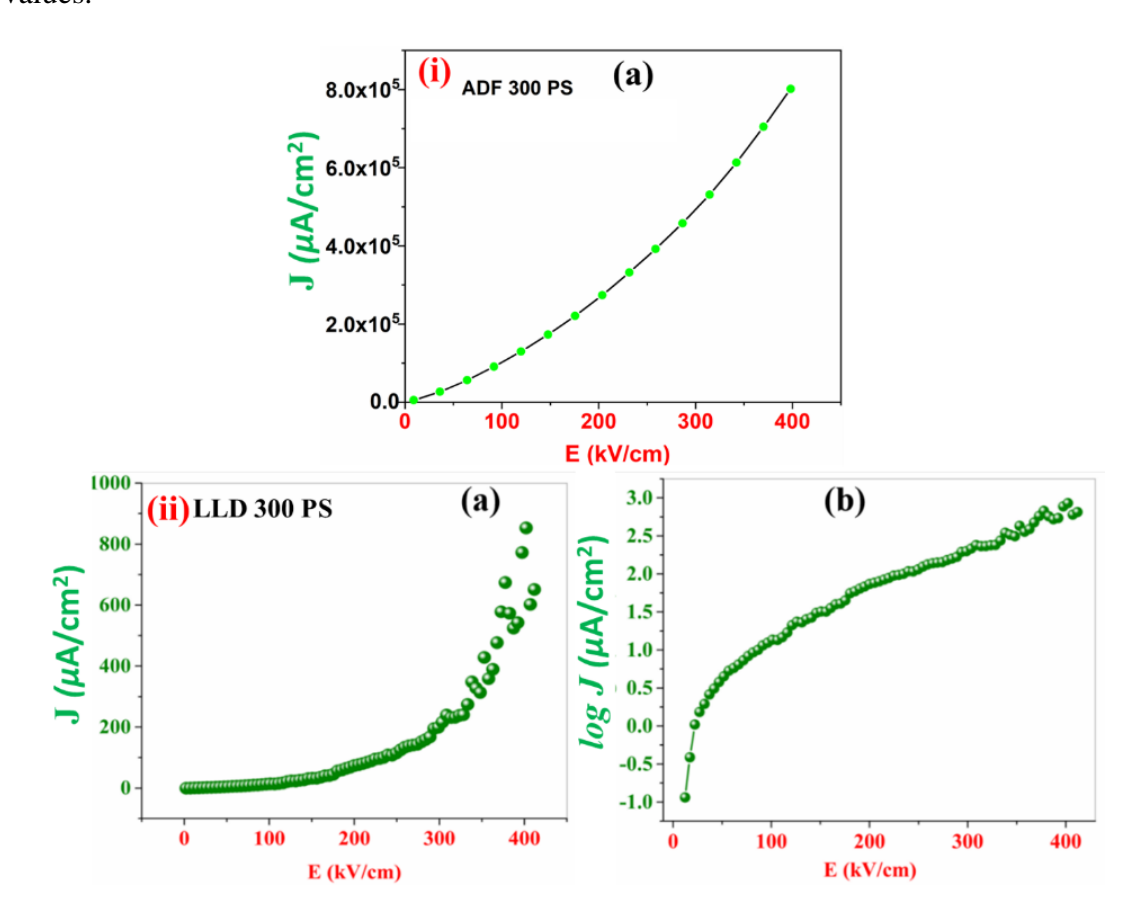


Fig. 6.14.(i) J vs. E of ADF 300 PS and (ii) (a) J vs. E (b) log J vs. E curve for Layer-by-layer deposited and laser annealed BST5 thin films (LLD 300 PS).

The fig. 6.15 shows the variation of $\log(J)$ with $\log(E)$. The SCLC theory is used to explain the three different regions of the plots [1,5,34]. The slope of the curve was found to be 1.18 to ~3, which shows that most of the conduction is only of Ohmic type. The comparison between laser annealed thin films and high temperature deposited BST thin films is given in Table 6.5. The laser annealed thin films show very low leakage current, which is the attractive for device fabrication.

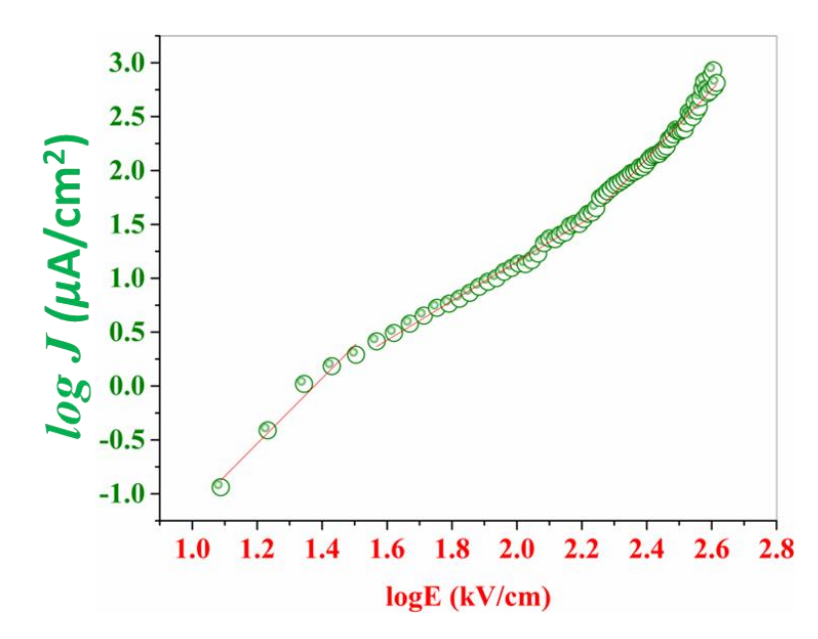


Fig. 6.15. Log J vs. log E curve for BST5 thin films LLD 300 PS.

Table 6.5: Leakage current study for layer-by-layer laser annealed and high temperature deposited BST5 crystalline thin films.

E	Films deposited	Films deposited	Layer by layer
(KV/cm)	at 300°C	at 700°C	laser annealed
	$J \left[\mu A/cm^2 \right]$	$J \left[\mu A/cm^2 \right]$	films (deposition
	(ADF 300 PS)	(ADF 700 PS)	& annealing at
			300°C)
			$J [\mu A/cm^2] (LLD)$
			300 PS)
100	1.03×10^5	3.890×10^3	1.4×10^{1}
200	2.7×10 ⁵	1.2820×10^4	7.4×10^{1}
300	4.9×10 ⁵	6.6860×10^4	2.16×10^2
310	5.2×10 ⁵	1.01570×10^5	2.40×10^{2}
400	8×10 ⁵	Shorted	8.50×10^2

(J-E plot of ADF 300 PS (amorphous film) is shown fig. 6.14 (i) (a)).

A comparison of the leakage current measurements data of the three samples (ADF 300 PS, LLD 300 PS, and ADF 700 PS respectively) investigated is tabulated in table 6.5. Clearly, the processed LLD 300 PS is of 3 orders lower in magnitude of leakage current than the amorphous (ADF 300 PS as shown fig. 6.14 (i) (a), and almost 2 orders lower than conventional processed ADF 700 PS respectively. It is a crucial advancement as lower

leakage current is an essential figure of merit for a tunable microwave device. This laser-based process has opened a new way to overcome the age-old problem buffeting the oxide films in similar applications. Tunable microwave devices apply a high electric field across the film to achieve dielectric tuning. The same can excite a leakage current, which got all the potential to destroy the device through Joule heating or to limit its life. In the microwave dielectric loss exhibited by these films, (Fig.6.4) it was pointed out that the loss values exhibited by the laser processed films are even lower than that of the amorphous films. Now the leakage current reduction points to the cause of it as a reduction in leakage current will reduce the charge carrier induced microwave loss mechanisms.

This observation got an enormous additional technological importance because a capacitor plays the crucial role in CMOS devices and with shrinking device dimensions, it is the leakage current of the capacitor that limits its operation. Efforts are going on to circumvent this problem with different compositions including with dielectrics that give high dielectric constant as they give same capacitance with larger film thickness. But they also gets limited by their leakage current performance, with further miniaturization. This result shows that there is an alternate way to solve the problem of leakage current by this kind of a laser-based processing that results in a mixed matrix of crystalline and amorphous phases. Since conduction in oxide thin films are dominated by the defect structure, a reduced leakage current indicates a structure where defects are healed. The laser process that induce lattice mending must have achieved defect compensation also. Also, the presence of an amorphous phase in between crystallites must be blocking the charge carriers or contributing to compensate the defects.

6.9 High overtone bulk acoustic resonator (HBAR) response

The on-wafer probe station was used for the HBAR microwave measurements using a 250 µm pitched Ground-Signal-Ground probe and it is calibrated with standard open and short loads. For different dc bias voltages, the S-parameter (S_{11}) was measured for a range of frequencies. From the measured S₁₁(reflection coefficient) the values of complex input impedance are obtained and plotted with frequency (500 MHz - 3 GHz). These plots are shown in fig. 6.16 and in fig. 6.17 with and without dc bias, for the BST5 as-deposited film at 700°C (ADF 700 PCS) and layer-by-layer deposited and subsequent laser annealed films on platinum coated silicon (LLD 300 PCS) films respectively. It is clear from these figures that the LLD 300 PCS is responding to the bias applied and acts like a piezoelectric thin film due to electrostriction as in the case of ADF 700 PCS. This induced piezoelectric response (exhibited only in crystalline state) of the LLD 300 PCS film translates as resonances in the frequency spectrum, and multiple resonance peaks occur due to creation of standing waves inside the double side polished silicon substrate. For both the cases, if the narrow band is taken into consideration i.e. Figure 6.16 (b and d) and 6.17 (b and d), the acoustic velocity of the substrate can be calculated. It is interesting to note that for the case of the HBAR, the spacing between adjacent resonant peak(Δf) is dependent only on the acoustic properties and thickness of the substrate; the spacing between resonant peaks for both samples ADF 700 PCS and LLD 300 PCS (silicon substrate thickness, t_{substrate} ~500 µm) is found to be around 9.63 MHz and by using the relation $V=2\times t_{\text{substrate}}\times\Delta f$, the acoustic velocity of the silicon substrate is calculated to be around 9400 m/s [27,33]. From these results it is demonstrate that, laser annealing can be used for designing acoustic resonators like; film bulk acoustic resonator, solidly mounted resonators etc. Secondly, presented 300°C laser annealing induced crystallization can be extended to flexible polymer substrates which had vast application in designing passive RF devices like filters

and even sensors of various types by giving an added advantage of tunability and flexibility.

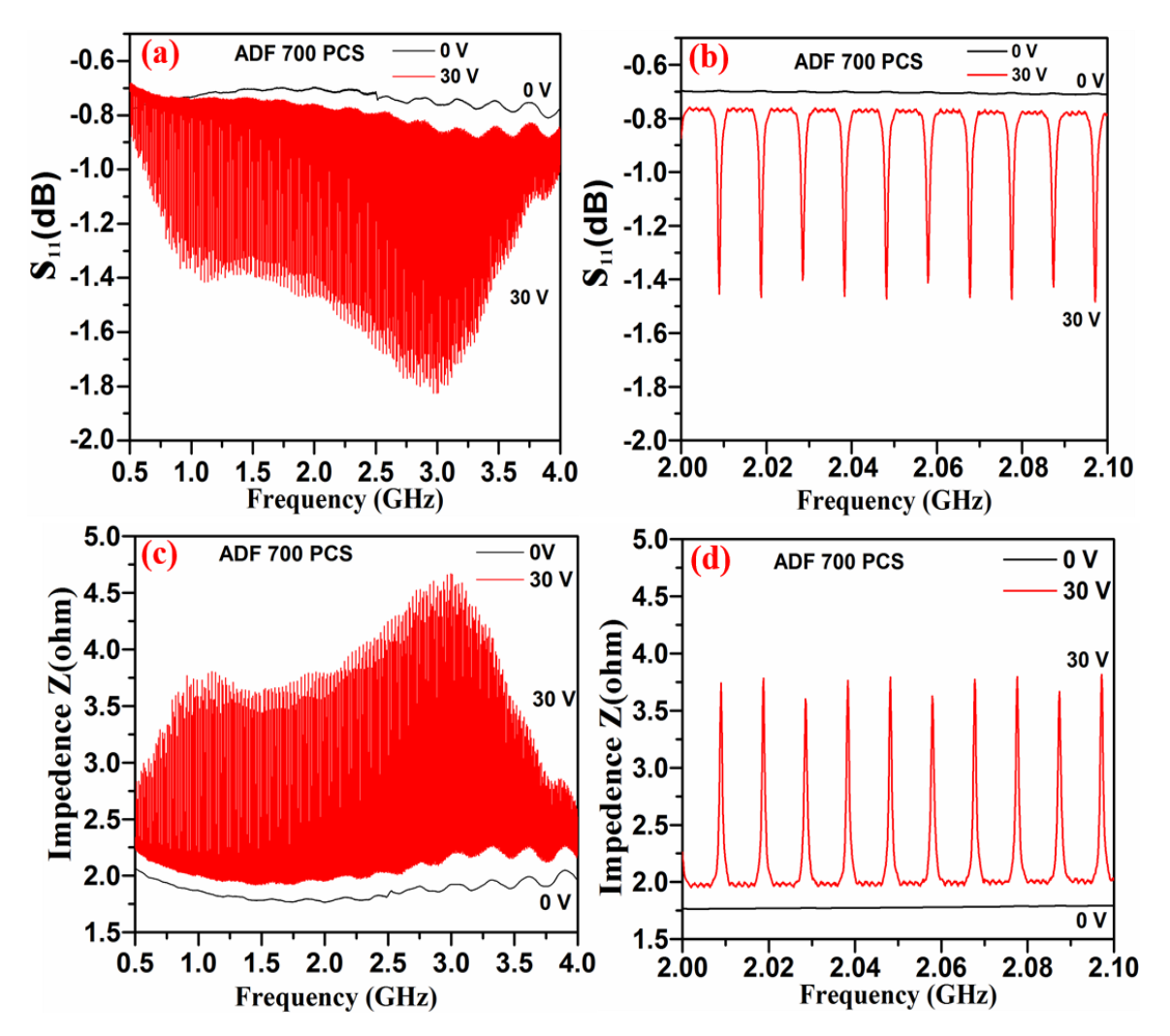


Fig.6.16 (a) Measured HBAR frequency spectrum for ADF 700 PCS with and without biasing, S₁₁, (c) Calculated electric impedance in broad band range of 500 MHz – 4 GHz. (b) and (d) HBAR response with and without dc bias in the 2 GHz–2.1 GHz narrow band frequency range for S₁₁ and electric impedance respectively.

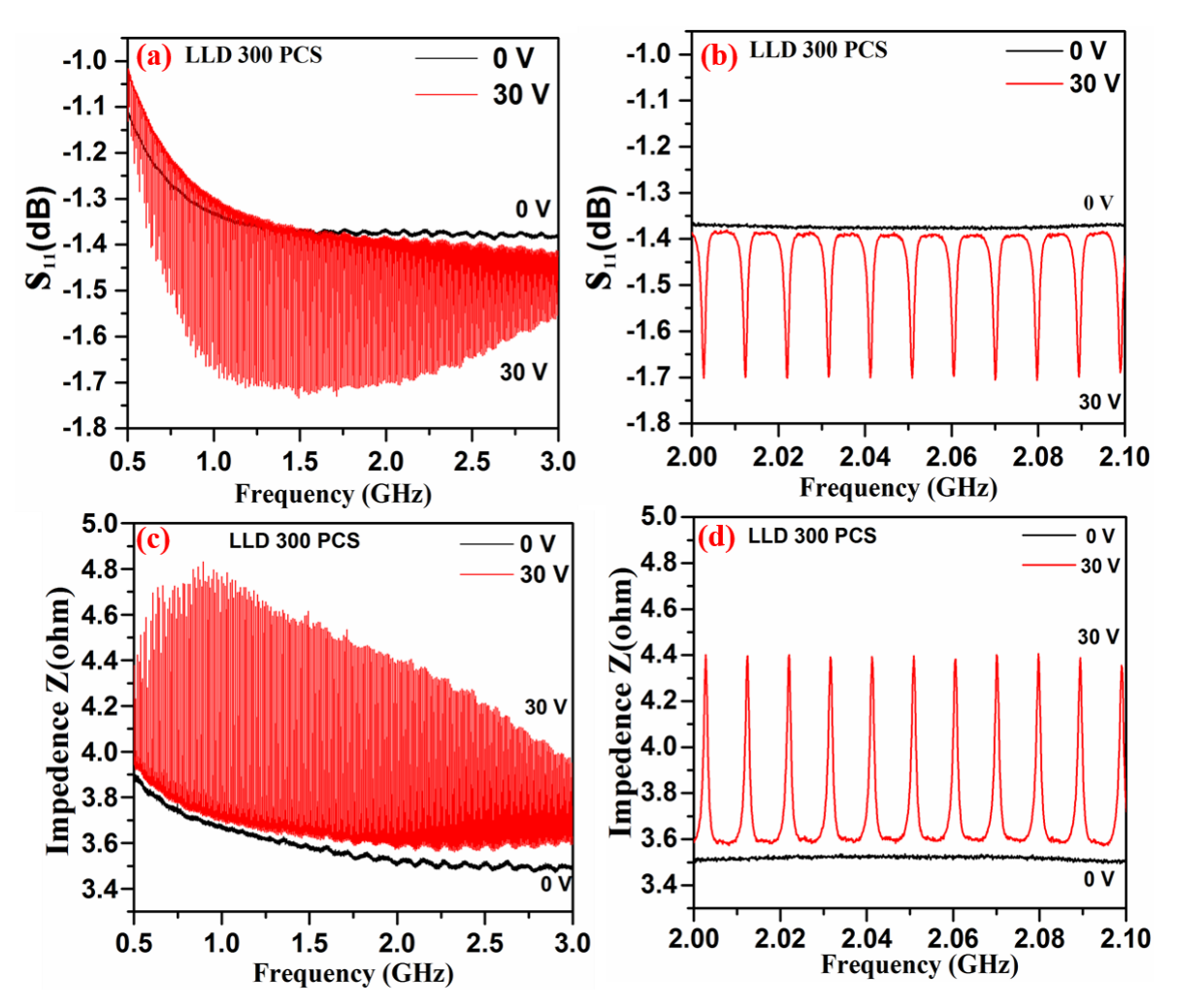


Fig.6.17 (a), (c) Measured frequency spectrum of HBAR of LLD 300 PCS with and without dc biasing, S₁₁ and calculated electric impedance in broad band range of 500 MHz–3 GHz respectively. Fig. (b), (d) HBAR response in S₁₁ and electric impedance with and without dc bias in narrow frequency range of 2–2.1 GHz.

6.10 Conclusions

Laser annealing of BST5 thin films are carried out for PLD deposited thin films at 300°C temperature. It is observed that the films are amorphous at 300°C and films deposited at 700°C are crystalline. The 300°C deposited amorphous films showed crystalline phase formation after laser irradiation with KrF excimer laser of 248 nm at 300°C. The layer-by-layer deposition at 300°C with subsequent laser annealing with an expanded beam of laser after each deposition showed vertical crystallization of about 600

nm thick films as confirmed by XRD, Raman and UV-Vis-NIR studies. The systematic decrease in the bandgap value after each layer of the laser annealing process shows the continuity of the process. These layered films showed HBAR response and microwave tunability of 34% at 1GHz, which is approaching the value given by conventionally deposited films. Thus, the layer-by-layer deposition and subsequent laser annealing method is found to be practical to yield tunability with a film processed at 300°C. Therefore, this process is compatible to develop various microwave devices like varactors, tunable filters and phase shifters and resonators on polymer substrates that can pave the way to active polymer microwave electronics.

References

- [1] M.G. Kang, K. H. Cho, S. M. Oh, Y.H. Do, C.Y. Kang, S. Kim, S.J. Yoon, Current Applied Physics, 11, S66-S69 (2011).
- [2] M.G. Kang, K.H. Cho, Y.H. Do, Y.J. Lee, S. Nahm, S.J. Yoon and C.Y.Kang, Appl. Phys. Lett., 101, 242910 (2012).
- [3] A. Queraltóa, A. P. del Pino, M. de la Mata, M. Tristany, X. Obradors, T. Puig, S.T. McKinstry, Ceramics International, 42, 4039–4047 (2016).
- [4] X.M. Lu, J.S. Zhu, W.S. Hu, Z.G. Liu and Y.N. Wang, Appl. Phys. Lett., 66, 2481-2483 (1995).
- [5] S. Halder, U. Boettger, T. Schneller, R. Waser, O. Baldus, P. Jacobs, M. Wehner, Mater. Sci. Eng. B, 133, 235–240 (2006).
- [6] S. C. Lai, Hang-Ting Lue, K. Y. Hsieh, S. L. Lung, Rich Liu, T. B. Wu, P. P. Donohue, and P. Rumsby, J. Appl. Phys., 96, 2779-2784 (2004).
- [7] Adarsh Rajashekhar, Austin Fox, S. S. N. Bharadwaja, and S. T. McKinstry, Applied Physics Letters 103, 032908 (2013).
- [8] J. H. Chen, C. L. Lia, K. Urban, & C. L. Chen, *Applied physics letters*, 81(7) 1291-1293 (2002).
- [9] H. J. Gao, C. L. Chen, B. Rafferty, S. J. Pennycook, G. P. Luo, and C. W. Chu, Appl. Phys. Lett. 75, 2542 (1999).
- [10] Z. Huang, Q. Zhang, and R. W. Whatmore, Journal of Applied Physics 85, 7355 (1999).
- [11] Jyh-Liang Wang, Yi-Sheng Lai, Sz-Chian Liou, Bi-Shiou Chiou, Chueh-Kuei Jan, and Huang-Chung Cheng, Journal of Vacuum Science & Technology B 26, 41 (2008).
- [12] O. Baldus and R. Waser, J. Eur. Ceram. Soc., 24,3013-3020 (2004).
- [13] Won-Jae Lee, Ho-Gi Kim, and Soon-Gil Yoon, Journal of Applied Physics, 80, 5891 (1996).
- [14] Z. Saroukhani, N. Tahmasebi, S. M. Mahdavi and Ali Nemati, Bull. Mater. Sci., Vol. 38, No. 6, pp. 1645–1650 (2015).
- [15] Y.H. Cheng, X.L. Qiao, J.G. Chen, Y.P. Wu, C.S. Xie, Y.Q. Wang, D.S. Xu, S.B. Mo, Y.B. Sund, Surface and Coatings Technology 160,269–276 (2002).
- [16] J. P. Zhao, Z. Y. Chen, T. Yano, T. Ooie, M. Yoneda, and J. Sakakibara, Journal of Applied Physics 89, 1634 (2001).

- [17] Yu. I. Yuzyuk, Phys. Solid Stat. 54, 1026 (2012).
- [18] R. Naik et.al, Phys. Rev. B, 61, 11367 (2000).
- [19] Q. Zhang, J. Zhai, L. Kong, X. Yao, J. Appl. Phys. 112, 124112 (2012).
- [20] L.Z. Cao, B.L. Cheng, S.Y. Wang, W.Y. Fu, S. Ding, Z.H. Sun, H.T. Yuan, Y.L. Zhou, Z.H. Chen, G.Z. Yang, J. Phys. Appl. Phys. 39, 2819 (2006).
- [21] S.Y. Wang, B.L. Cheng, C. Wang, S.Y. Dai, K.J. Jin, Y.L. Zhou, H.B. Lu, Z.H. Chen,G.Z. Yang, J. Appl. Phys. 99, 013504 (2006).
- [22] J. D. Freire and R. S. Katiyar, Phys. Rev. B 37, 2074 (1988).
- [23] V Pal, O P Thakur and R K Dwivedi, J. Phys. D: Appl. Phys. 48, 055301(2015).
- [24] R. Swanepoel, J. Phys. [E]. 16, 1214 (1983).
- [25] J.C. Tauc, F. Abeles., Optical properties of solids, North-Holland, Amsterdam, 1972.
- [26] H.Y. Tian, W.G. Luo, A.L. Ding, J. Choi, C. Lee, K. No, Thin Solid Films. 408, 200–205 (2002).
- [27] K. Sandeep, J.P. Goud, K.C.J. Raju, IEEE. (2016). https://doi.org/10.1109/ISAF.2016.7578099
- [28] S. Tappe, U. Böttger, R. Waser, Appl. Phys. Lett. 85, 624–626 (2004)
- [29] S. Sandeep, J.P. Goud, K.C. James Raju, Appl. Phys. Lett. 111, 012901 (2017).
- [30] J. Pundareekam Goud, Mahmoud S. Alkathy, K. Sandeep, S. Ramakanth and K. C. James Raju, Journal of Materials Science: Materials in Electronics 29, 15973–15982 (2018).
- [31] L.Zhang, Y. Pu, M Chen, T. Wei, W. Keipper, R. Shi, X. Guo, R. Li, and Peng, *J. Eur. Ceram. Soc.*, 40, 71-77 (2020).
- [32] A. R. Jayakrishnan, Kevin V. Alex, K. Kamakshi, J. P. B. Silva, K. C. Sekhar,
 M. J. M. Gomes, J. Mater. Sci. Mater. Electron. 30, 19374–19382 (2019).
- [33] Hao Zhang, Wei Pang, Hongyu Yu, and Eun Sok Kim, Journal of Applied Physics 99, 124911 (2006).
- [34] J.P.B. Silva, A. Khodorov, A. Almeida, Appl. Phys. A 116, 1271-1280 (2014).

Chapter-7

Conclusions and scope of future work

7.1 Conclusions

In this chapter, a summary of the outcome of work done for this thesis is presented. It includes the results obtained through phase analysis, structural and microstructural studies, optical, electrical, and microwave dielectric characterizations of BST thin films. The work's main objectives are 1) Reducing the crystallization temperature of BST thin film and achieving a film with as high a tunability as possible using a laser annealing technique. 2) To achieve the BST thin films' full vertical crystallization using layer-by-layer deposition and laser annealing at 300°C. High quality thin films with high tunability at microwave frequencies are required in tunable microwave devices such as tunable filters, phase shifters and resonators.

Chapter-2 describes the experimental techniques that are used as part of implementing the work of this thesis. It includes preparation techniques used for the Barium Strontium Titanate (BST) ceramic target which is to be used for thin film deposition. This chapter also describe the working principle and procedure of structural characterization techniques used like XRD, Raman, and TEM as well as microstructural studies from FESEM and TEM. It also describes other important techniques such as optical bandgap studies by using UV/VIS/NIR spectrometer, and microwave dielectric property studies using Vector Network Analyzer (VNA). The measurement procedures for electrical and microwave dielectric properties are explained.

Thin films of Barium Strontium Titanate (Ba_{0.5}Sr_{0.5}TiO₃) were deposited using the Pulsed Laser Deposition (PLD) technique on MgO (100) substrate at different working pressures (Chapter-3). The deposition temperature of 750°C is kept constant and the oxygen working pressure is varied from 1×10^{-1} to 1×10^{-4} mbar. The X-ray diffraction pattern indicates that films deposited with higher oxygen working pressure are partially

crystalline. Improved crystallinity is seen in the films that are deposited at lower oxygen working pressure of 1×10^{-4} mbar. As the oxygen working pressure increases, the lattice parameter and the unit cell volume of all films decreases. The crystallinity can be further increased with a specific orientation by increasing the laser fluence from 1.4 J/cm² to 2 J/cm². The above films' tunability are investigated using IDC test structures at the microwave frequency by applying dc bias voltage (0-75 V). The maximum tunability at 1 GHz observed for the (111) film is 16.5%, whereas the remaining films exhibited low tunability. The films showed a (111) orientation dominated growth for films deposited at a lower working pressure of oxygen and a higher laser fluence. For these films, the orientation factor is determined, and it is observed that higher film orientation factor show greater tunability. These studies also allowed us to investigate the relation between structure and microwave dielectric properties.

Chapter-4 discusses a systematic study of the effect of deposition laser energy density (or) laser fluence on the structural, the microstructural and the optical properties of polycrystalline $Ba_{0.6}Sr_{0.4}TiO_3$ (BST6) ferroelectric thin films deposited using PLD on fused silica substrates. The Barium Strontium Titanate $Ba_{0.6}Sr_{0.4}TiO_3$ (BST6) thin films are deposited by the PLD process at different laser fluences, maintaining a constant oxygen pressure. X-ray diffraction analysis confirms the formation of single-phase cubic films and the crystallite size calculated by using the Williamson-Hall method. The results show that the crystallite size increases with increasing laser fluences. The thin-film microstructures have been studied using HRTEM, and the results show the presence of (110) faceted planes of BST6 with d spacing $\sim 2.72-2.79$ Å. The BST6 thin films' optical bandgap is calculated by applying the Tauc relation-from the transmission spectra in the 190-2500 nm range. Optical parameters such as bandgap are calculated from recorded optical transmission spectra and correlated with structural and microstructural properties of $Ba_{0.6}Sr_{0.4}TiO_3$

(BST6) thin films. The BST6 thin films grown at $2J/cm^2$ showing the best microstructural and optical properties were selected for the microwave dielectric measurements by depositing a test circular patch capacitor on the film. It can be inferred that the laser fluence is an essential parameter in tuning the dielectric/ferroelectric properties of the films under optimized conditions. The microwave tunability and dielectric constant (ϵ_r) of a well crystallized BST6 thin film were found to be ~56% and ~284, respectively at 1GHz making it suitable for applications in tunable microwave devices.

Chapter-5 discusses the optimization processes to obtain low-temperature crystallization of amorphous thin-film of Ba_{0.5}Sr_{0.5}TiO₃ (BST5) using a KrF excimer laser of 248 nm. The ceramic target of BST5 is used for the deposition of BST5 thin films by using a pulsed laser deposition technique on fused silica (FS) substrates and is found to be amorphous when the deposition temperature is 300°C. The laser annealing processes are conducted at 300°C temperature with different optimizing parameters like the number of laser pulses, the energy density, and the pulse repetition rate on the samples deposited at 300°C. After applying laser pulses, the phase confirmation, microstructural, vibrational, and optical responses are acquired and analyzed. The XRD confirms these films' crystallization, with optimized laser annealing parameters like 10Hz repetition rate, 2000 pulses and laser energy density of 66 mJ/cm². The crystallite size increases with the increase in the number of pulses (i.e. from 250 to 2000) and is adjudged to be coalescence of nano crystallites. FESEM observations support the nano crystallites coalescence, leading to larger granular grains evolution.

A significant bandgap narrowing with crystallization is another supporting affirmation. Cross-sectional TEM investigations are carried out for optimized BST5 films. The microstructural detailing suggests that up to a thickness of about 120 nm, the film is crystallized with the use of optimized laser annealing parameters in this study. As

presented in Chapter-6, a layer-by-layer deposition and subsequent annealing after each deposition is done to obtain the microwave device quality films optimized for 600 nm thick BST5. These layer by layer deposited and laser crystallized films at 300°C will be of extensive use extending from polymer to ceramic substrates, when compared to its conventionally prepared counterparts that are deposited at 700°C.

Chapter-6 discusses the crystallization of BST5 thin films at lower temperatures. BST5 thin films are crystallized layer-by-layer after deposition and subsequent laser annealing at 300°C using excimer laser of KrF-248 nm as the source for both deposition and annealing. In this process, BST5 film of up to 600 nm thickness is crystallized in which each individual cycle of deposition and annealing is with a layer of 120 nm thickness and the laser annealing is done with 66 mJ/cm² of optimized laser fluence. The temperature of 300°C is kept constant for both the deposition and the annealing processes. The phase formation and full vertical crystallization of BST5 thin films are confirmed by XRD patterns, Raman spectroscopy, UV-Vis-NIR spectroscopy and cross-sectional TEM.

It is observed that the as deposited films deposited at 300°C are amorphous, and films deposited at 700°C are crystalline. The 300°C deposited amorphous films showed crystalline phase formation after laser irradiation with KrF excimer laser of 248 nm at 300°C. The layer-by-layer deposition at 300°C with subsequent laser annealing with an expanded beam of the laser after each deposition showed vertical crystallization of about 600nm thick films. The systematic decrease in the bandgap value after each layer of the laser annealing process shows the process's continuity. These layer-by-layer processed films showed HBAR response and microwave tunability of 34% at 1GHz, which is approaching the value given by conventionally processed films at 700°C. Thus, the layer-by-layer deposition and subsequent laser annealing method is found to be practical to yield tunability with a film processed at 300°C. From the leakage current measurements, it is

clear that LA films have a lower leakage current when compared to conventional processed films. It is a crucial achievement as lower leakage current is an essential figure of merit for tunable microwave devices and for such films used in nanoelectronic CMOS circuit fabrication. Therefore, this process is compatible with developing various microwave devices like varactors, tunable filters, phase shifters and resonators on polymer substrates that can pave the way to an active polymer microwave electronics.

7.2 Scope of future work

The work carried out in the present thesis has created more interest in carrying out further research in related fields like ferroelectric, laser-matter interaction, and flexible electronics.

- 1. Fabrication of device quality epitaxial Barium Strontium Titanate thin films for better response and to use in tunable microwave devices at lower temperatures.
- Use of laser annealing process to further reduce the substrate temperature from 300°C to room temperature for further opening up the scope of flexible and wearable microwave electronics.

The field of laser annealing is still open since numbers of variables are too high such as use of different lasers (Excimer & Nd-YAG) with different wavelengths (248 nm, 264 nm, 356 nm, 532 nm and 1064 nm) and having different laser related parameters (pulse width, rep. rate, and laser energy density), substrate related parameters, etc. Therefore, this study is only a beginning as all these factors needs to be considered before a best and efficient process can be standardized for industry.

List of Publications:

List of Patents

1. J. Pundareekam Goud, S Ramakanth, Kongbrailatpam Sandeep, Ajeet Kumar and K.C. James Raju "Laser based method to crystallize ferroelectric thin film at 300°C temperatures for tunable microwave devices", Filed for an Indian patent. Application no. 201941007633 dated February 27, 2020.

List of Publications in part of Thesis

- 1. **J. Pundareekam Goud,** S Ramakanth, Andrews Joseph, Kongbrailatpam Sandeep, G L N Rao, and K C James Raju, "Effect of crystallinity on microwave tunability of Pulsed laser deposited Ba_{0.5}Sr_{0.5}TiO₃ Thin Films" **Thin Solid Films 626 126–130 (2017).**
- 2. **J. Pundareekam Goud**, Kongbrailatpam Sandeep, Sivanagi Reddy Emani, Mahmoud. S. Alkathy, Kuna Lakshun Naidu and K C James Raju "Zr-substituted Ba_{0.6}Sr_{0.4}TiO₃ ferroelectric thin films grown by pulsed laser deposition (PLD) at different laser fluence". **Ferroelectrics, VOL. 516, 28–35, (2017).**
- 3. **J. Pundareekam Goud**, Mahamoud S. Alkathy, K.C. James Raju, "Structural, dielectric and impedance study of Bi and Li co-substituted Ba_{0.5}Sr_{0.5}TiO₃ ceramics for tunable microwave devices applications", **Journal of Materials Science: Materials in Electronics**, **29**, **3611–3620** (**2018**).
- 4. **J. Pundareekam Goud**, Mahmoud S. Alkathy, Kongbrailatpam Sandeep, S Ramakanth and K. C. James Raju "Influence of laser fluence on structural, optical and microwave dielectric properties of pulsed laser deposited Ba_{0.6}Sr_{0.4}TiO₃ thin films". **Journal of Materials Science: Materials in Electronics, 29, 15973–15982 (2018).**
- 5. **J. Pundareekam Goud**, Ajeet Kumar, S Ramakanth, Kongbrailatpam Sandeep, and K.C. James Raju, "Tunable microwave device fabrication on low-temperature crystallized Ba_{0.5}Sr_{0.5}TiO₃ thin films by an alternating deposition and laser annealing process", **Manuscript being reviewed and Revised**. (**Advanced Electronic materials**).
- 6. **J. Pundareekam Goud**, Ajeet Kumar, Kongbrailatpam Sandeep, Deepak kumar, S. Ramakanth, K. C. James Raju, A.R. James, Partha Ghoshal, "Reducing the leakage current in BST by a low temperature crystallization process", **Manuscript under preparation**.

List of other Publications:

- 7. Andrews Joseph, **J. Pundareekam Goud**, Sivanagi Reddy Emani, K. C. James Raju "Study of amorphous and crystalline phases of sodium bismuth titanate thin films by optical and Raman spectroscopy", **J Mater Sci: Mater Electron 28:4362–4370 (2017).**
- 8. Kongbrailatpam Sandeep, **J. Pundareekam Goud**, and K. C. James Raju, Resonant spectrum method for characterizing Ba_{0.5}Sr_{0.5}TiO₃ based high overtone bulk acoustic wave resonators, **Applied Physics Letters 111, 012901 (2017).**
- 9. S Pattipaka, **J. Pundareekam Goud**, GP Bharti, KCJ Raju, A Khare, D Pamu, "Effect of oxygen partial pressure on nonlinear optical and electrical properties of BNT–KNNG composite thin films", **Journal of Materials Science: Materials in Electronics 31 (4), 2986-2996 (2020).**
- 10. Kongbrailatpam Sandeep, J. Pundareekam Goud, and K. C. James Raju, "Effects of a Coated Material Layer on High Overtone Bulk Acoustic Resonator and its Possible Applications", IEEE Transactions on Ultrasonics, Ferroelectrics, and Frequency Control, Sept-21, (2020). DOI: 10.1109/TUFFC.2020.3025618.

List of Conference Proceedings:

- 11. **J. Pundareekam Goud,** Bashaiah Sindam, Anil Tumuluri, and K.C. James Raju, "Microwave absorption properties of LiNb₃O₈ in X-band prepared by combustion synthesis". **AIP Conference Proceedings 1675, 020024 (2015).**
- 12. **J. Pundareekam Goud,** Andrews Joseph, S. Ramakanth, Kuna Lakshun Naidu, and K. C. James Raju "Microwave dielectric and optical properties of amorphous and crystalline Ba_{0.5}Sr_{0.5}TiO₃ thin films" **AIP Conference Proceedings 1728, 020293,(2016).**
- 13. K. Sandeep, J. Pundareekam Goud, K.C. James Raju, "Switchable High Overtone Resonance in BST film with MIM structure on Sapphire Substrate", 978-1-5090-1871-0/16/\$31.00 ©2016 IEEE Workshop (ISAF/ECAPD/PFM IEEE International Symposium) (2016).
- 14. Mahmoud S. Alkathy, **J. Pundareekam Goud**, and K. C. James Raju "Effect of sintering temperature on structural and dielectric properties of Bi and Li cosubstituted SrTiO₃" **AIP Conference Proceedings 1728, 020355 (2016).**
- 15. Andrews Joseph, **J. Pundareekam Goud**, Sivanagi Reddy Emani, and K.C. James Raju "Microwave Dielectric and Optical Properties of Pulsed Laser Deposited N_{a0.5}B_{i0.5}Ti_{O3} Thin Film" **AIP Conference Proceedings 1731, 080039 (2016).**
- 16. Bashaiah Sindam, **J. Pundareekam Goud**, and K.C. James Raju "Microwave assisted synthesis of Ba (Zn_{1/3}Ta_{2/3})O₃ nanoparticles" **Materials Today: Proceedings 3, 2101–2106 (2016).**

Conferences/Symposium/ Workshops attended

- 1. **J. Pundareekam Goud,** Bashaiah Sindam, Anil Tumuluri and K. C. James Raju "Microwave Absorption Properties of LiNb₃O₈ in X-band prepared by combustion synthesis" ORAL presentations (AMRP-2015).
- 2. **J. Pundareekam Goud**, Sivanagi reddy emani, Mahmoud. S. Alkathy, Kuna Lakshun Naidu and K. C. James Raju, "Zr-substituted Ba_{0.6}Sr_{0.4}TiO₃ ferroelectric thin films grown by pulsed laser deposition (PLD) at different laser fluence", POSTER presentation, AMF-2017.
- 3. **J. Pundareekam Goud**, K C James Raju, "Ba_{0.6}Sr_{0.4}TiO₃ fferroelectric thin films grown at different laser fluence", POSTER presentation, FIP-2016.
- 4. **J. Pundareekam Goud,** Andrews Joseph, S. Ramakanth, Kuna Lakshun Naidu, and K. C. James Raju "Microwave dielectric and optical properties of amorphous and crystalline Ba_{0.5}Sr_{0.5}TiO₃ thin films", ICC-2015, POSTER presentation.
- J. Pundareekam Goud, S Ramakanth, Ajeet Kumar, and K. C. James Raju,
 "Laser induced crystallization of tunable BST thin films suitable for RF and high frequency Devices", ISIF-2017, ORAL presentations.
- 6. **J. Pundareekam Goud**, Processing and Characterization of Thin Films, work shop, UGC-NRC, School of Physics, University of Hyderabad, 2018.
- 7. **J. Pundareekam Goud**, Kongbrailatpam Sandeep, Ajeet Kumar, Bibhudatta Sahoo, S. Ramakanth, A.R. James, and K.C. James Raju, "Thickness dependent microwave tunability of pulsed laser ablated Ba_{0.5}Sr_{0.5}TiO₃ thin films", ICONN-19, POSTER presentation.

Laser-induced Crystallization of Barium Strontium Titanate Thin Films for Microwave Device Applications

by J Pundareekam Goud

Submission date: 21-Dec-2020 11:43AM (UTC+0530)

Submission ID: 1479965491

File name: PhD-Thesis13PHPH07-J_P_GOUD.pdf (9.05M)

Word count: 28086

Character count: 144728

Laser-induced Crystallization of Barium Strontium Titanate Thin Films for Microwave Device Applications

ORIGINALITY REPORT

15%

SIMILARITY INDEX

INTERNET SOURCES

PUBLICATIONS

STUDENT PAPERS

PRIMARY SOURCES

J. Pundareekam Goud, Mahmoud S. Alkathy, Kongbrailatpam Sandeep, S. Ramakanth, K. C. James Raju. "Influence of laser fluence on structural, optical and microwave dielectric properties of pulsed laser deposited Ba0.6Sr0.4TiO3 thin films", Journal of Materials Professor

Science: Materials in Electronics, 2018 Publication

School of Physics University of Hyderahad Hyderabad-500 046, INDIA

J. Pundareekam Goud, S. Ramakanth, Andrews Joseph, Kongbrailatpam Sandeep, G. Lakshminarayana Rao, K.C. James Raju. "Effect of crystallinity on microwave tunability of pulsed laser deposited Ba0.5Sr0.5TiO3 thin Professor films", Thin Solid Films, 2017

Publication

School of Physics University of Hyderahad Hyderabad-500 046. INDIA

J. Pundareekam Goud, Kongbrailatpam Sandeep, Sivanagi Reddy Emani, Mahmoud. S. Alkathy, Kuna Lakshun Naidu, K. C. James Raju. " Zr-substituted Ba Sr TiO ferroelectric thin films grown by pulsed laser deposition (PLD) at K.C. James Raju

Professor School of Physics University of Hyderabad Hyderabad-500 046. INDIA

different laser fluence ", Ferroelectrics, 2017

Publication

4	"Physics of Semiconductor Devices", Springer Science and Business Media LLC, 2014 Publication	<1%
5	baadalsg.inflibnet.ac.in Internet Source	<1%
6	worldwidescience.org Internet Source	<1%
7	S. S. N. Bharadwaja. "Excimer Laser Crystallized (Pb,La)(Zr,Ti)O ₃ Thin Films", Journal of the American Ceramic Society, 2/25/2008	<1%
8	aip.scitation.org Internet Source	<1%
9	www.springerprofessional.de Internet Source	<1%
10	Kong, L.B "Electrically tunable dielectric materials and strategies to improve their performances", Progress in Materials Science, 201011 Publication	<1%
11	Sivanagi Reddy Emani, K. C. James Raju. "Effect of substrate temperature on the optical	<1%

69	gateway.webofknowledge.com Internet Source	<1%
70	Dmitri A. Tenne. "Raman Spectroscopy of Ferroelectric Thin Films and Superlattices", Journal of the American Ceramic Society, 4/4/2008 Publication	<1%
71	McCarter, W.J "Gel formation during early hydration", Cement and Concrete Research, 198701 Publication	<1%
72	studentsrepo.um.edu.my Internet Source	<1%
73	Yong Zeng, Yan Zhao, Yijian Jiang. "Effect of KrF excimer laser irradiation on the surface changes and photoelectric properties of ZnO single crystal", Journal of Alloys and Compounds, 2016 Publication	<1%
74	impj.ir Internet Source	<1%

Exclude quotes

On

Exclude matches

< 14 words

Exclude bibliography

On



UNIVERSITY OF HYDERABAD CENTRE FOR ADVANCED STUDIES IN ELECTRONICS SCIENCE & TECH. (CASEST) SCHOOL OF PHYSICS HYDERABAD 500 046, INDIA

Dr.K.C.James Raju Professor

21.12.2020

TO WHOM IT MAY CONCERN

This is to certify that the thesis titled "Laser-induced Crystallization of Barium Strontium Titanate Thin Films for Microwave Device Applications" submitted by Mr. J. Pundareekam Goud (Reg.No:13PHPH07), has been screened by the Turnitin software at Indira Gandhi memorial library (IGML), University of Hyderabad. This software shows 16% similarity index out of which 8% came from the candidates own publications (where he is the first author) directly related to this thesis.

From the detailed similarity index report, it is obvious that the remaining 8% of the similarity index, is due to the resemblance caused by the frequent use of the well-known standard terms such as ferroelectric, Barium Strontium Titanate, microwave dielectric properties, dielectric constant, dielectric loss, Tunability, Tunable microwave devices, Varactor, High overtone bulk acoustic resonator (HBAR), Pulsed Laser Deposition, KrF Excimer laser, Wavelength, Repetition rate, Laser fluence, Laser annealing, BST, PZT, Thin film, X-ray diffraction pattern (XRD), Crystallite size, Field Emission Scanning Electron Microscopy (FESEM), Grain size, Transmission Electron Microscope (TEM), Optical properties, Raman effect, Bandgap, Electrical properties and Leakage current. The use of such terms is rampant in the literature, and hence it is not surprising that the similarity index is artificially inflated. It should be noted that the use of such standard terms cannot be avoided.

Prof. K. C. James Raju (Supervisofssor School of Physics School of Physics

School of Physics University of Hyderabad Hyderabad-500 046. INDIA